Project No. 12-3318

Advanced Supercritical Carbon Dioxide Brayton Cycle Development

Reactor Concepts

Mark Anderson
University of Wisconsin, Madison

In collaboration with:
Argonne National Laboratory

Steven Reeves, Federal POC
Jim Sienicki, Technical POC

NEUP Nuclear Energy University Programs
U.S. Department of Energy

FINAL REPORT
Advanced Supercritical Carbon Dioxide Brayton Cycle Development (NEUP project 12-3318)

Project Number: NU-12-WI-UWM_-3030-02 (Project 12-3318)
Project Title: Advanced Supercritical Carbon Dioxide Brayton Cycle Development

Submitted by:
Mark Anderson, PhD
Univesity of Wisconsin - Madison
Director, Thermal Hydraulics Laboratory
Dept. Engineering Physics
1500 Engineering Dr.
Madison WI 53706
608-263-2802
manderson@engr.wisc.edu

Prepared by: Haomin Yuan

Abstract

Fluids operating in the supercritical state have promising characteristics for future high efficiency power cycles. In order to develop power cycles using supercritical fluids, it is necessary to understand the flow characteristics of fluids under both supercritical and two-phase conditions. In this study, a Computational Fluid Dynamic (CFD) methodology was developed for supercritical fluids flowing through complex geometries. A real fluid property module was implemented to provide properties for different supercritical fluids. However, in each simulation case, there is only one species of fluid. As a result, the fluid property module provides properties for either supercritical CO_2 (S-CO_2) or supercritical water (SCW). The Homogeneous Equilibrium Model (HEM) was employed to model the two-phase flow. HEM assumes two phases have same velocity, pressure, and temperature, making it only applicable for the dilute dispersed two-phase flow situation. Three example geometries, including orifices, labyrinth seals, and valves, were used to validate this methodology with experimental data.

For the first geometry, S-CO_2 and SCW flowing through orifices were simulated and compared with experimental data. The maximum difference between the mass flow rate predictions and experimental measurements is less than 5%. This is a significant improvement as previous works can only guarantee 10% error. In this research, several efforts were made to help this improvement. First, an accurate real fluid module was used to provide properties. Second, the upstream condition was determined by pressure and density, which determines supercritical states more precise than using pressure and temperature.

For the second geometry, the flow through labyrinth seals was studied. After a successful validation, parametric studies were performed to study geometric effects on the leakage rate. Based on these parametric studies, an optimum design strategy for the see-through labyrinth seals was proposed. A stepped labyrinth seal, which mimics the behavior of the labyrinth seal used in the Sandia National Laboratory (SNL) S-CO_2 Brayton cycle, was also tested in the experiment along with simulations performed.

The rest of this study demonstrates the difference of valves' behavior under supercritical fluid and normal fluid conditions. A small-scale valve was tested in the experiment facility using S-CO_2. Different percentages of opening valves were tested, and the measured mass flow rate agreed with simulation predictions. Two transients from a real S-CO_2 Brayton cycle design provided the data for valve selection. The selected valve was studied using numerical simulation, as experimental data is not available.

Contents

Figures

Tables

1. Introduction

This research aims at developing a CFD methodology for fluid flow through complex geometries under both supercritical and two-phase conditions. This chapter is divided into four sections; the first section introduces the research goals, the second section discusses the choice of tools, the third section presents the research flow chart, with the final section discussing the organization of the remaining chapters.

1.1 Research goals

Based on the increasing interest in the application of supercritical fluids, an understanding of supercritical fluid flow is in great demand. In this research, a CFD methodology was developed to simulate supercritical fluid flow with a two-phase modeling capability. Three example geometries were tested to provide an insight of the flow and demonstrate the developed methodology's validity. In summary, this research has achieved the following goals:

- Developing a CFD methodology to simulate supercritical and two-phase flow simultaneously. CO_2 and water were used as examples. However, other fluids could be implemented using the same method.
- Simulating the flow through orifices to examine the supercritical fluid choked flow problem. The Homogenous Equilibrium Model (HEM) was tested to determine its applicability.
- Using the proposed methodology to develop an optimization method for labyrinth seals under S-CO_2 conditions. Parametric studies were performed to investigate the geometric effects.
- Using the proposed methodology to evaluate valves under S-CO_2 conditions. This goal encompasses simulating the valve geometry to predict its mass flow rate and possible issues with regard to cavitation and Mach number.

1.2 Choice of tools

In order to study supercritical fluid flow, a proper tool is needed. There are two common ways to approach this problem: experimental and model based. Regarding modeling, specialized models exist, but they are usually limited to specific geometries. CFD simulation can be performed without geometric limitations. There are many CFD codes on the market, both commercial and open source. Due to the proprietary nature of commercial codes, users cannot access their source codes. This lack of access is problematic, as they cannot simulate supercritical and two-phase flow simultaneously without code modification. For example, for the commercial CFD code ANSYS-FLUENT, users can only use real fluid property in the supercritical or single-phase regions, but not in the two-phase region [1]. Therefore, the open source CFD code, OpenFOAM, was used due to its easy access to source code. It could use real fluid property in the two-phase region without deciding the state is in the two-phase region or not. OpenFOAM was chosen also based on the author's prior experience with C++ and its widespread use in academia and industry. However, if real fluid property could be used in the two-phase region in commercial codes, like ANSYS-FLUENT, they could also be used for this research. Figure 1 presents the logics associated with the choice of tools in this research. In addition to the CFD code, simulating the supercritical fluid flow requires a database for real fluid properties. Initially, REFPROP [2] was used to provide real fluid properties, but it slows down simulations. Therefore, the property code FIT [3] was instead employed with a much better computational efficiency. Chapter 3 covers more detail about the implementation of the property module.

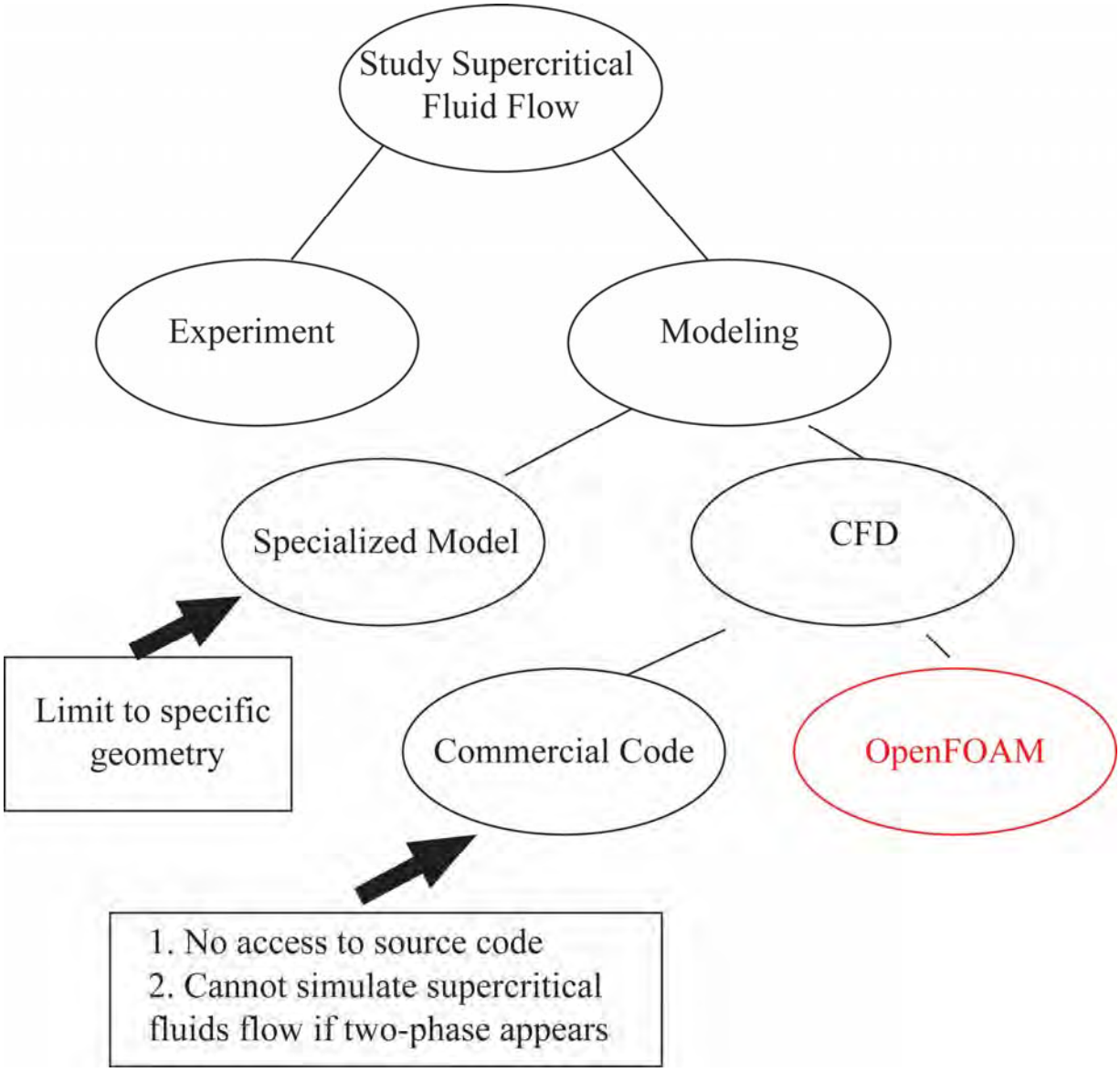

Figure 1 Choice of tools

1.3 Research flow chart

Figure 2 describes the flow chart of this research. This research is divided into three major steps in order to accomplish the goals presented in Section 1.1. The first step was to study OpenFOAM and the real fluid module. This step was regarded as the foundation for all subsequent efforts. The second step was to develop the simulation methodology based on OpenFOAM. In the third step, three example geometries were chosen to validate the proposed numerical methodology with experimental data. The first geometry was orifices, including circular and annular orifices, as it is typically used to study the choked flow problem, which may be encountered in a pipe break scenario. Subsequently, the geometry of labyrinth seals was used as another demonstration. As a labyrinth seal was used in the SNL S-CO_2 Brayton cycle experiment loop, the study of a labyrinth seal is needed to benefit their experiment. Finally, the valve was used as another example. The developed methodology could be used to evaluate and design components in real supercritical fluid cycles in the future.

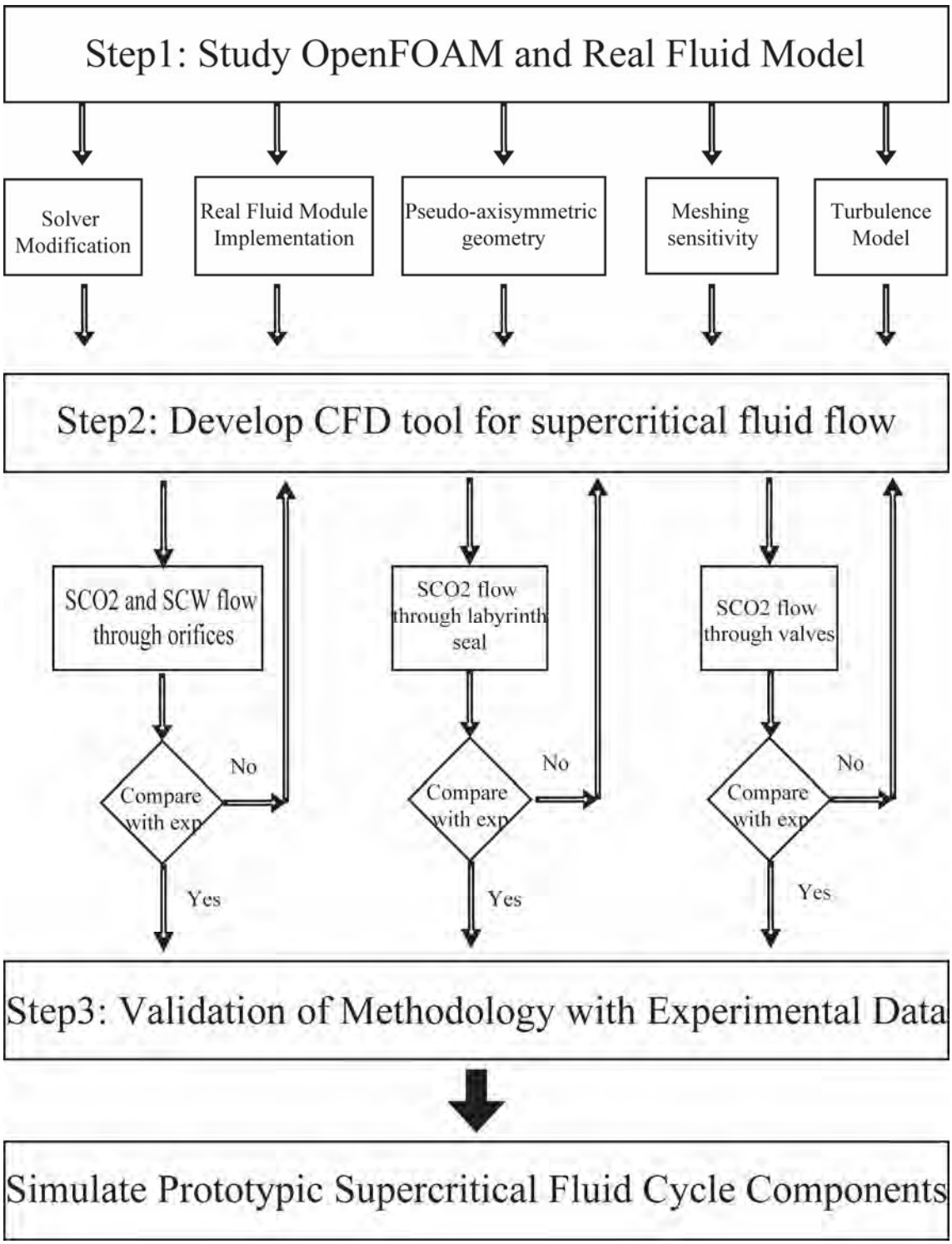

Figure 2 Research flow chart

1.4 Organization

The following chapters delve into the details of this research. Chapter 2 discusses the previous works in this area and lays the foundation with regard to the importance of this work. Chapter 3 describes the methodology set forth to develop the OpenFOAM computational tool for the evaluation of supercritical fluid flow. Chapter 4 introduces the experiment facility, which provides validation data for this research. Chapter 5 presents the validation of the proposed numerical methodology by comparisons with experimental data for three example geometries. Chapter 5 also discusses the details and nuances associated with implementing the simulations to different geometries. Finally, Chapter 6 concludes this research with a complete summary.

2. Background and literature review

This chapter presents the background and literature review with six sections included. The first section explains supercritical fluids and their applications to power cycles. The S-CO_2 Brayton cycle is presented as an example to demonstrate the benefits of using supercritical fluids for power generation. The second section discusses the previous works and challenges associated with conducting CFD simulations of supercritical fluid flow. After that, three consecutive sections review the works conducted for three example geometries of interest. The final section presents a brief summary.

2.1 Supercritical fluid and supercritical fluid power cycles

A supercritical fluid is defined as a fluid in a state where pressure and temperature are above its critical point [4]. As shown in Figure 3, for CO_2, its critical point is 7.38 MPa at 31.1 ^{o}C [5]. When a fluid is supercritical, it does not exhibit a saturation point where two phases can be distinguished. However, supercritical fluids exhibit a pseudo-critical point, around which fluid properties (e.g., density and specific heat as shown in Figure 4) dramatically change.

Scientists and engineers have considered using supercritical water (SCW) for high efficiency power cycles for many years [6]–[11]. SCW has already been used in fossil power plants to increase power cycle efficiency [12]. However, safety issues like high pressure, high temperature, and intensive corrosion prevent its application to nuclear power generation. More recently, other fluids like CO_2 and helium have been considered [13]–[16]. One major benefit of using supercritical fluids is that the two-phase appearance is avoided in major cycle components [13], [15], thus simplifying their designs. The second benefit is that the increased operating temperature enhances the cycle efficiency. At the same time, by taking advantage of property changes near the critical point, the compression work is reduced, which also improves the efficiency [13]. The increased efficiency can be enhanced to approximately 45% [13], [15], in contrast to typical efficiencies of 33% for most current base load power cycles using the steam Rankine cycle.

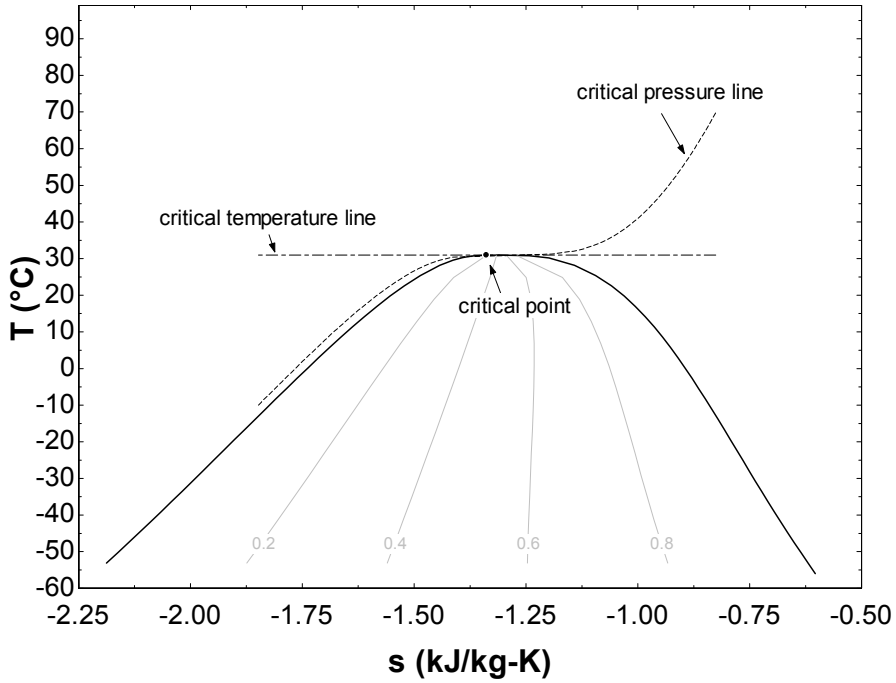

Figure 3 T-S diagram of CO_2

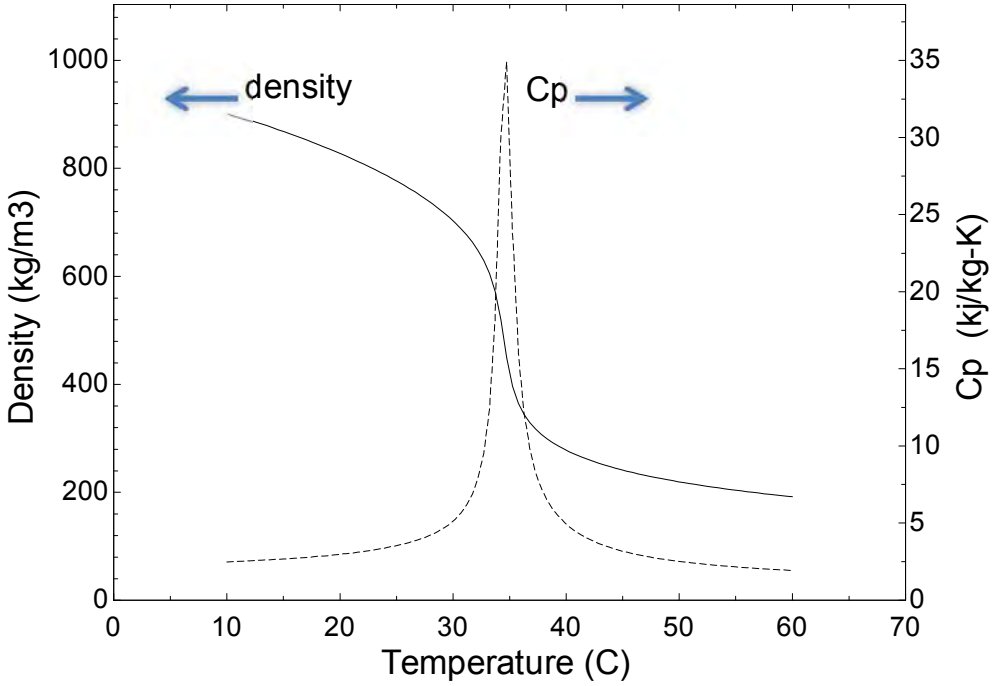

Figure 4 Property change of CO_2 at pseudo-critical point at 8 MPa

The S-CO_2 Brayton cycle is introduced as an example, as it has its own benefits compared to other supercritical fluid cycles. The lower critical pressure of CO_2 results in a lower pressure system, decreasing safety issues and saving costs significantly compared to a SCW cycle. The corrosion associated with S-CO_2

is also milder compare to SCW, due to the inactive chemical characteristic of CO_2. The high density of S-CO_2 makes the cycle components much smaller than a comparable supercritical helium cycle as shown in Figure 5. Overall, the S-CO_2 Brayton cycle shows the optimal performance among its competitors.

There is a family of S-CO_2 Brayton cycle layouts, including inter-cooling, re-heating, re-compressing, and pre-compressing. According to Dostal [13], the recompression cycle layout was found to yield the highest efficiency, while still retaining simplicity. Figure 6 shows a diagram of the recompression S-CO_2 Brayton cycle layout. This cycle layout improves efficiency by reducing the heat rejection to the precooler via introducing another compressor before the precooler [13]. The flow splits before entering the precooler and heat is only rejected from part of the flow. The thermodynamic states of component connections are indicated on a temperature-entropy diagram for CO_2 in Figure 7. In this cycle, the main compressor (compressor #1) compresses CO_2 to a high pressure (~20 MPa), according to the change from State 1 to State 2 in Figure 7. Due to the dramatic density change associated with the path from State 1 to State 2, the reduction of the compressor work is significant. Next, from State 2 to State 3, the low temperature recuperator heats the fluid. The fluid is then combined with the flow from compressor #2 and heated by the high temperature recuperator. After that, a heater, which may use fossil, nuclear or solar power, heats the flow to the highest temperature in the cycle. The high temperature and pressure working fluid then enters the turbine to produce power, according to the change from State 5 to State 6. Then, part of the residual heat is provided to the high temperature and low temperature recuperators. Before the flow dumps its residual heat into the precooler, part of the flow enters compressor #2.

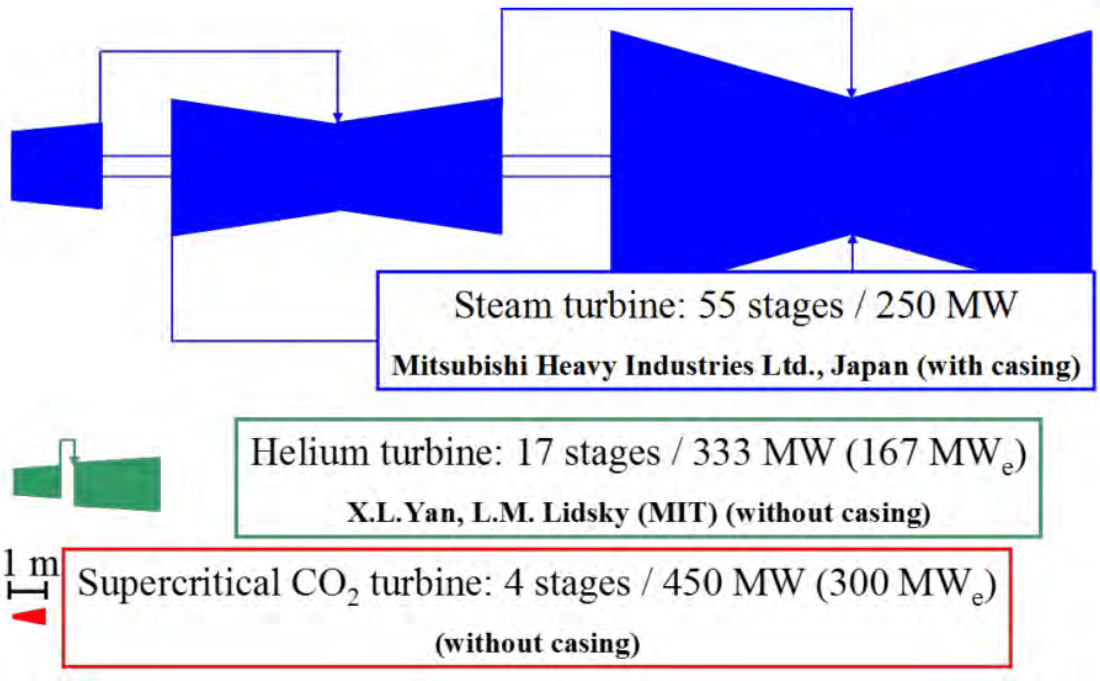

Figure 5 Size comparison of a steam turbine, a helium turbine, and a S-CO_2 turbine [13]

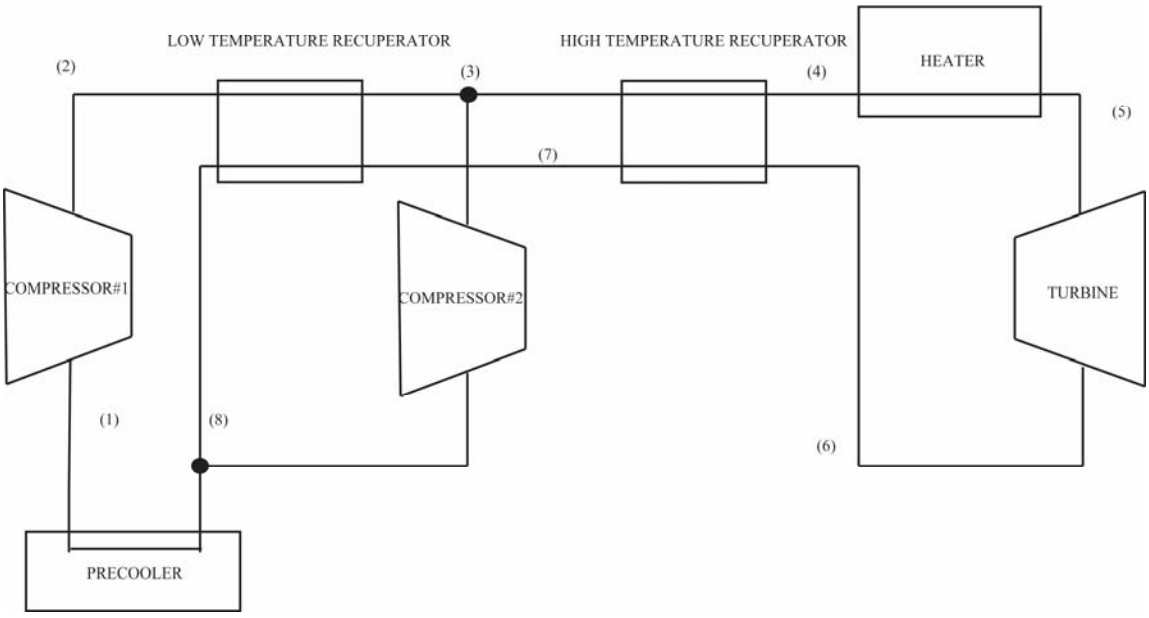

Figure 6 Recompression S-CO_2 Brayton cycle

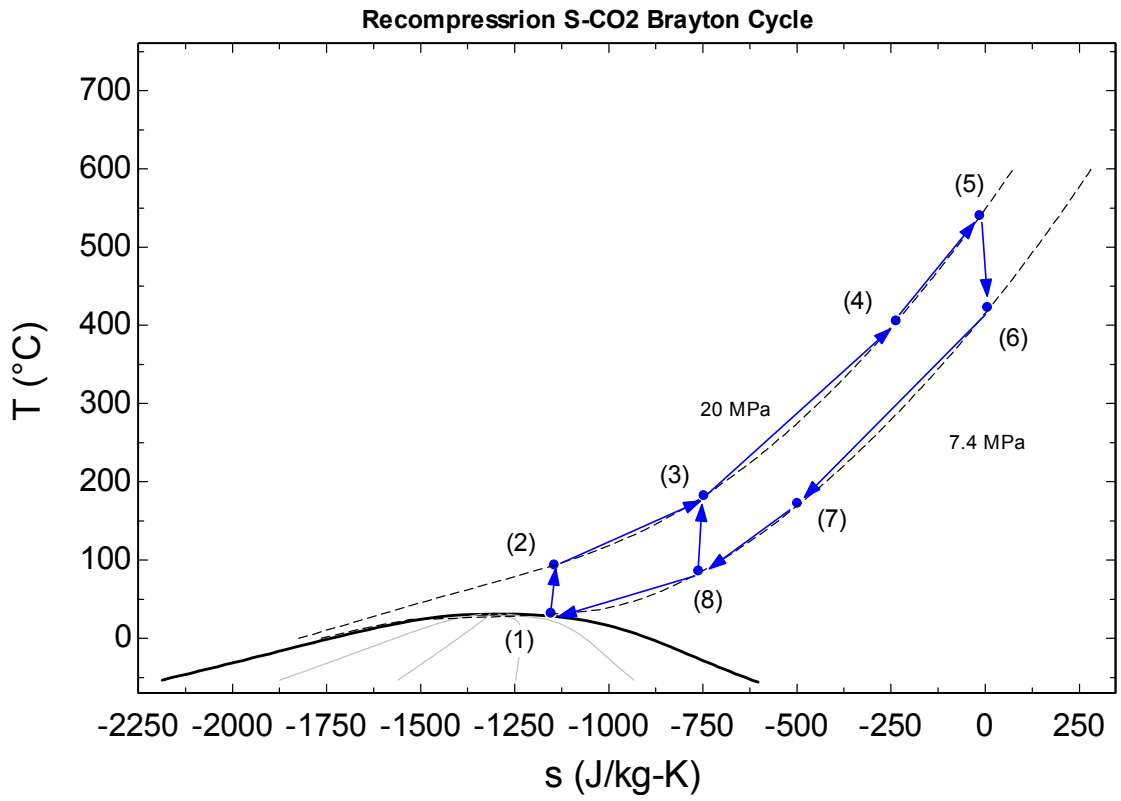

Figure 7 T-S diagram of recompression S-CO_2 Brayton cycle

2.2 CFD simulation of supercritical fluid flow

With the development of computer technology, CFD simulation for supercritical fluid flow in practical applications can now be performed. This section provides a background review of the past works with CFD simulation of supercritical fluid flow. Most of the previous works used either SCW or S-CO_2. As a result, the works of SCW are first introduced, then the works of S-CO_2.

Researchers conducted CFD simulations of SCW flow for different purposes. Schuler [17] used the ANSYS-FLUENT [1] with REFPROP [2] to study the SCW jet problem. The SCW jet was proposed as a possible alternative drilling technology. As a result, this research focused on the penetration length of the SCW jet. Farah [18] used ANSYS-FLUENT to study the SCW heat transfer problem in vertical bare tubes. Sensitivity analysis was performed for different parameters and turbulence models. Other researchers used another commercial CFD code, STAR-CCM+. Ampomah-Amoako [19] used this code along with

REFPROP to simulate SCW flow through a fuel rod subchannel. Chatharaju [9] used a steam table rather than REFPROP to simulate SCW choked flow. Her mass flow rate predictions have about 10% error compared with experimental data from Chen [20]. However, the two-phase modeling capability was not included in her methodology.

Flow of S-CO_2 was also studied by CFD codes. Yadav [21] used ANSYS-FLUENT along with REFPROP to simulate S-CO_2 in a natural circulation loop. New heat transfer and friction factor correlations were proposed based on modifications of the Dittus-Boelter and Filonenko correlations. Van Abel [22] used ANSYS-FLUENT with REFPROP to study S-CO_2 heat transfer in the Printed Circuit Heat Exchangers (PCHE). With a proper turbulence model and a precise geometric description, simulation results match experimental data. Serrano [23] used the same CFD code to study PCHEs, but properties were calculated from EES [5]. Guardo [24] used ANSYS-FLUENT with user-defined correlations for S-CO_2 properties. The particle-to-fluid heat transfer problem was studied; with a new heat transfer correlation proposed. Suo-Anttila [25] used another CFD code called C3D and implemented an interface to communicate with REFPROP. Three example problems, including both natural and forced circulations, were studied. Fairweather [26] developed a CFD model to simulate supercritical and two-phase CO_2 flow simultaneously. Fairweather used HEM and simulated the choked flow problem for a pipe break scenario. The near-field fluid dynamic and phase behavior after CO_2 is released from a supercritical state are studied. However, the mass flow rate predictions compared with experimental data was not presented in this work.

In the last two paragraphs, CFD codes have been used as a basic tool to study supercritical fluid flow. However, all of the works mentioned above, except Fairweather [26], are limited to the single-phase and supercritical states, and none of them extends to the two-phase region. In a supercritical fluid power cycle, the fluid in most components is in a supercritical state, but the two-phase scenario may appear under some circumstances, such as in gas relief valves, in pipe break scenario, etc. As a result, all methods discussed in the last two paragraphs, except Fairweather [26], cannot solve the problem in this research. With HEM implemented, the developed methodology can perform CFD simulations for supercritical and two-phase

flow simultaneously. The difference between this research and Fairweather [26] is that this research focuses on the prediction of mass flow rate, which is not presented in Fairweather's work.

2.3 Geometry 1: Orifices

The first example geometry is the orifice. In this study, the high-pressure supercritical fluid flows through an orifice to a low-pressure environment. As the downstream pressure decreases, the mass flow rate through this orifice reaches its maximum value at a certain point where the velocity at the orifice equals to the local sound speed. This mass flow rate is referred as the choked flow rate. This phenomenon also goes by several other names, such as critical flow. To avoid ambiguity, it is referred as "choked flow" throughout this document. As in this research, the upstream condition is in a supercritical state; this problem is also referred as "supercritical fluid choked flow." Two-phase scenario may appear as the downstream condition enters the two-phase region.

2.3.1 Isentropic model

Before reviewing the work related to the supercritical fluid choked flow problem, a theoretical model could be introduced first to build a simple concept. Many researchers studied this problem based on the isentropic model. Because pressures and entropies are used to determine thermodynamic states, the HEM assumption is inherently used for two-phase states. The remaining part gives a detailed description of this model. First, the upstream and downstream entropies are assumed to be equal (Equation 1). As the upstream and downstream pressures are given, Equation 2 and 3 determine the enthalpies. At the same time the upstream velocity is assumed to be zero. The downstream velocity can be calculated based on the energy conservation in Equation 4. Finally, Equation 5 determines the mass flow rate.

$$s_{upstream} = s_{downstream} \quad \textbf{1}$$

$$h_{upstream} = h(fluid, P_{upstream}, s_{upstream}) \quad \textbf{2}$$

$$h_{downstream} = h(fluid, P_{downstream}, s_{downstream}) \quad \textbf{3}$$

$$h_{upstream} = h_{downstream} + \frac{1}{2} v_{downstream}^2 \quad \textbf{4}$$

$$\dot{m} = \rho_{downstream} v_{downstream} A \quad \textbf{5}$$

In this model, the mass flow rate initially increases as the downstream pressure decreases. When the downstream pressure reaches a certain point, further reducing it predicts a reduced mass flow rate. However, this behavior is not physical, and the mass flow rate remains constant once it reaches its maximum value. Due to the isentropic assumption, this model predicts a higher mass flow rate than real situations. To account for the non-isentropic behavior, a discharge coefficient is defined as the ratio of the actual to the isentropic flow rates, as presented in Equation 6.

$$DC = \frac{\dot{m}_{actual}}{\dot{m}_{is}} \quad \textbf{6}$$

2.3.2 Experiments and simulations of supercritical fluid choked flow

The following paragraph describes the experiments related to the supercritical fluid choked flow problem. Mignot [27], Chen and Liu [25], [26], Zhang and Yang [35], [36], and Fairweather [26] conducted S-CO_2 choked flow experiments. Figure 8 and Figure 9 show the experiment facilities of Mignot [27] and Fairweather [26]. However, experimental data from these facilities are not used to validate the proposed methodology, as their downstream conditions were not controlled. Chen [20], [32] conducted a SCW choked flow experiment, which is shown Figure 10.

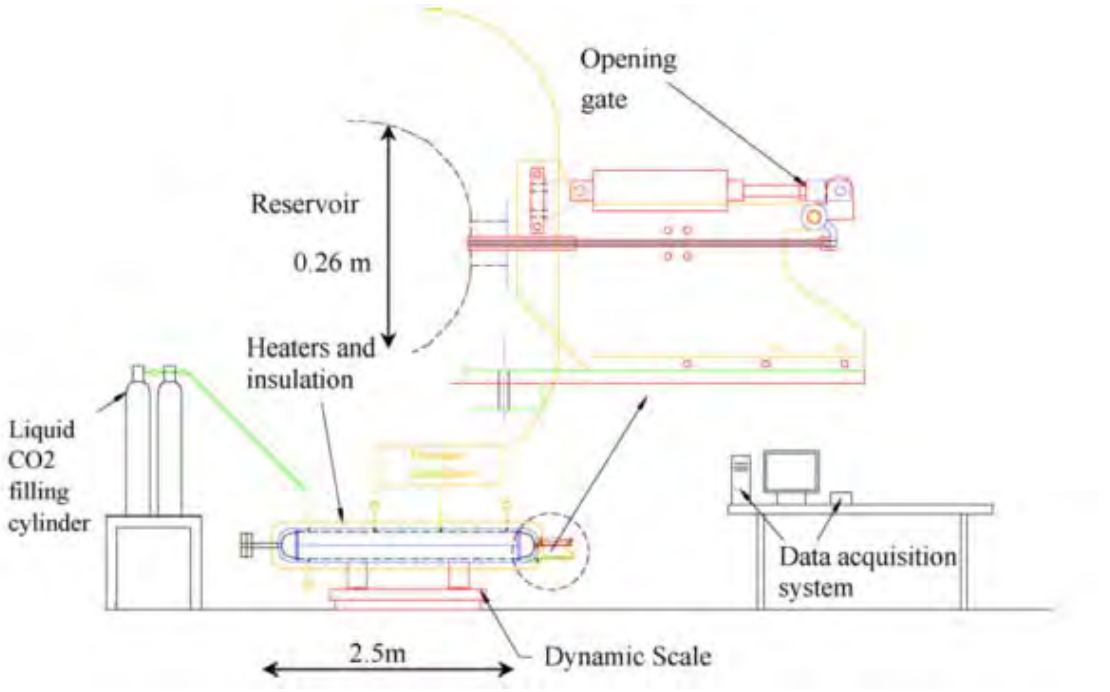

Figure 8 S-CO_2 choked flow experiment by Mignot[27]

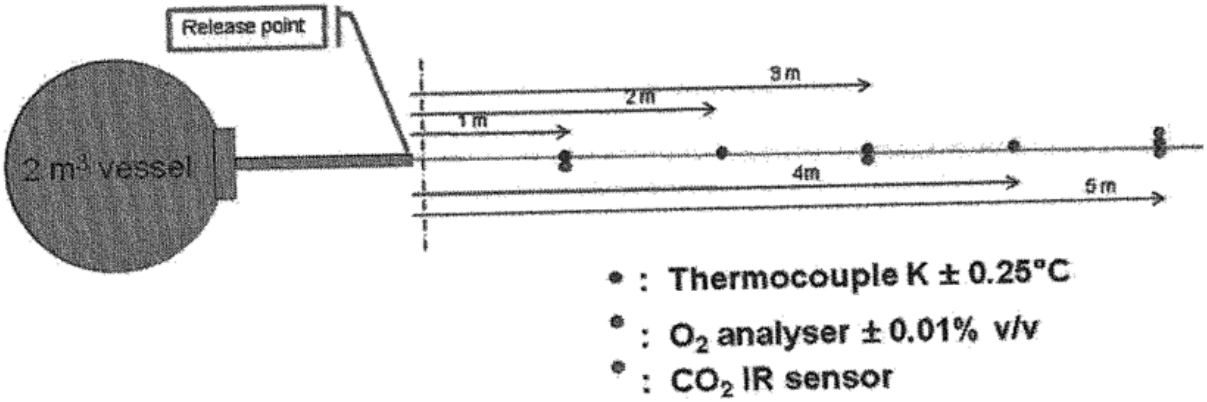

Figure 9 S-CO_2 release test rig by Fairweather [26]

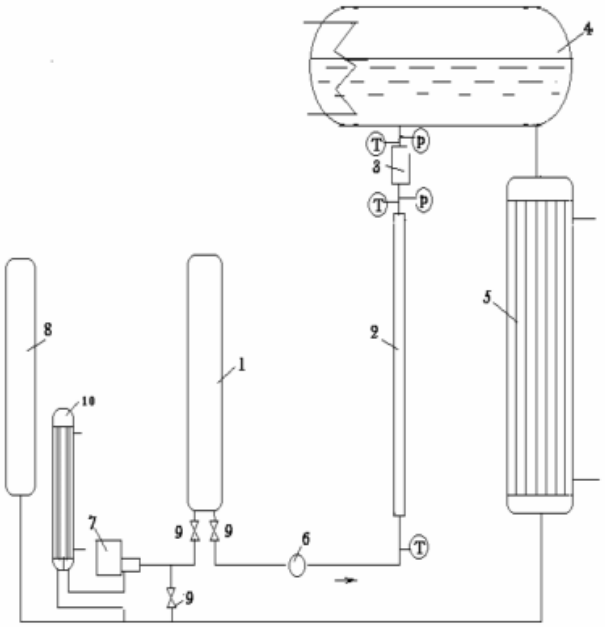

Figure 10 SCW choked flow experiment by Chen [20], [32]

Concerning the CFD simulations of supercritical fluid choked flow, Chatharaju [9] used STAR-CCM+ to study SCW flow through orifices. The experimental data from Chen [20] were used for validation by Chatharaju. About 10% prediction error of the choked flow rate was noticed from most cases considered. Two reasons may be the causes of error. First, the fluid properties were obtained from a steam table, which can be inaccurate, especially near the critical point. Second, Chatharaju used the experimental data from Chen [20][32], which used pressure and temperature to determine the upstream conditions. However, if the upstream state is near the pseudo-critical point, the density change associated with a temperature disturbance is significant. As a result, if the thermocouples in the experiment were not well calibrated or even have a small uncertainty, the upstream density can have a large deviation. This is the reason in this research the upstream condition is determined by pressure and density rather than pressure and temperature. Fairweather [26] developed a CFD model to simulate S-CO_2 flow through orifices. Due to the possible appearance of a two-phase condition, HEM was applied to calculate two-phase properties. However, Fairweather did not present the comparison of predicted mass flow rates and experimental measurements.

2.4 Geometry 2: Labyrinth seals

The second geometry of interest is the labyrinth seal. There are several reasons to study labyrinth seals. First, without too much change of current test facility, experiments of labyrinth seals can be conducted. Second, labyrinth seals have been used in various turbomachinery applications, or as a base design for more advanced seal designs. For example, the SNL S-CO_2 Brayton cycle experiment [15] used a stepped labyrinth seal for the compressor as shown in Figure 11.

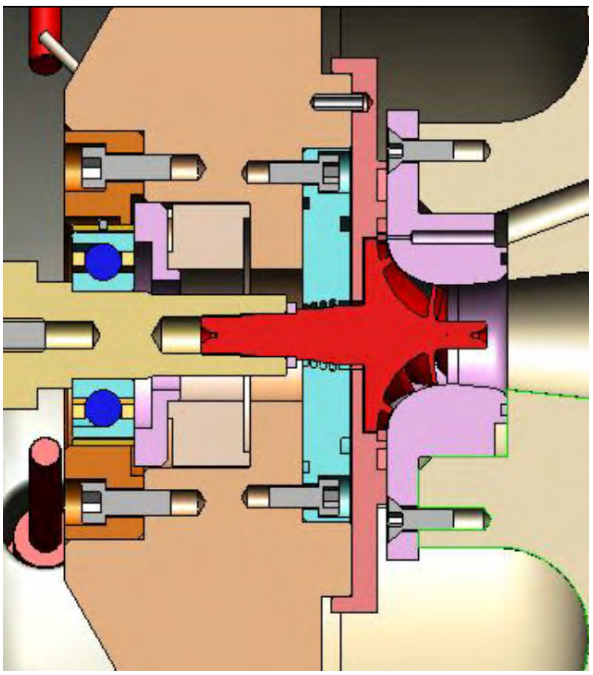

Figure 11 Seal of compressor in SNL S-CO_2 Brayton cycle experiment [15]

The idea of using labyrinth seals for turbomachinery has been around for a long time. From Sneck's [33] review paper, Parsons [34], [35] first introduced the idea of labyrinth seals. The idea was to interpose a tortuous flow path between high and low pressure regions by means of a series of non-contacting restrictors and separating cavities [33]. By this method, the pressure head is converted into kinetic energy and dissipated by the eddy in these cavities. After Parsons's study, researchers studied labyrinth seals from different perspectives. Several works are mentioned here as milestones. In the pioneering paper by Martin [36], labyrinth seals were considered to be a series of discrete throttling processes. Egli [37] modified Martin's model by introducing a kinetic energy carry-over coefficient, which is determined empirically.

This coefficient represents the portion of kinetic energy carried from one cavity to the next. Egli also noticed that since the pressure drop across each restrictor increases, the last restrictor is the first to reach the choked flow condition. Hodkinson [38] assumed a conically shaped stream in each cavity from a fluid mechanical point of view. The expansion angle of this conically shaped stream determines the carry-over coefficient in Egli's model.

Eldin [39] conducted the most recent and significant work on labyrinth seals. He mentioned that increasing the seal blade thickness reduces leakage by the largest amount (but the total length is changed). Increased eccentricity leads to an increased leakage rate, but this effect is only significant at a low Reynolds number. The effect of the cavity height was minor compared to the seal blade thickness although there does exist an optimum cavity height leading to a minimum leakage rate.

Witting [40], Rhode [41], and Schramm [42] used CFD codes to study labyrinth seals. They used CFD codes to perform optimization for labyrinth seals using the ideal-gas model. Suryanarayanan [43], using the ideal-gas model, on the other hand presented a new model to calculate the carry-over coefficient in Hodkinson's model [38]. Jiang [44] presented a numerical study on labyrinth seals for SCW. This research used the finite element method to solve fluid dynamic equations to find the rotordynamic coefficients. Jiang focused on the steam forcing induced by the leakage and studied the effect from different parameters like tooth number, seal clearance, etc. However, the leakage rate prediction and two-phase modeling capability were not mentioned.

2.5 Geometry 3: Valves

The third geometry of interest is the valve. There are two reasons to study valves. First, they are relative simpler than other parts in the cycle and much less computational resources are needed to study them. Second, at this point, there is no clear understanding of valves' behavior for supercritical fluid flow. As valves are widely used in supercritical fluid power cycles, it is essential to know valves' performance. Only S-CO_2 is used in this study, as experimental data are only available for S-CO_2 currently.

2.5.1 S-CO_2 Brayton cycle control schemes

According to Dostal [13] and Moisseytsev [45], valves are used to control the S-CO_2 Brayton cycle. In Dostal's discussion, three types of control schemes are adopted for the S-CO_2 Brayton cycle. They are bypass control, inventory control, and temperature control. In bypass control, regulating the mass flow rate through major components controls the power output. Inventory control uses one or several inventory tanks to control the mass of working fluid in the cycle. Temperature control changes the turbine inlet temperature by regulating the power level of the coupled heat source. As temperature control does not utilize valves, it is not discussed in this research.

In both bypass and inventory controls, valves change the flow path. In bypass control, valves are placed to bypass the major components, such as turbine, compressor, recuperator, and cooler. In inventory control, inventory tank reduce or add inventory into the cycle through inventory inlet or outlet valves. As a result, it is important to know the valve characteristics with the fluid of S-CO_2. In this research, the cycle design by Moisseytsev [45] is used as an example to help valve selection. There are five valves in Moisseytsev's design as shown in Figure 12. They are Turbine Bypass Valve (TBPv), Recuperator Bypass Valve (RBPv), Cooler Bypass Valve (CBPv), Inventory tank Inlet Valve (INVIv), and Inventory tank Outlet Valve (INVOv). Apparently, TBPv, RBPv, and CBPv are for bypass control, and INVIv and INVOv are for inventory control.

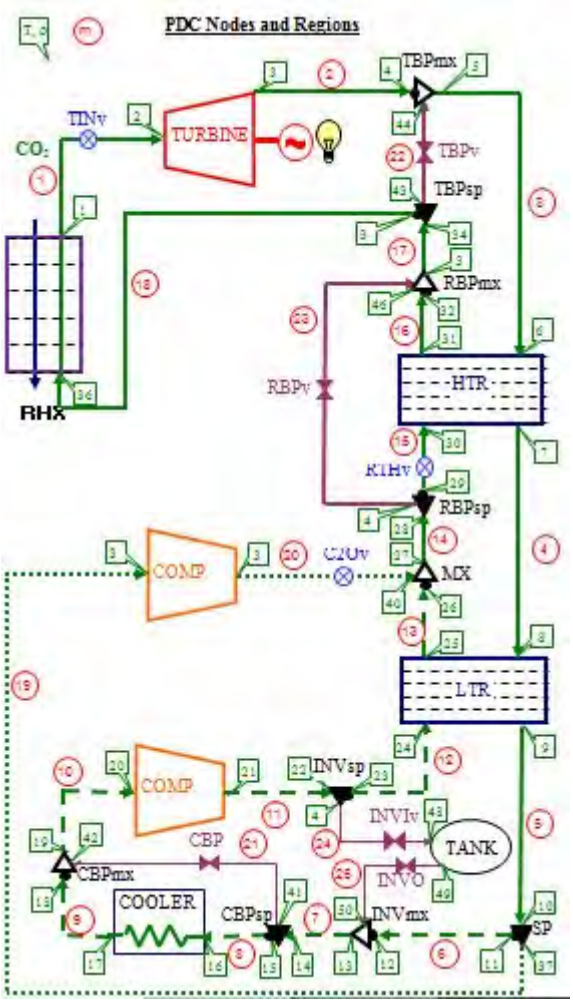

Figure 12 S-CO_2 Brayton cycle design by Moisseytsev [45]

2.5.2 Valve selection

In order to select proper valves, it is important to determine their types and sizes. For better controlling purpose, it is proposed to use the globe type for all valves. The remaining issue is to determine their sizes. If a valve is sized too small, the maximum amount of flow through the valve is limited and inhibits the system function. If a valve is sized too large, the user must bear the added cost of installing a larger valve. Another major disadvantage is that the entire flow control may be accomplished in the first half of the stroke, meaning that a minor change in position may cause a large change in flow, thus significantly reducing sensitivity. In addition, because regulation occurs in the first half of the stroke, flow control is difficult when regulating element is operating close to the seat. The ideal situation is to utilize the full range

of the stroke while producing the desired flow characteristics and maximum flow output [46]. However, valves are rarely undersized because of the number of safety factors built into the user's service conditions and the manufacturer's sizing criteria. Because of these safety factors, a large number of valves actually end up being oversized. Although not ideal, an oversized valve is still workable. The valve coefficient helps determining the valve size [46]. As specified by the Instrument Society of America, the simplified equation of the valve coefficient is

$$C_v = Q\sqrt{\frac{S_g}{\Delta P}} \qquad \textbf{7}$$

Where C_v = required valve coefficient for the valve

Q = flow rate (in gal/min)

S_g = specific gravity of the fluid

ΔP = pressure drop (psi)

However, the above correlation can only be used for incompressible fluid. To determine the valve coefficient for compressible fluid, like gas service, or use a manufacturer's provided valve coefficient to calculate the mass flow rate, a modified equation is needed as shown in Equation 8 [46].

$$w = 63.3F_pC_v\Upsilon\sqrt{xP_1\gamma_1} \qquad \textbf{8}$$

Where w = gas flow rate (lb/h)

F_p = piping-geometry factor

C_v = valve coefficient

Υ = expansion factor, $1-x/(3x_TF_k)$

x = pressure drop ratio, $(P_1-P_2)/P_1$

P_1= upstream absolute pressure (psia)

P_2= downstream absolute pressure (psia)

γ_1 = specific weight at inlet service condition (lb/ft^3)

F_k = ratio of specific heat transfer, k/1.40

k = ratio of specific heat of working fluid

x_T = terminal pressure drop ratio

As presented in Figure 13, a choked flow check is needed to use Equation 8. When $x < x_T F_k$, the flow is not choked, and the value of x is used in calculation. When $x > x_T F_k$, the flow is choked, and $x = x_T F_k$ is used in calculation. The application of Equation 8 is discussed with more detail in Skousen [46]. The values of x_T in [46] for globe valves are shown in Table I.

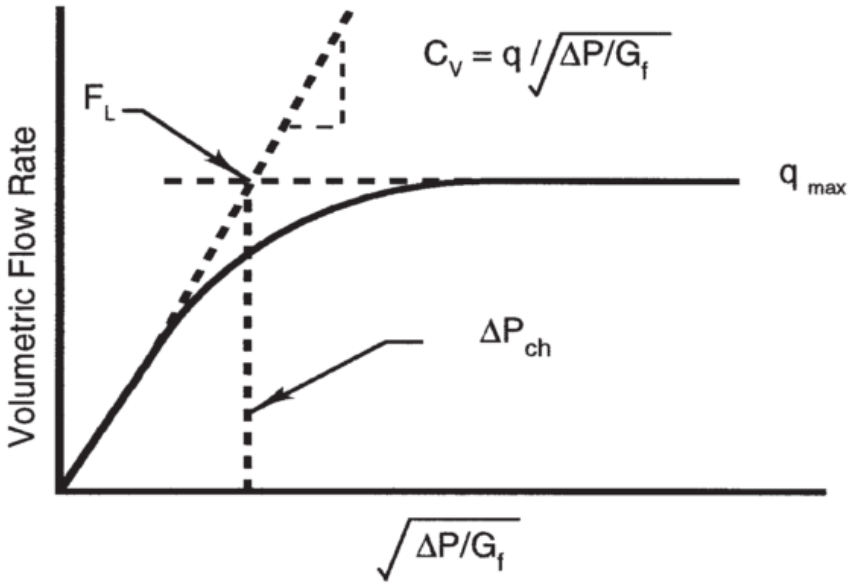

Figure 13 Maximum flow rate occurring due to choked conditions [46]

Table I Typical terminal pressure drop ratio [46]

Flow direction	Trim area	x_T
Over seat	Full area	0.70
Over seat	Reduced area	0.70
Under seat	Full area	0.75
Under seat	Reduced area	0.75

It is proposed to improve the existing gas service valve model by changing the choked flow check method. The traditional method uses an empirical coefficient, which may not be applicable to S-CO_2 conditions.

The proposed modification is to use the isentropic choking point, which is determined by the isentropic model introduced in Section 2.3.1.

After the required valve coefficient is calculated, the user could look up the manufacturer's table, and choose the smallest valve body that passes the required valve coefficient. At this point, the exit velocity should be calculated to ensure that it is within the velocity limits of Mach 0.5 for noise or Mach 1.0 for maximum velocity [46]. If the velocity is larger than Mach 1.0, than a larger valve body should be chosen. If the velocity is less than Mach 1.0 but larger than Mach 0.5, then the turbulence will most likely create noise in the valve, and preventative measures may be necessary, such as special trim, insulation or isolation of the valve. If the velocity is less than Mach 0.5, then this valve works for the purpose. To properly calculate the Mach number in the two-phase region, the sound speed is defined in Equation 9.

$$c^2 = \left.\frac{\partial P}{\partial \rho}\right|_s \tag{9}$$

Where c is sound speed (m/s), P is pressure (Pa), ρ is density defined from HEM (kg/m3), s is specific entropy (j/kg·K).

2.5.3 Cavitation

Another important concern is the cavitation phenomenon. When the fluid passes the narrowest point of the valve, the pressure decreases inversely as the velocity increases. If the pressure drops into the two-phase region, bubbles or droplets begin to form. As the fluid moves into the downstream, the pressure recovers to a certain extent. This increases the pressure, causing the bubbles or droplets to collapse. This two-step process, creation of the bubbles or droplets and their subsequent implosion, is called cavitation and is a leading cause of valve damage in the form of metal surface [46] as shown in Figure 14. Proper design of the system and the valve can help to eliminate or reduce cavitation.

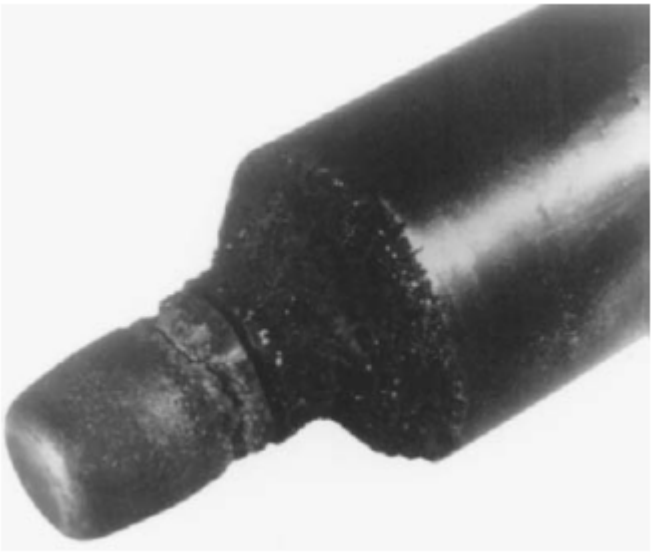

Figure 14 Plug damaged by cavitation [46]

2.6 Summary

This chapter presents the background and literature review of this research. The first section introduces supercritical fluids and their applications in power cycles. The definition of supercritical fluid is discussed first. Then different supercritical fluid power cycles are briefly introduced. The S-CO_2 Brayton cycle in its recompression version shows the optimum performance. After that, works about CFD simulations of supercritical fluid flow are reviewed. A lot of works in this area have been done and proved that the CFD method is a reliable approach. However, most of them did not combine supercritical and two-phase in simulations. The combination is a significant limitation and a complex problem. Then, a literature review of the study of three example geometries was presented. Previous works were introduced, along with their approaches and results.

3. Methodology development

This chapter introduces the methodology development of this research. The first two sections discuss solver modification and property module implementation. The remaining part covers geometry specification, boundary conditions, turbulence modeling, and issues of meshing. Figure 15 is a part of Figure 2, and shows the outline of this chapter.

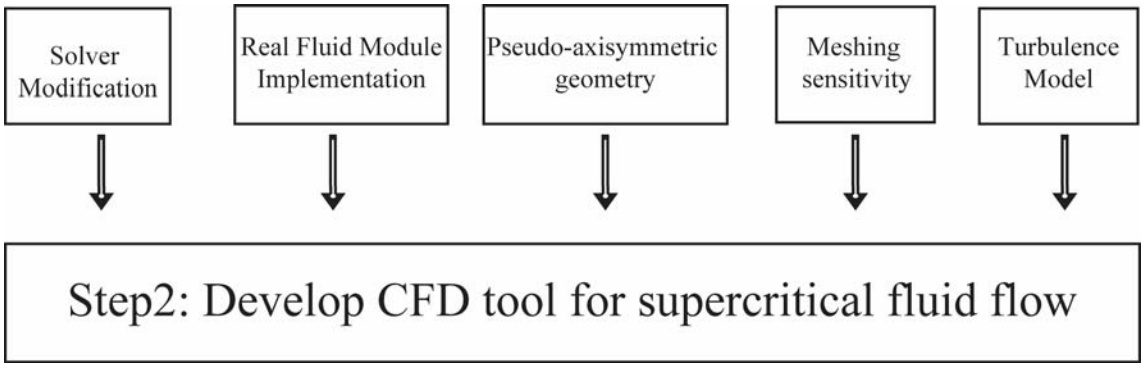

Figure 15 Flow chart of methodology development

3.1 Compressible SIMPLEC solver in OpenFOAM

The steady-state single-phase compressible solver *rhoSimplecFoam* in OpenFOAM was used for this research. This solver uses the *SIMPLEC* [47] algorithm to solve the Navier-Stokes equations for steady-state single-phase compressible flow. The name *SIMPLE* [48] is an acronym for Semi-Implicit Method for Pressure Linked Equations. Instead of solving the continuity equation, the *SIMPLE* algorithm solves a pressure correction equation based on the combination of continuity and momentum equations. The *SIMPLEC* [47] algorithm is a permutation of the *SIMPLE* algorithm, and C stands for Coupling. It basically follows the same procedure of the *SIMPLE* algorithm with minor modifications; however, it exhibits better robustness and stability in some applications [1], [47]. The steady-state single-phase compressible Reynolds-Averaged Navier-Stokes (RANS) equations are shown in Equation 10, 11, 12.

Continuity equation:

$$\nabla \cdot \left(\rho U \right) = 0 \quad \textbf{10}$$

Momentum equation:

$$\nabla \cdot \left(\rho UU \right) = -\nabla P + \nabla \cdot \left(\left(\mu_m + \mu_t \right) \nabla U \right) \quad \textbf{11}$$

Energy equation:

$$\nabla \cdot \left(\rho Uh \right) + \nabla \cdot \left(\rho U \frac{U^2}{2} \right) - \nabla \cdot \left(\alpha_{eff} \nabla h \right) = 0 \quad \textbf{12}$$

In the rest of this subsection, the SIMPLEC algorithm in *rhoSimplecFoam* is introduced with great details. The momentum equation can be re-written in a semi-discretized form in Equation 13. The right hand side of H(U) in Equation 13 represents the matrix coefficients of the neighbouring cells multiplied by their velocity as shown in Equation 14. As a result, there is no pressure gradient in H(U). Then, the continuity equation is discretized in Equation 19. Where S is outward-point face area vector; U_f is the velocity on the face; ρ_f is the density on the face. The velocity on the face is obtained by interpolating the semi-discretized form of the momentum equation as presented in Equation 16. By substituting this equation into the discretized continuity equation obtained above, the pressure equation could be obtained (Equation 17). Then the momentum and pressure equations could be solved iteratively until convergence criteria are reached. After pressure-velocity coupling is finished, the energy equation (Equation 12) could be solved.

$$\alpha_p U_p = H\left(U\right) - \nabla P \Leftrightarrow U_p = \frac{H\left(U\right)}{\alpha_p} - \frac{\nabla P}{\alpha_p} \quad \textbf{13}$$

$$H\left(U\right) = -\sum_n \alpha_n U_n \quad \textbf{14}$$

$$\nabla \cdot \left(\rho U \right) = \sum_f \left(S \cdot U_f \cdot \rho_f \right) = 0 \quad \textbf{15}$$

$$U_f = \left(\frac{H(U)}{\alpha_p}\right)_f - \left(\frac{\nabla P}{\alpha_p}\right)_f \quad \textbf{16}$$

$$\nabla \cdot \left(\frac{\rho}{\alpha_p}\nabla P\right) = \nabla \cdot \left(\frac{\rho H(U)}{\alpha_p}\right) = \sum_f S\left(\frac{\rho H(U)}{\alpha_p}\right)_f \quad \textbf{17}$$

3.2 Modification to energy equation

The *rhoSimplecFoam* solver could not be directly used for this problem, as it uses molecular thermal diffusivity, which is not defined in the two-phase region. Equation 18 shows the energy equation in the unmodified solver, using an effective thermal diffusivity, which is a combination of turbulence and molecular thermal diffusivity (Equation 19). Equation 18 can be transformed to Equation 20. Through Equation 20 and 23 with the ideal gas assumption (Equation 22), the original form of the energy equation can be derived as presented in Equation 23. In the modified solver, the energy equation is changed to the form of Equation 23 to avoid using molecular thermal diffusivity α_m, which is not defined in the two-phase region.

$$\nabla \cdot (\rho U h) + \nabla \cdot (\rho U \frac{U^2}{2}) - \nabla \cdot (\alpha_{eff} \nabla h) = 0 \quad \textbf{18}$$

$$\alpha_{eff} = \alpha_m + \alpha_t \quad \textbf{19}$$

$$\nabla \cdot (\rho U h) + \nabla \cdot (\rho U \frac{U^2}{2}) - \nabla \cdot ((\alpha_m + \alpha_t) \nabla h) = 0 \quad \textbf{20}$$

$$\nabla \cdot (\rho U h) + \nabla \cdot (\rho U \frac{U^2}{2}) - \nabla \cdot ((\alpha_t + \kappa / Cp) \nabla h) = 0 \quad \textbf{21}$$

$$h = T \cdot Cp \quad \textbf{22}$$

$$\nabla \cdot (\rho U h) + \nabla \cdot (\rho U \frac{U^2}{2}) - \nabla \cdot ((\alpha_t \nabla h) = \nabla \cdot (\kappa \nabla T) \quad \textbf{23}$$

3.3 Real fluid module

A real fluid module is needed to provide properties for supercritical fluid. The NIST standard reference database REFPROP [2] was initially used to provide the fluid properties. REFPROP is based on the most accurate pure fluid and mixture models currently available. It implements three models for the thermophysics properties of pure fluids: equation of state explicit in Helmholtz energy, the modified Benedict-Webb-Rubin equation of state, and an extended corresponding states (ECS) model [2]. Density and temperature are obtained from these models with calculated pressure and enthalpy. Viscosity and thermal conductivity are modeled with either fluid-specific correlations, an ECS model, or in some cases the friction theory model [2]. However, REFPROP slows down simulations significantly. Fluid properties are currently calculated using the FIT software library published by Northland Numerics [3], which provides an interpolated representation of properties with the underlying property data obtained from REFPROP. In this way the FIT code calculates fluid properties much faster than REFPROP with an acceptable deviation. Figure 16 shows the comparison of FIT and REFPROP property calculation for CO_2. According to Northland Numerics [3], each plot is based on one million points, distributed evenly from 240 K to 1500 K and from 1 kPa to 100 MPa. As can be seen in Figure 16, the maximum difference is less than the uncertainty of the equation of state.

To use the FIT code, an interface was created to link the external property module with OpenFOAM. This interface was embedded in the *hRhoThermo* thermophysics module. The original code of this module is replaced by user specified external subroutines. As a result, when solver calls this thermophysics module, it uses user defined property subroutines instead of its default subroutines.

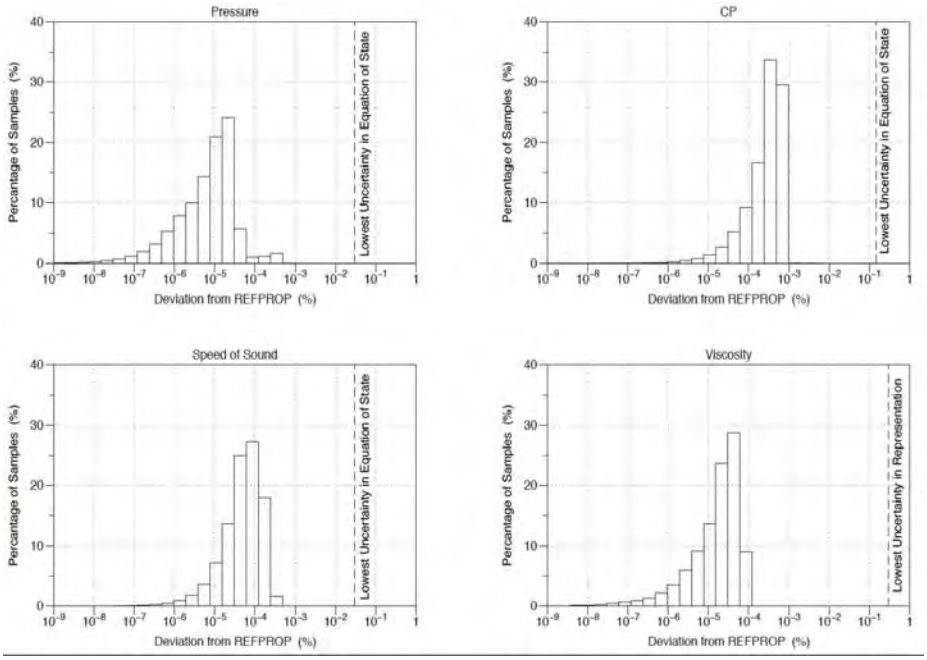

Figure 16 Comparison of FIT and REFPROP for CO_2 [3]

3.4 Two-phase modeling

Under certain circumstances, the downstream condition of tested geometry enters the two-phase region, resulting in flashing in the flow domain. Therefore, it is necessary to implement a two-phase modeling capability in the developed methodology. Three types of two-phase models are discussed in this section. The first type is the two-fluid model, which represents two phases separately. This type of model is expressed in terms of two sets of conservation equations governing the balance of mass, momentum, and energy in each phase. The second type is the drift-flux model, which treats two phases as a mixture. The two-phase interactions are modeled. The third one is the Homogeneous Equilibrium Model (HEM). In this model, two phases are treated as a mixture, and two-phase interactions are completed neglected. In the following discussion, equations of these models are presented and compared, and HEM is selected for simplicity. Dimensionless analysis is performed afterward to validate HEM's usage in this problem.

3.4.1 Two-fluid model, Drift-flux model, HEM

The two-fluid model gives a more complete description of two-phase flow, compare with other two types of models. However, according to Ishii [49], if one is more concerned with the total response of the two-

phase mixture in a system rather than the local behavior of each phase, the drift-flux model is simpler and in most cases effective for solving problems. In this research, pressure drop and corresponding mass flow rate across the examined geometries is the major concern, and phase distribution is less interested. Using the two-fluid model brings unnecessary complications. As a result, the two-fluid model is not discussed here with too much detail. However, Equation 24, 25, 26, 27 represent the two-fluid model excluding the energy equation. The subscript k represents each individual phase.

$$\frac{\partial \alpha_k \rho_k}{\partial t} + \nabla \cdot \left(\alpha_k \rho_k U_k \right) = \Gamma_k \tag{24}$$

$$\frac{\partial \alpha_k \rho_k U_k}{\partial t} + \nabla \cdot \left(\alpha_k \rho_k U_k U_k \right) = -\nabla \alpha_k P_k + \nabla \cdot \left(\alpha_k \left(\mu_m + \mu_t \right) \nabla U_k \right) + M_k \tag{25}$$

$$\sum_k^2 \Gamma_k = 0 \tag{26}$$

$$\sum_k^2 M_k = M_m \tag{27}$$

The drift-flux model, which is relative simpler than the two-fluid model, is represented by Equation 28, 29, 30. In the drift-flux model, there are two continuity equations and one momentum equation. The second continuity equation (Equation 29) represents the second phase or dispersed phase. The momentum equation (Equation 30) describes interactions of two phases with the drift and interface terms. When comparing the momentum equations of drift-flux model and HEM (Equation 31), drift and interface terms are the difference. The subscript m represents mixture properties, but for viscosity it stands for molecular properties. Subscript 1 represents the carrier phase, while subscript 2 represents the dispersed phase.

$$\frac{\partial \rho_m}{\partial t} + \nabla \cdot \left(\rho_m U_m \right) = 0 \tag{28}$$

$$\frac{\partial \alpha_2 \rho_2}{\partial t} + \nabla \cdot \left(\alpha_2 \rho_2 U_m \right) = \Gamma_2 - \nabla \cdot \left(\frac{\alpha_2 \rho_1 \rho_2}{\rho_m} V_2 \right) \tag{29}$$

$$\frac{\partial \rho_m U_m}{\partial t}+\nabla\cdot\left(\rho_m U_m U_m\right)=-\nabla\left(P_m\right)+\nabla\cdot\left(\left(\mu_m+\mu_t\right)\nabla U_m\right)$$
$$\underbrace{-\nabla\cdot\left(\frac{\alpha_2}{1-\alpha_2}\frac{\rho_1\rho_2}{\rho_m}V_2V_2\right)}_{\text{Drift term}}+\rho_m g+\underbrace{M_m}_{\text{Interface term}} \quad \textbf{30}$$

Where $M_m=2H_{21}\sigma\nabla\alpha_2+\sum_j 2a_{ij}\left(H_{21}-\overline{H_{21}}\right)\sigma n_1$

$$\frac{\partial \rho_m U_m}{\partial t}+\nabla\cdot\left(\rho_m U_m U_m\right)=-\nabla P_m+\nabla\cdot\left(\left(\mu_m+\mu_t\right)\nabla U_m\right) \quad \textbf{31}$$

In Equation 30, drift term represents the momentum interaction due to difference in density and velocity. While, interface term represents the momentum interaction due to interface movement. These two terms can be scaled by two non-dimension numbers, drift number (Equation 32) and surface number (Equation 33). Moreover, in Equation 31, the gravitational force is also neglected. This term can be scaled by the Fraud number represented by Equation 34. According to Ishii [49], when drift number and surface number are much less than unity, drift and interface terms can be neglected. And when the Fraud number is much larger than unity, the gravitational term can be neglected. In the following two subsections, drift and surface number are calculated with some simple analytical models. The calculation of Fraud number is not given, as it can be easily proved to be much larger than one.

$$N_D=\frac{\rho_g V_{12}}{\rho_m u_m} \quad \textbf{32}$$

$$N_\sigma\equiv\frac{2H_{21}\sigma}{\rho_m u_m^2}=\frac{2\sigma}{\rho_m u_m^2 R} \quad \textbf{33}$$

$$N_{Fr}=\frac{u_m^2}{gL} \quad \textbf{34}$$

3.4.2 Drift number

The drift number is estimated in this part. The isentropic model (Equation 1-5) combined with Moody's [50] slip ratio model (Equation 35) are used to calculate drift number quantitatively. According to Moody's deduction, using this slip ratio results in the maximum mass flow rate for two-phase mixture flow [50]. The void fraction is calculated by Equation 36. The mass flow rate is conserved by isentropic model using Equation 37. For an example case with an upstream condition of 7.7 MPa, 498 kg/m^3 and an outlet pressure is 6 MPa, the drift number is 0.08. As drift number is much less than unity, drift term can be neglected. The detail of this calculation can be found in Appendix A.

$$S=\frac{u_g}{u_l}=\left(\frac{v_g}{v_l}\right)^{1/3}=\left(\frac{\rho_l}{\rho_g}\right)^{1/3} \tag{35}$$

$$\alpha=\frac{1}{1+\frac{1-x}{x}\frac{\rho_g}{\rho_l}S} \tag{36}$$

$$\rho_m u_m=\alpha\rho_g u_g+(1-\alpha)\rho_l u_l \tag{37}$$

3.4.3 Surface number

In order to calculate the surface number, the size of bubble/droplet should be determined. The classical nucleation theory [51] is used to determine the size of bubble/droplet. In this part, nucleus is referred to represent bubble or droplet for convenience. The classical nucleation theory is based on the capillary approximation, in which small portion of the new phase are treated as if they represent macroscopic regions of space [52]. It assumes the nucleus is spherical, and its free energy can be represented by two parts as show in Equation 38, where R is the nucleus radius, Δg is the free energy difference between nucleating phase and surrounding phase per unit volume, σ is the surface tension.

$$\Delta G=\frac{4}{3}\pi R^3\Delta g+4\pi R^2\sigma \tag{38}$$

At some nucleus radius, the free energy goes through a maximum, and so the probability of forming a nucleus goes through a minimum. And there is a least-probable nucleus occurs. This is called the critical nucleus and occurs at a critical nucleus radius. The critical nucleus is the smallest nucleus that can be seen in nucleation. Thus, using this critical nucleus radius gives the maximum value of the surface number. This critical nucleus radius can be calculated by taking a derivative of Equation 38 as shown in Equation 39. And the representation of the critical nucleus radius is shown in Equation 40.

$$\left.\frac{d\Delta G}{dr}\right|_{r=r^*} = 0 \tag{39}$$

$$r^* = -\frac{2\sigma}{\Delta g} \tag{40}$$

An example case is examined: CO_2 nucleate at the saturation point of 6 MPa. In this situation, the surface number is 0.002. As surface number is much less than unity, surface term can be neglected. Appendix A gives more detail of this calculation.

3.4.4 HEM implementation

From the discussion above, it is globally feasible to use the simplest two-phase model, i.e. HEM. Aaron [53], Fang [54], Payne [55] have also confirmed HEM's applicability to similar flow conditions. For more theoretical and local analysis, Trujillo [56] studied the departure from passive advection of small particles based on a Lagrangian framework. A localized indicator was proposed to determine passive particles advection. However, the density ratio in Trujillo's study is O (10^3). Therefore, more theoretical analysis should be performed to validate HEM's usage in this problem. For simplification, HEM was used for this research at present stage. HEM assumes two phases to have the same velocity, temperature and pressure [57]. The state of two-phase can be determined by pressure and enthalpy uniquely using Equation 41 (specific volume) and 42 (enthalpy).

$$v_{two-phase} = x \cdot v_{gas} + (1-x) \cdot v_{liquid} \tag{41}$$

$$h_{two-phase} = x \cdot h_{gas} + (1-x) \cdot h_{liquid} \quad \textbf{42}$$

For transport properties (e.g., viscosity and conductivity), the average value for a two-phase state can be based on area, mass or volume [57]. The developed methodology obtains two-phase transport properties based on the mass average using Equation 43 and 44. The flow in this problem is highly turbulent, making turbulent viscosity and diffusivity much larger than their molecular counterparts. As a result, different averaging method does not affect the bulk flow. However, in the near wall region, the molecular viscosity starts to make a difference, as turbulent effects become weaker. But the total mass flow rate is not affected either as the pressure drop is primarily due to form loss not wall shear stress.

$$\mu_{two-phase} = x \cdot \mu_{gas} + (1-x) \cdot \mu_{liquid} \quad \textbf{43}$$

$$\kappa_{two-phase} = x \cdot \kappa_{gas} + (1-x) \cdot \kappa_{liquid} \quad \textbf{44}$$

3.5 Pseudo-axisymmetric geometry and boundary conditions

Since example geometries are axisymmetric, 2D axisymmetric geometries are used to save computational time. As RANS turbulence model is used in this problem, and velocity gradient in azimuthal direction is zero, therefore the turbulence affect in azimuthal direction could be neglected. Therefore, the axisymmetric geometry could be used in this research. However, OpenFOAM does not have the ability to solve 2D problem in the cylindrical coordinate. Because it is designed for the Cartesian system [58], [59]. Therefore, the OpenFOAM community uses a pseudo-axisymmetric method. Figure 17 shows the pseudo-axisymmetric geometries used in simulations for circular and annular orifices.

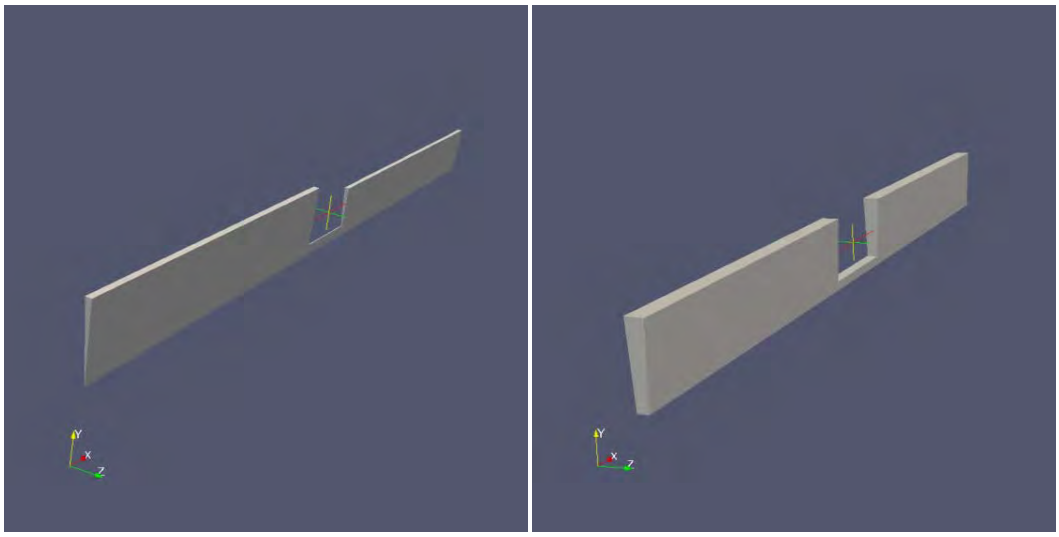

Figure 17 Pseudo-axisymmetric geometries for circular and annular orifices

Figure 18 and Figure 19 shows the front and axial views of computational domains for difference orifices, describing their boundary conditions as well. The 'wall' boundary condition means non-split and non-penetration for velocity, and zero-gradient for pressure. Due to the adiabatic assumption, zero heat flux is assumed at wall, which applies zero-gradient of temperature. This is achieved by the combination of zero-gradient for both pressure and enthalpy. The 'wedge' boundary condition is recommended in the OpenFOAM User Guide [58] for the pseudo-axisymmetric geometry when there is only one level of cells in the corresponding direction. It assumes the adjacent cell in azimuthal direction is the cell itself. Therefore, the 'wedge' boundary condition is actually a specialized periodic boundary condition designed for the pseudo-axisymmetric geometry. The 'empty' boundary condition makes the cell faces on that patch have a zero area, which means that there is no fluxes at this boundary, including both momentum and energy flux. It is recommended by the OpenFOAM User Guide [58] to use the 'empty' boundary condition at the axis of a pseudo-axisymmetric geometry. The cells on the axis degrade to wedged shaped blocks as the vertices on the axis collapse to one. However, other cells are still hexahedral. In this paragraph, only the computational domains and boundary conditions for orifices are discussed. The same boundary condition setting is also used for the study of labyrinth seals and valves.

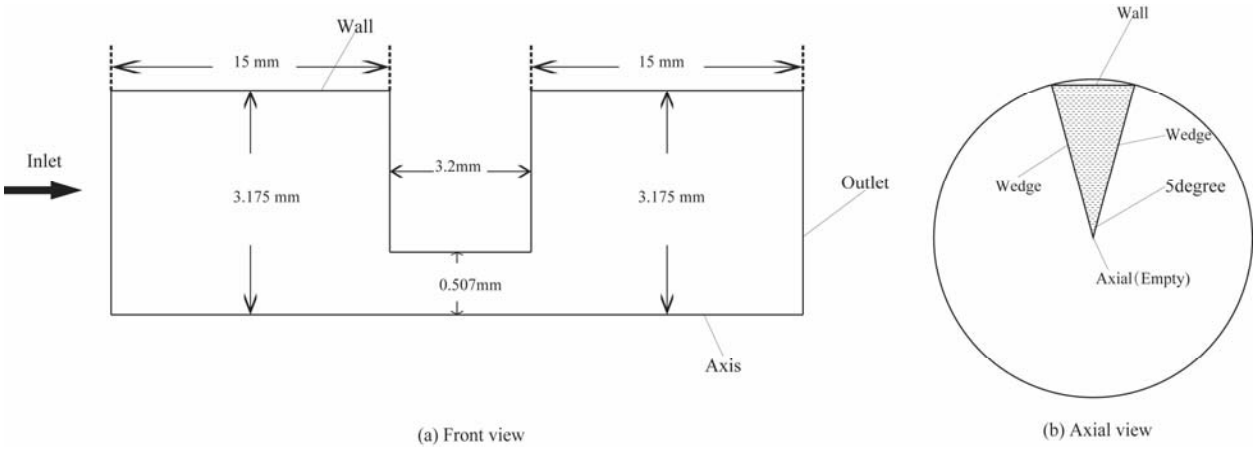

Figure 18 Computational domain and boundary conditions for circular orifice (not to scale) [60]

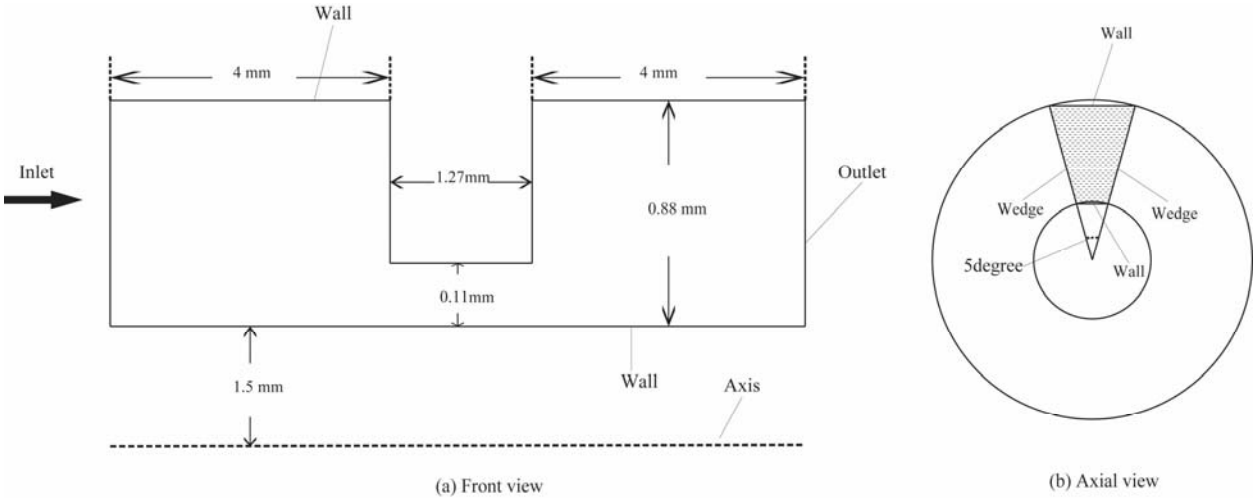

Figure 19 Computational domain and boundary conditions for short annular orifice (not to scale) [60]

3.6 Turbulence modeling

3.6.1 Choice of turbulence model

Turbulence should be modeled as it significantly affects the flow. The k-ω SST model was compared with the standard k-ε model for S-CO_2 flow. Due to the high Reynolds number (~200,000) encountered in this problem, both models predict similar mass flow rate. However, standard k-ε model brings better stability and robustness. The standard k-ε model also performs very well in a study by Qiu [61] for an engine nozzle for a similar flow condition. The equations and coefficients for these two turbulence models in OpenFOAM are presented as followed.

In the standard k-ε model

$$\frac{D\rho k}{Dt}=\nabla\left(\left(\frac{\mu_t}{\sigma_k}+\mu\right)\nabla k\right)+\rho P_k-\frac{2}{3}\rho k\nabla U-\rho\varepsilon \quad (45)$$

$$\frac{D\rho\varepsilon}{Dt}=\nabla\left(\left(\frac{\mu_t}{\sigma_\eta}+\mu\right)\nabla\varepsilon\right)+C_{\varepsilon 1}\frac{\rho P_k\varepsilon}{k}-\left(\frac{2}{3}C_{\varepsilon 1}+C_{\varepsilon 3}\right)\rho\varepsilon\nabla U-C_{\varepsilon 2}\frac{\rho\varepsilon^2}{k} \quad (46)$$

$$\mu_{\mathrm{t}}=C_\mu\frac{\rho k^2}{\varepsilon} \quad (47)$$

$$\alpha_{\mathrm{t}}=\frac{\mu_t}{\rho\cdot\mathrm{Pr}_{\mathrm{t}}} \quad (48)$$

Table II Coefficients for standard k-epsilon model in OpenFOAM

C_μ	$C_{\varepsilon 1}$	$C_{\varepsilon 2}$	$C_{\varepsilon 3}$	σ_k	σ_ε	Pr_{t}
0.09	1.44	1.92	-0.33	1.0	1.3	1.0

In the k-ω SST model

$$\frac{D\rho k}{Dt}=\nabla\left(\left(\alpha_k\mu_t+\mu\right)\nabla k\right)+\rho P_k-\frac{2}{3}\rho k\nabla U-\rho\beta^*\omega k \quad (49)$$

$$\frac{D\rho\omega}{Dt}=\nabla\left(\left(\alpha_\omega\mu_t+\mu\right)\nabla\omega\right)+\gamma\frac{\rho P_k\omega}{k}-\frac{2}{3}\rho\gamma\omega\nabla U-\rho\beta\omega^2-\rho\left(F-1\right)F \quad (50)$$

$$\mu_{\mathrm{t}}=\frac{\rho k}{\omega} \quad (51)$$

Where

$$F=\frac{2\alpha_{\omega 2}\left(\nabla k\square\nabla\omega\right)}{\omega},\alpha_k=F\alpha_{k1}+(1-F)\alpha_{k2},\alpha_\omega=F\alpha_{\omega 1}+(1-F)\alpha_{\omega 2},\gamma=F\gamma_1+(1-F)\gamma_2,\beta=F\beta_1+(1-F)\beta_2$$

Table III Coefficients for k-omega SST model in OpenFOAM

α_{k1}	α_{k2}	$\alpha_{\omega 1}$	$\alpha_{\omega 2}$	β_1	β_2	β^*	γ_1	γ_2	Pr_t
0.85034	1.0	0.5	0.85616	0.075	0.0828	0.09	0.5532	0.4403	1.0

Figure 20 describes the simulation data from the standard k-ε and k-ω SST turbulence models based on a short annular orifice with a smooth wall condition at an upstream condition of 10 MPa at 475 kg/m^3. In Figure 20, 'IS' represents data from the isentropic model, 'EXP' represents data from experiment, 'k-epsilon' represents the data from the standard k-ε model, and 'k-omega SST' represents the data from the k-ω SST model. Figure 21 presents the data from a medium length annular orifice with the k-ω SST turbulence model with 0.5 μm roughness at an upstream condition of 10 MPa at 325 kg/m^3. In Figure 20 and Figure 21, two turbulence models predict the mass flow rate with a very small difference. The geometry parameters for these annular orifices are presented in Section 5.1.

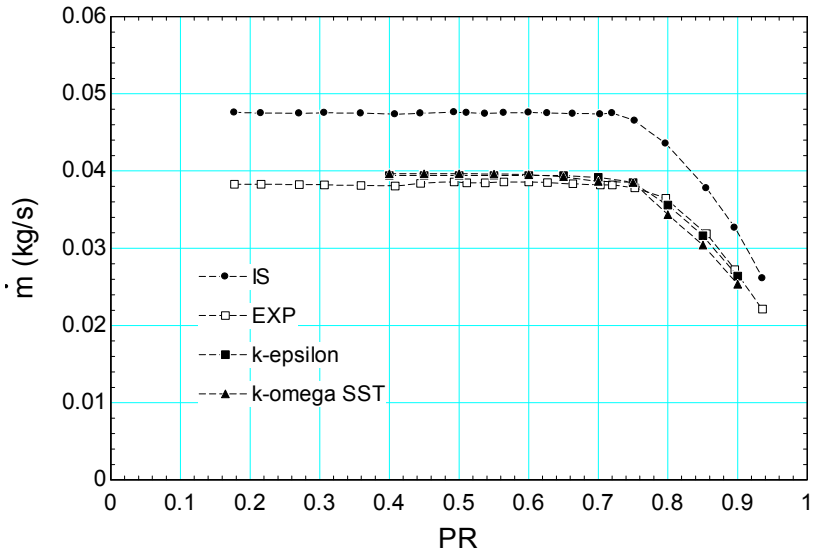

Figure 20 Short annular orifice data for comparison of standard k-epsilon and k-omega SST

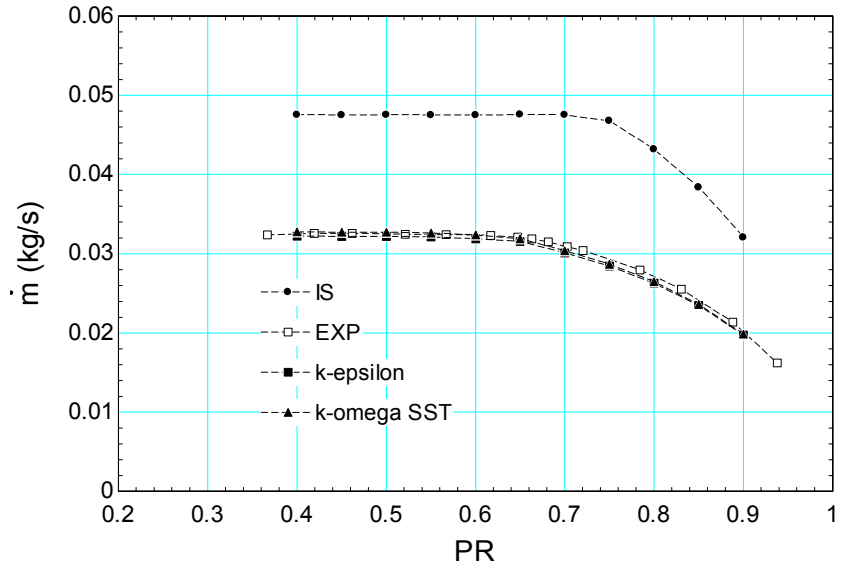

Figure 21 Medium annular orifice data for comparison of standard k-epsilon and k-omega SST

3.6.2 Turbulence Prandtl number

There is a lot of discussion on the constant Pr_t assumption in supercritical fluid flow [62]–[65]. It is believed that the constant Pr_t assumption is not valid in supercritical fluid flow, and the value of Pr_t deviate from unity. However, in [65], the recommended value of Pr_t is not significantly deviate from unity. As a result, three different Pr_t values are tested to see its influence on the prediction of mass flow rate. These values are 0.9, 1.0, and 1.1. Figure 22 shows the results of different Pr_t at the same inlet condition (7.7 MPa, 498 kg/m^3) for a circular orifice. In Figure 22, different Pr_t numbers give a similar prediction of mass flow rate through the circular orifice. As a result, the assumption of $Pr_t = 1.0$ is used in the rest of this research. The tested circular orifice is described with more detail in Section 5.1.

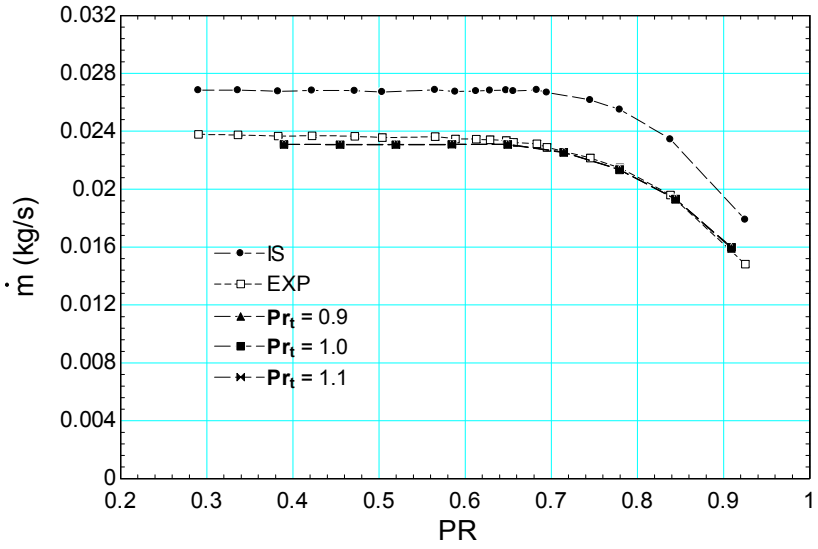

Figure 22 Circular orifice data for different Pr_t using standard k-epsilon model

3.7 Meshing

The meshing is limited to the 2D pseudo-axisymmetric geometry. The circular orifice geometry is discussed as an example; however, the meshing strategy can be applied to other situations if flow condition is similar. As the Reynolds number increases, the recirculation zone at the entrance becomes smaller. The cells in the recirculation region should then also be small to capture this flow structure. Mesh was refined at the entrance. The mesh at the refined zone, with its accompanying velocity vector plot within the recirculation zone, is shown in Figure 23.

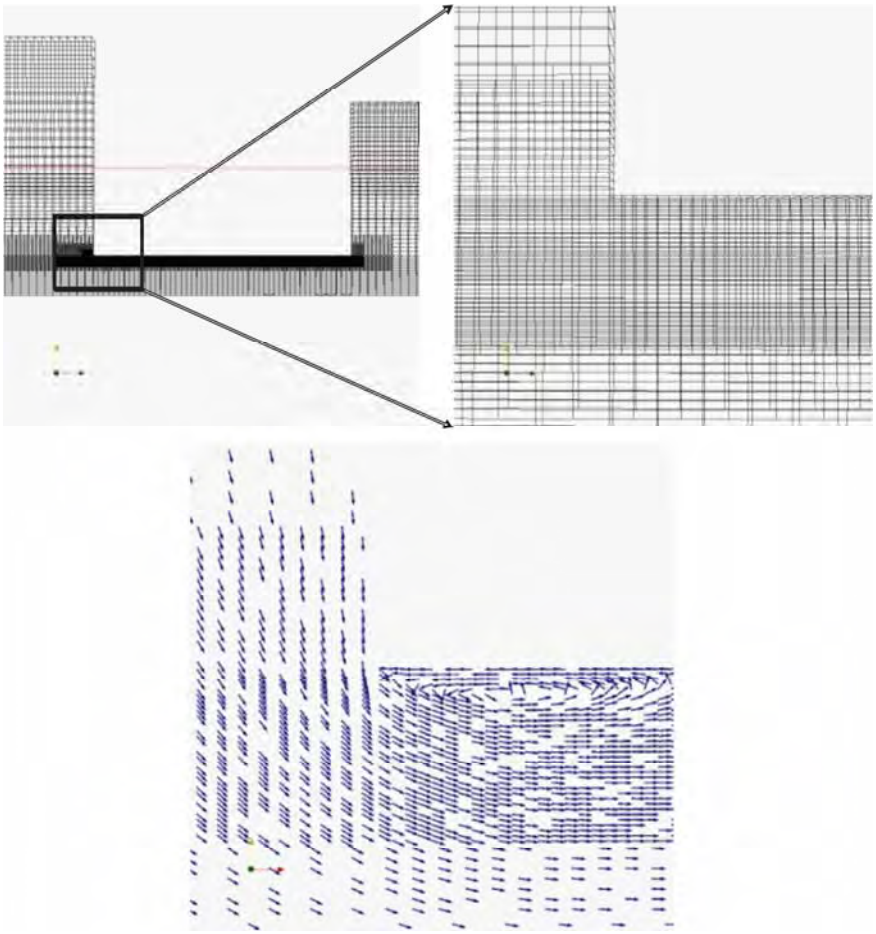

Figure 23 Mesh refinement at entrance

In the standard k-ε model, the wall function requires the boundary cells to be in the log-arithmetic layer. As a consequence, the boundary cells have y+ around 30-50 for all simulated cases.

3.8 Summary

The methodology development in this research is discussed in this chapter. The solver in OpenFOAM was modified to meet the requirements of supercritical and two-phase fluid flow. The FIT code was implemented to provide properties. HEM was applied to model two-phase flow. The pseudo-axisymmetric geometries were used for better computational efficiency. Two different turbulence models were tested using S-CO_2, and the standard k-ε model worked well and gave the best stability and robustness.

4. Experiment facility

This chapter introduces the experiment facility used to provide validation data for S-CO_2 flow. Experimental data for SCW are provided from another experiment facility, which is introduced in Section 2.3.2. The experiment facility for S-CO_2 flow was constructed by Rodarte [66] and improved by Edlebeck and Wolf [67], [68] on the University of Wisconsin-Madison campus. Its system diagram is shown in Figure 24, along with its photograph in Figure 25. The thermodynamic states of each connection are presented on a temperature-entropy diagram of CO_2 in Figure 26. A two-stage compressor (Figure 27) compresses CO_2 to a supercritical state. The outlet of the compressor connects to a large buffer tank to eliminate the pressure fluctuation introduced by the moving of the compressor pistons. After the flow comes out of the compressor, it passes through a precooler/preheater stage. After that, the flow goes through a flow meter (both mass flow rate and density are recorded) and then to the test section. A thermocouple and a pressure transducer are placed before the test section to measure the upstream condition (State 1 in Figure 26). The reservoir tank in the test section helps to maintain a stable downstream condition, corresponding to State 2 in Figure 26. Before the flow returns to the compressor, new CO_2 inventory could be added through the supply tank.

The test section upstream pressure is controlled by changing the power of the compressor along with tuning the valve in the bypass loop. The precooler and preheater control the upstream temperature of the test section. Once the upstream condition reaches its specified value, tuning the valve in the bypass loop or the valve after the test section can modify the mass flow rate through the test section. Detailed diagrams of the test section are presented in Figure 28. The test section is composed of a flange and a reservoir tank. The tested geometry is fixed inside the flange. Figure 28 illustrates a circular orifice for testing; however a subassembly can be implemented to hold a pin inside the circular orifice to form an annular orifice. Using the same method, the labyrinth seal geometry could also be constructed. A different method is used to test a valve, and is discussed in Section 5.3.1.

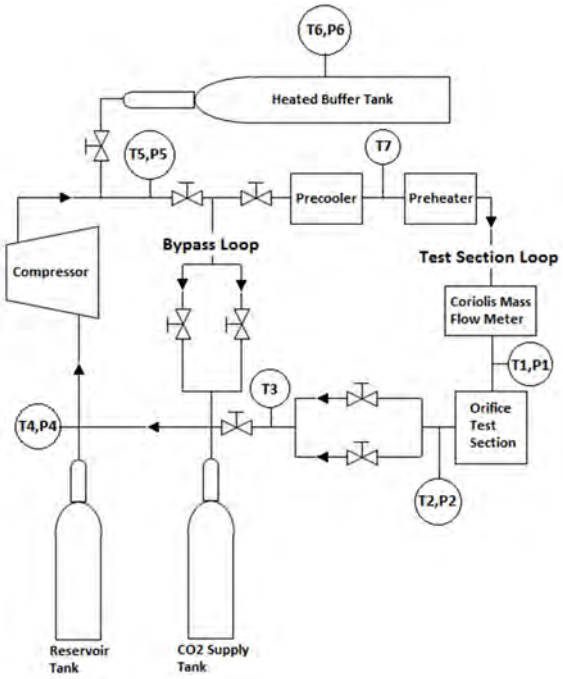

Figure 24 Schematic diagram of experiment facility

Figure 25 Picture of experiment facility

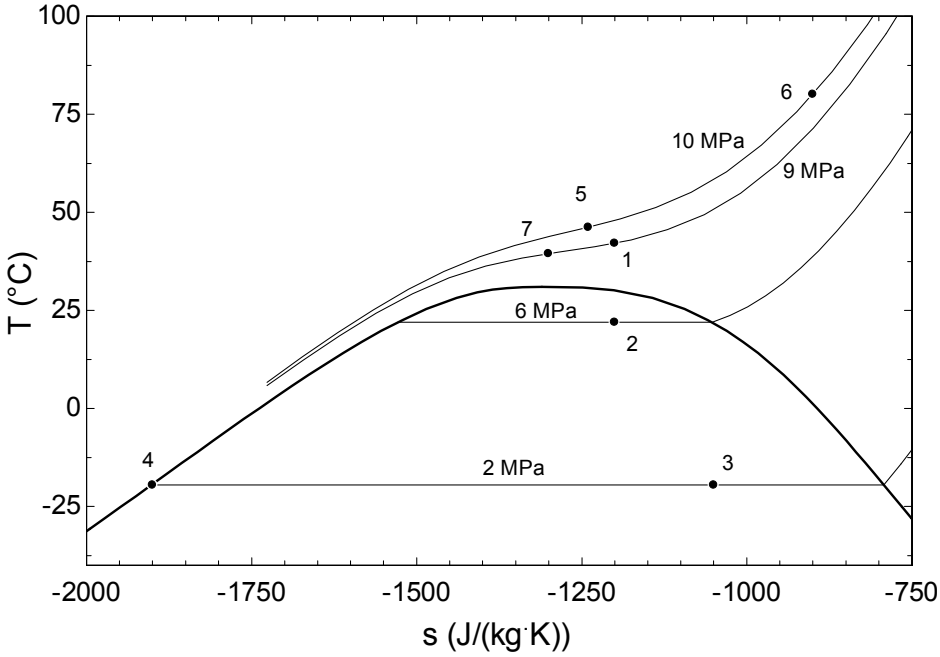

Figure 26 Thermodynamic state of each point in experiment loop

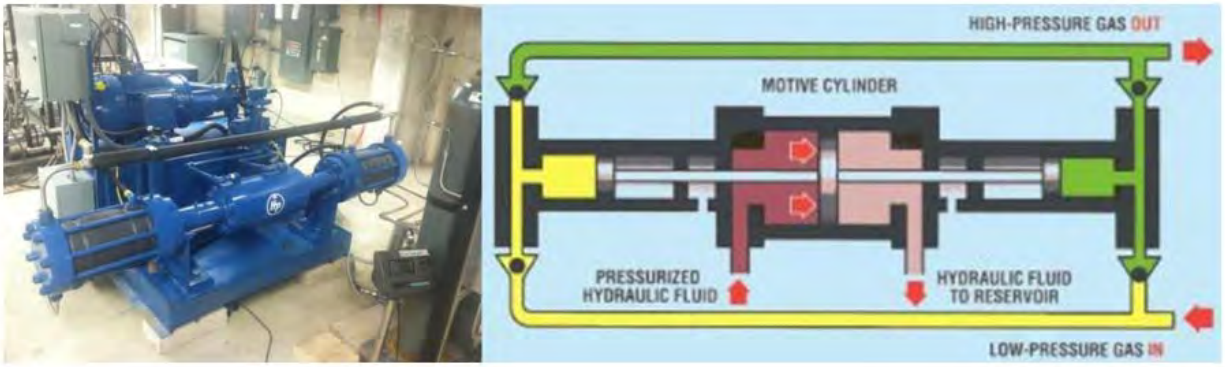

Figure 27 Picture and diagram of Hydro-Pac compressor

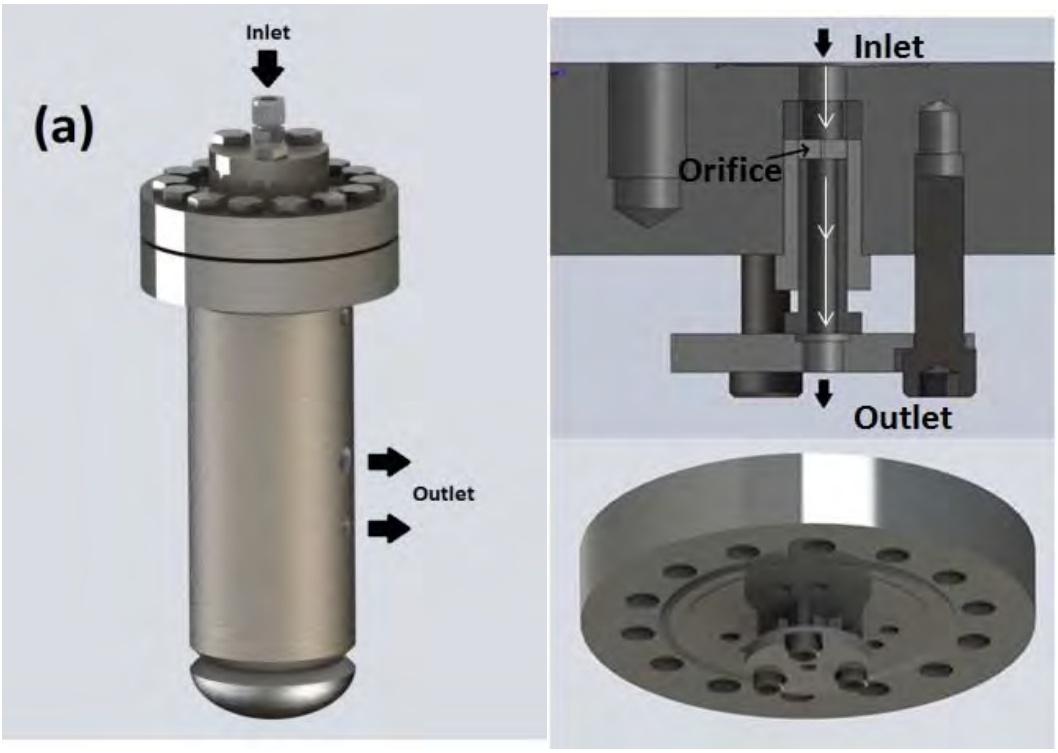

Figure 28 Diagram of test section

The uncertainty analysis was performed by Edlebeck [68], and is only briefly discussed here. Table IV presents instrument, resistance, resolution, and total uncertainties for the measured quantities. These quantities include inlet/outlet pressure, inlet density, and mass flow rate. The uncertainties in Table IV are much smaller than their absolute values. For example, the inlet pressure is usually several MPa with an uncertainty around 20 kPa. The measured mass flow rate is around 0.01 to 0.03 kg/s, and the uncertainty for its measurement is 1.06e-4 kg/s. Therefore, the uncertainty of mass flow rate measurement is less than 1%.

Table IV Measurement uncertainties for experiment facility [68]

Measurement	Instrument	Resistance	Resolution	Total
Inlet pressure	17.24 kPa (2.50 psia)	5.61 kPa (0.814 psia)	1.30 kPa (0.19 psia)	18.18 kPa (2.63 psia)
Outlet pressure	17.24 kPa (2.50 psia)	5.62 kPa (0.816 psia)	1.30 kPa (0.19 psia)	18.18 kPa (2.63 psia)
Inlet density	1.0 kg/m^3	0.325 kg/m^3	0.076 kg/m^3	1.05 kg/m^3
Mass flow rate	1.0e-4 kg/s	3.3e-5 kg/s	7.6e-6 kg/s	1.06e-4 kg/s

5. Validation geometries

This chapter covers the validation of the proposed numerical methodology. As discussed previously, three example geometries were chosen for validation. For orifices, both S-CO_2 and SCW flows were studied. While for labyrinth seals and valves, only S-CO_2 flow was studied. Figure 29 is a part of Figure 2, and shows the flow chart of this chapter.

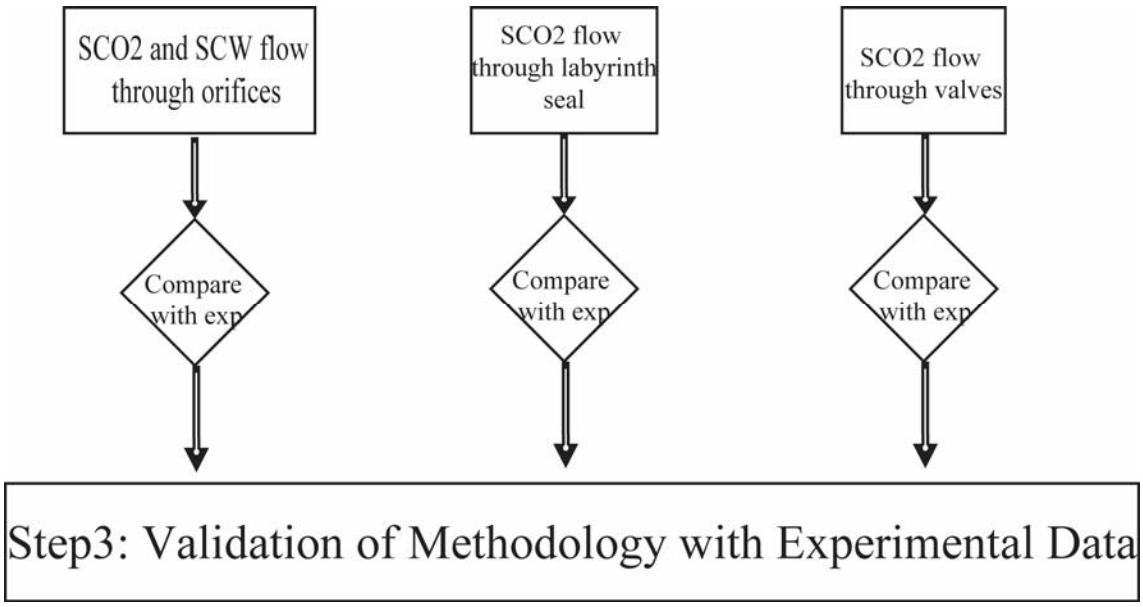

Figure 29 Flow chart for validation

5.1 Geometry 1: Orifices

This section has four subsections. The first subsection shows the geometries of circular and annular orifices in simulations. The second subsection presents the comparison of experimental measurements and simulation data for circular orifices for S-CO_2. The next subsection shows the same comparison but for annular orifices. Then, the work to simulate SCW flow through circular orifice is introduced. This subsection also introduces the experiment facility to measure the SCW choked flow. Finally, a brief summary of this section is presented.

5.1.1 Geometric definition

The geometries for circular and annular orifices are shown in Figure 30. In simulations, a high-pressure condition was applied on the inlet (upper side) and a low-pressure condition was applied on the outlet (bottom side). The computational domains and boundary conditions are elaborated in Figure 18 and Figure 19 in great detail.

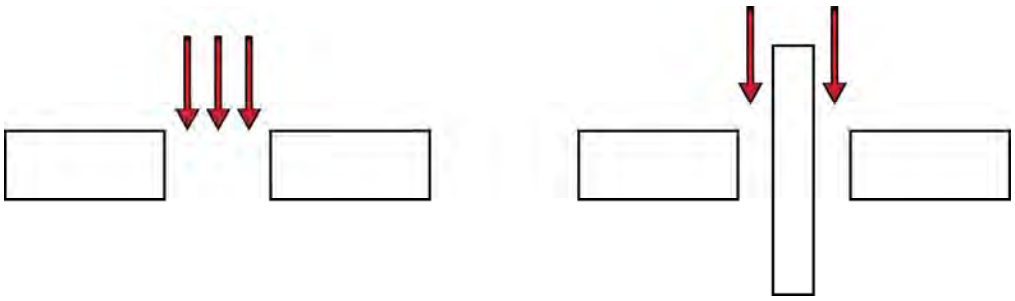

Figure 30 Schematic for the flow through circular and annular orifices

5.1.2 S-CO_2 flow through circular orifice

This subsection summarizes the simulation data for circular orifices. However, only one circular orifice is studied. This circular orifice has a diameter of 1.014 mm, with a length of 3.2 mm. Twelve upstream conditions were tested, and are presented in the Table V. Figure 31 shows the tested upstream conditions from Table V on a temperature-entropy diagram of CO_2. All tested upstream conditions are in the supercritical region. Of the twelve tested upstream conditions, one upstream condition (7.7 MPa at 111 kg/m^3) is far away from the two-phase region while the rest of them are just above it. With the exception of the far removed upstream condition, the flow exhibits flashing when the downstream condition is in the two-phase region.

Table V Inlet conditions for the Circular Orifice test

Pressure (MPa) / Density (kg/m^3)	7.7	9.0	10.0	11.0
111	O	X	X	X
372	O	O	O	O

498	O	O	O	O
630	O	O	O	X

O represents this condition is tested, X represents this condition is not tested.

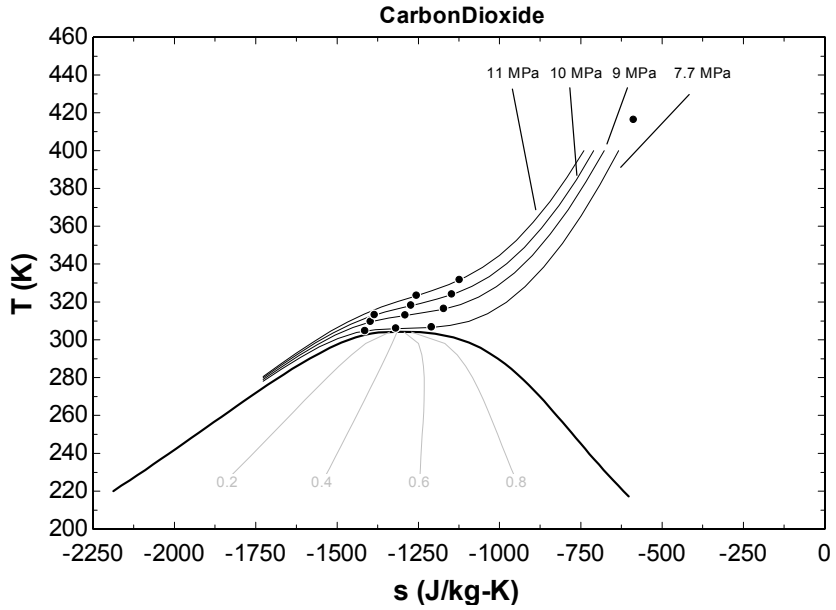

Figure 31 Circular orifice tested inlet conditions on T-S diagram

Figure 32 and Figure 33 show simulation results and comparisons with experimental measurements. Two upstream conditions are demonstrated as examples; data from other tested upstream conditions are presented in Appendix B. The mass flow rate predictions are very close to measurements with a maximum 5% difference. Figure 34 compares predictions and measurements for all tested conditions.

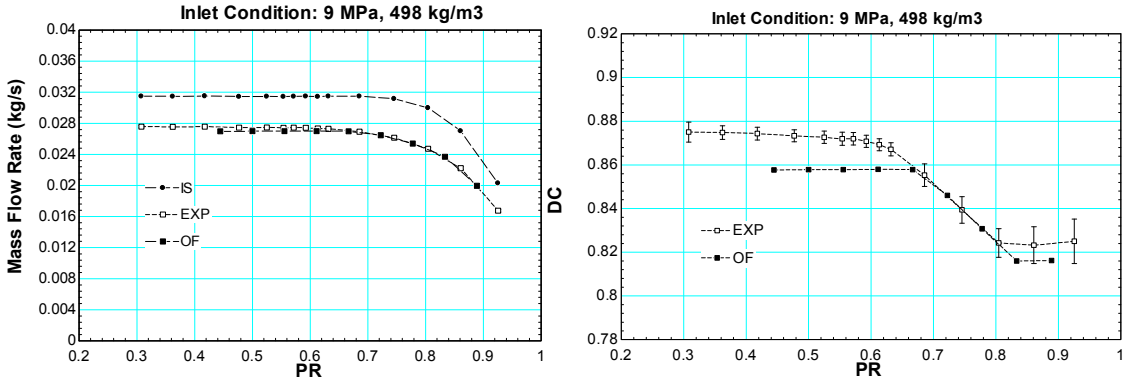

Figure 32 Short circular orifice simulation and experiment data for inlet condition 9 MPa, 498 kg/m^3

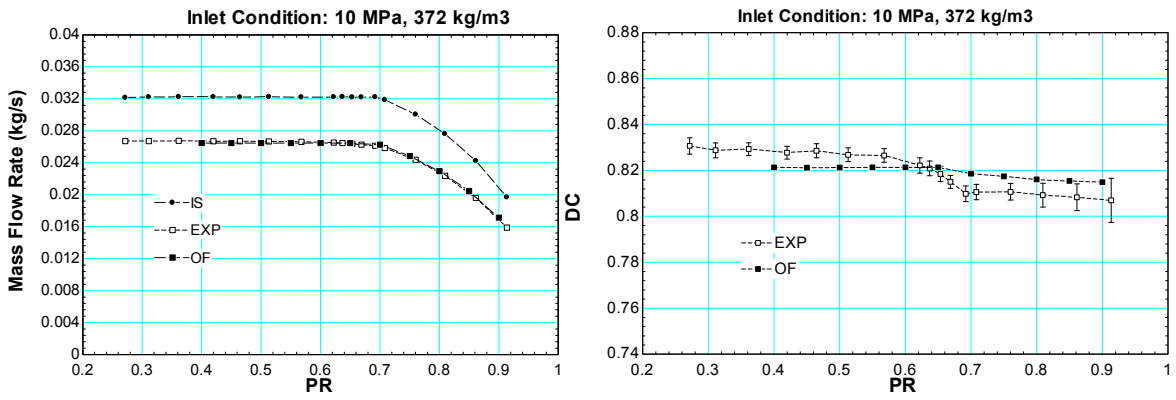

Figure 33 Short circular orifice simulation and experiment data for inlet condition 10 MPa, 372 kg/m^3

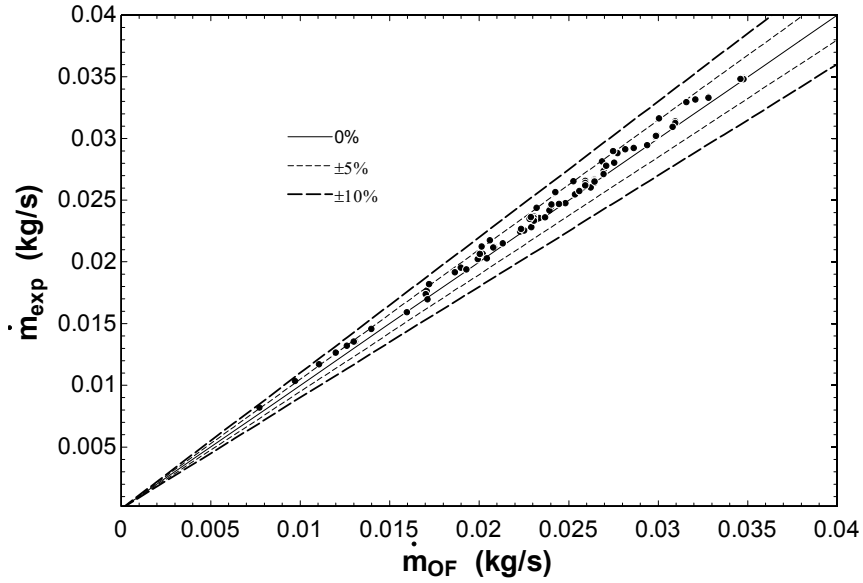

Figure 34 Mass flow rate comparison of the circular orifice

5.1.3 S-CO_2 flow through annular orifice

Simulations and experiments were also performed on three annular orifices. Table VI gives the geometric parameters for these annular orifices. These annular orifices have different length-to-clearance ratios, and are referred to as short, medium, and long annular orifice respectively. The results presented in this document show that as the length increases, the frictional effect becomes more important. The roughness plays an important role for the long annular orifice in Figure 37, but is less significant in the short and medium annular orifices in Figure 35 and Figure 36. The values of the roughness used in simulations are

shown after the OF in the legend of each figure. The best estimated roughness is approximately 0.5 μm. The measured roughness is about 0.46 μm, which is very close to the estimated value. All the data from simulations with roughness of 0.5 μm are compared with experimental measurements in Figure 38. Like the results discussed in the previous subsection, the maximum difference is about 5%. Numerical and experimental data for other tested conditions are presented in Appendix B.

Table VI Geometry parameter for annular orifices

Name	Inner diameter (in)	Outer diameter (in)	Length (in)	Length/Clearance	Test conditions
Short	0.118	0.1267	0.05	11.5	(10MPa, 475kg/m^3)
Medium	0.118	0.1267	0.1	23	(10MPa, 325kg/m^3), (10MPa, 475kg/m^3)
Long	0.118	0.1258	1.23	315	(10MPa, 475kg/m^3), (11MPa, 498kg/m^3)

Clearance = (Outer Diameter-Inner Diameter)/2

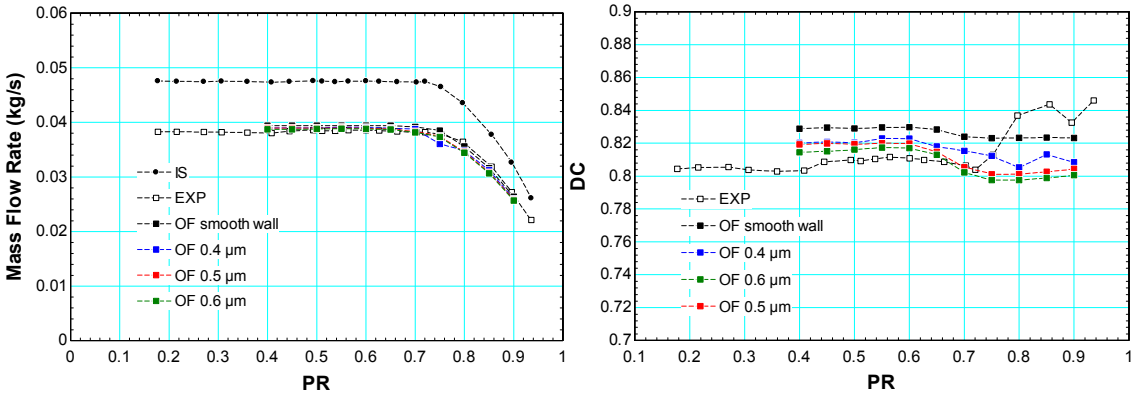

Figure 35 Short annular orifice data for inlet condition 10 MPa, 475 kg/m^3

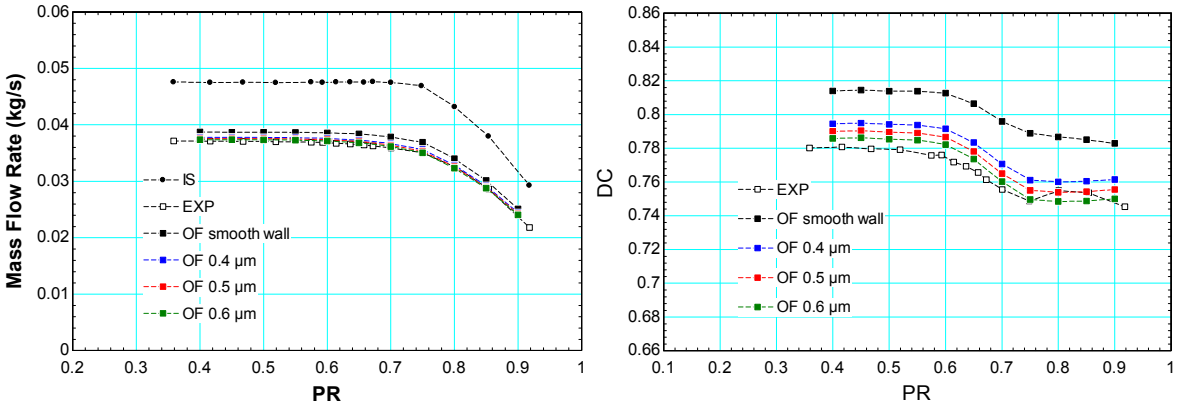

Figure 36 Medium annular orifice data for inlet condition 10 MPa, 475 kg/m^3

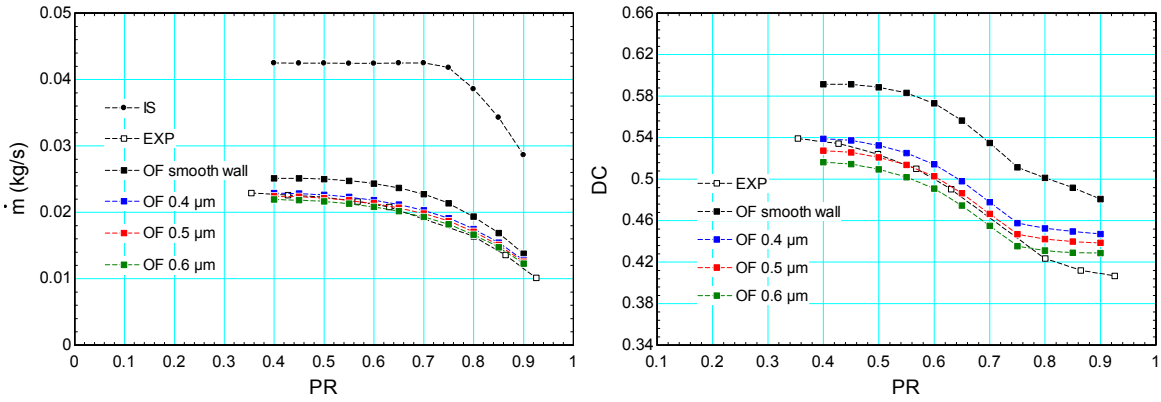

Figure 37 Long annular orifice data for inlet condition 10 MPa, 475 kg/m^3

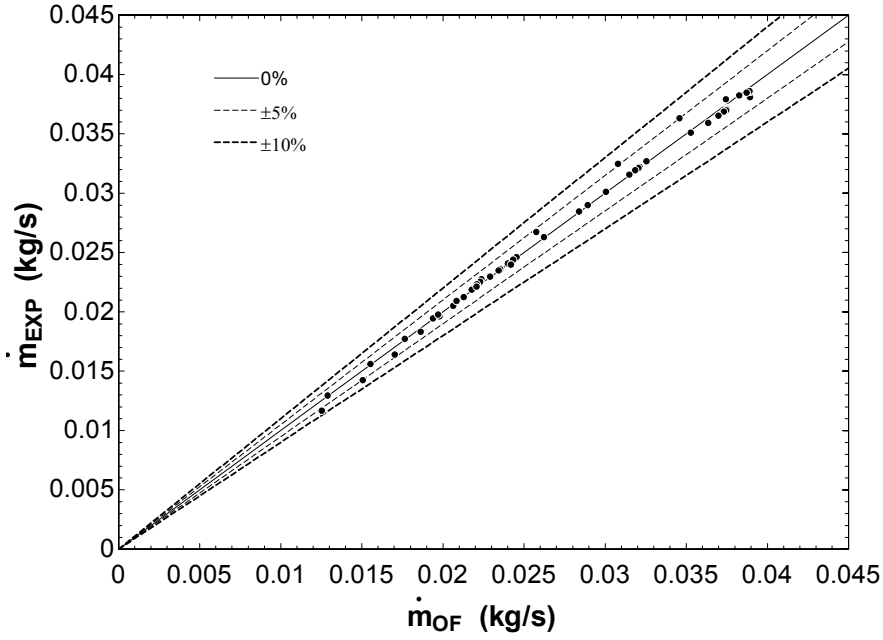

Figure 38 Mass flow rate comparison of annular orifice

5.1.4 SCW flow through circular orifice

In previous subsections, only S-CO_2 is used in simulations. This subsection explores how the developed methodology works for fluids other than S-CO_2, like SCW. The property module of SCW was implemented into OpenFOAM using the same methodology discussed in Chapter 3. The experiment of SCW choked flow was conducted by Chen [20], [32]. The tested orifices shown in Figure 39 are 1.41 mm in diameter and 4.35 mm in length. One orifice has a round entrance, and the other has a sharp entrance. Figure 10 shows the system diagram of the test facility. SCW was supplied by a three-head piston pump with a maximum pressure of 45 MPa and a maximum flow rate of 2.4 m^3/h. Then SCW passed through a dumping tank and a preheater, and flowed upward through the orifice. A thermocouple and a pressure transducer were used to determine upstream conditions, with a flowmeter measuring the flow rate. Only the choked mass flow rate is measured in this experiment, as the downstream pressure is close to the atmospheric pressure.

Figure 40 and Figure 41 show the comparisons of numerical and experimental data for the sharp entrance orifice, as a complete geometry profile is not available for the round entrance orifice. The experimental data

in Figure 40 and Figure 41 perform as lines representing the choked mass flow rate. When comparing the predicted choked flow rate with the experimental data, a difference of 5% is observed. However, readers should keep in mind that the uncertainties of the experiment are not provided.

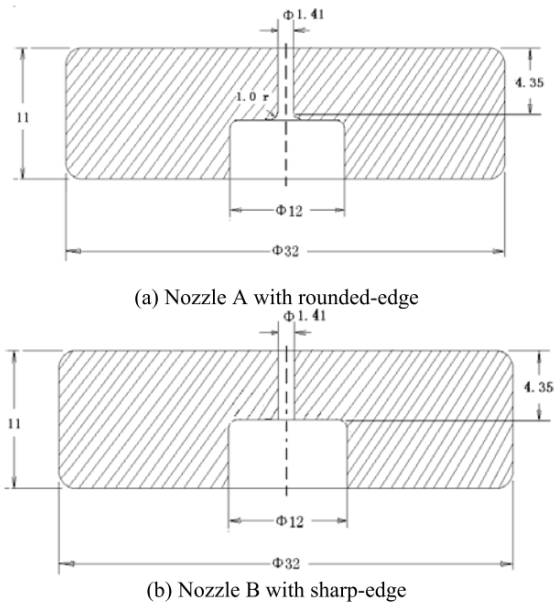

Figure 39 Nozzles tested in SCW choked flow experiment by Chen[20], [32]

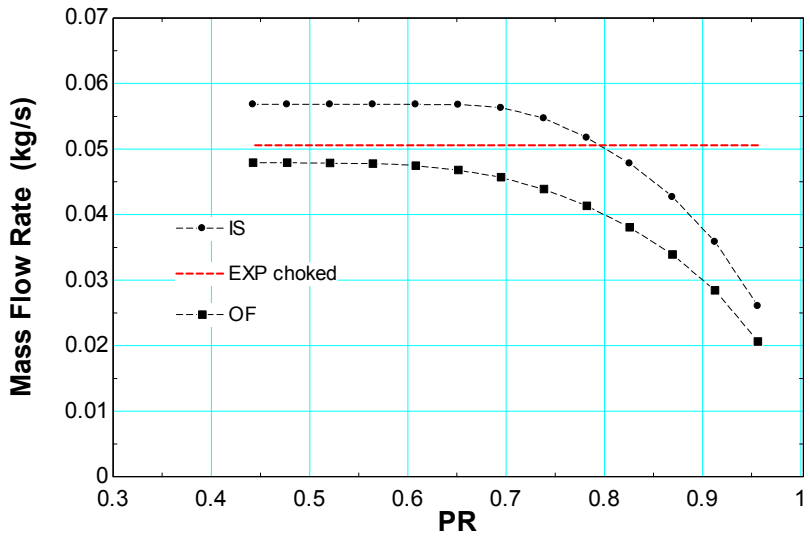

Figure 40 Comparison of simulation and experiment for SCW at 22.95 MPa and 392.5 ^{0}C

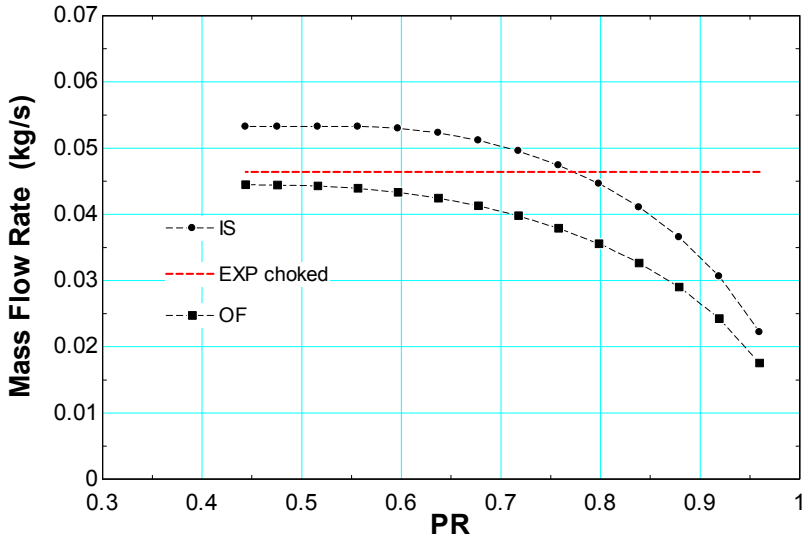

Figure 41 Comparison of simulation and experiment for SCW at 24.8 MPa and 453 ^{0}C

5.1.5 Summary

Section 5.1.2 and 5.1.3 present comparisons of experimental measurements and simulation data for circular and annular orifices for S-CO_2. The maximum difference of mass flow rate between the experiment and simulation is around 5%. SCW property module was also implemented and validated with experimental data. Results from different conditions and supercritical fluids demonstrate the validity and extensibility of the proposed numerical methodology.

5.2 Geometry 2: labyrinth seals

The labyrinth seal geometry was studied as another example. This section has eight subsections. The first subsection gives a geometric definition of labyrinth seals. Then, available experimental data are used to validate the proposed numerical methodology. After that, consecutive subsections present the parametric study on the leakage rate. Four parameters were inspected; they are radial clearance, cavity length, cavity height, and tooth number. Before the final subsection, a stepped labyrinth seal, which mimics the seal in SNL S-CO_2 Brayton cycle compressor, was studied. The final subsection makes a summary and proposes an optimization method for labyrinth seals under S-CO_2 condition.

5.2.1 Geometric definition

Figure 42 shows the schematic diagram of a two-tooth labyrinth seal. The S-CO_2 enters the seal from the left and leaks out to the right. The geometric definitions shown in Figure 42 are used in the rest of this section. Table VII defines the geometric notations in Figure 42. The goal is to investigate how each geometric parameter affects the mass flow rate through labyrinth seals. Once this is understood, an optimization method can be developed to design a labyrinth seal for turbomachinery using supercritical fluid. Table VII defines seven variables with one inherent relationship between them: $L_{total} = n\ L_{tooth} + (n-1)\ L_{cavity}$, leading to six independent variables. In this research, four geometric parameters were chosen for parametric study. They are radial clearance, cavity length, cavity height, and tooth number. The total length was excluded, as it is limited by the available space in the turbomachinery. And the tooth width was also excluded as it changes according to the change of total length and cavity length. The shaft diameter was fixed for experiment and simulation convenience.

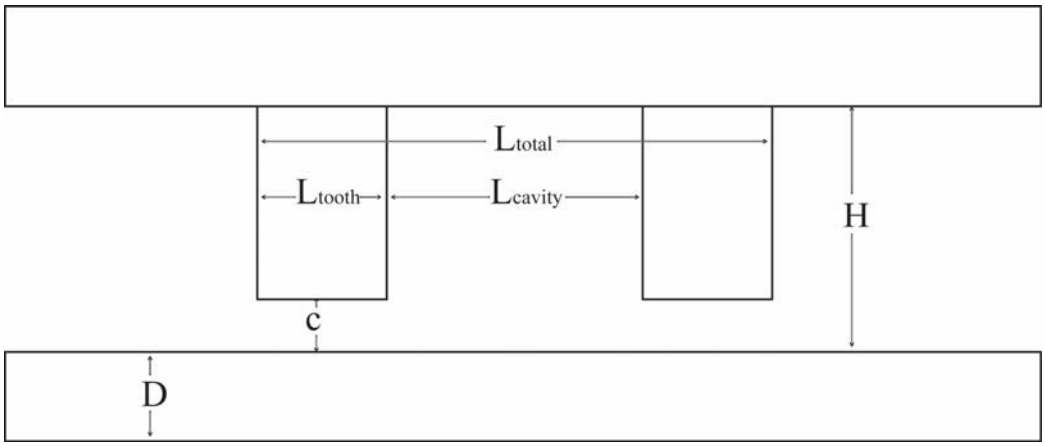

Figure 42 Schematic of two-tooth labyrinth seal (not to scale)

Table VII Notations for labyrinth seals

Description	Notation
Shaft Diameter	D
Radial Clearance	c
Cavity Height	H
Cavity Length	L_{cavity}
Tooth Width	L_{tooth}
Total Length	L_{total}
Tooth number	n

5.2.2 Validation with experimental data

Experiment of a two-tooth labyrinth seal was conducted first to validate the developed methodology. Table VIII gives a geometric description of the tested labyrinth seal. Two inlet conditions were tested in the experiment, they are (10 MPa, 325 kg/m^3) and (10 MPa, 475 kg/m^3). Figure 43 and Figure 44 present the comparison of experimental measurements and numerical data for the tested conditions. Similar to last section, leakage rate predictions are close to experimental measurements. Therefore, it is feasible to use the developed numerical methodology to predict labyrinth seal leakage rates.

Table VIII Geometry parameter for two-tooth labyrinth seal in experiment

Description	Notation	Number
Shaft diameter	D	3 mm
Seal diameter	D_o	3.21 mm
Radial clearance	c	0.105 mm
Cavity height	H	0.88 mm
Cavity length	L_{cavity}	1.27 mm
Tooth width	L_{tooth}	1.27 mm
Total length	L_{total}	3.81 mm
Tooth number	n	2

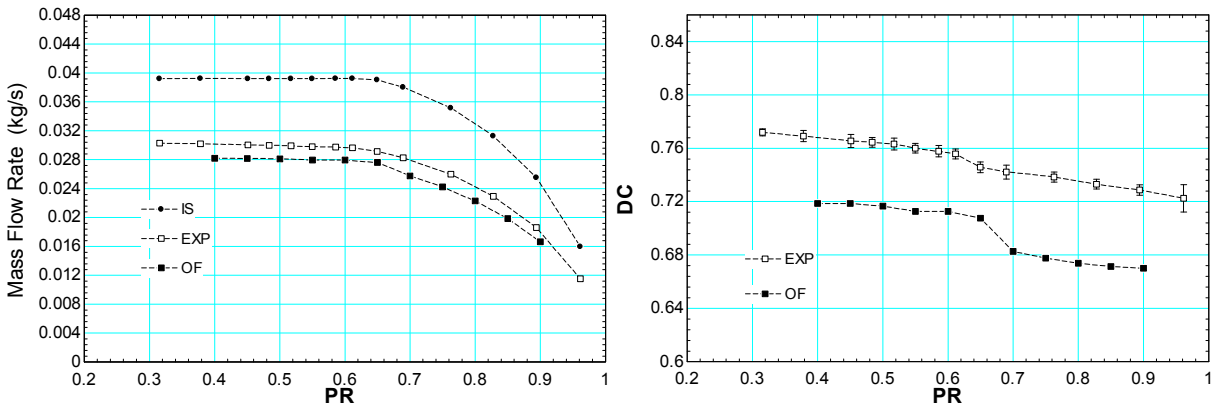

Figure 43 Two-tooth labyrinth seal experiment and simulation comparison (10 MPa, 325 kg/m^3)

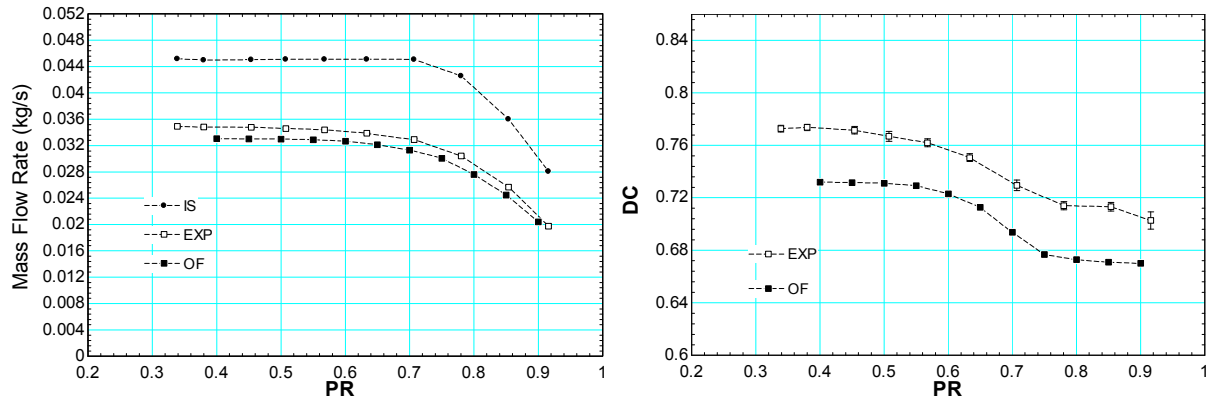

Figure 44 Two-tooth labyrinth seal experiment and simulation comparison (10 MPa, 475 kg/m^3)

5.2.3 Radial clearance

A three-tooth labyrinth seal was used to investigate the effect of radial clearance. Its geometric parameters are presented in Table IX. In Figure 45, the leakage rate increases with the increase of radial clearance. This is a fairly obvious result as an increase in the clearance area allows more fluid to be forced underneath the tooth. It should be noted that the inlet condition is fixed at 10 MPa and 498 kg/m^3. The outlet pressure is 5 MPa for all the cases. Although the results presented here are for a three-tooth labyrinth seal, conclusions are valid for any number of teeth and different operating conditions as well.

Table IX Geometry parameter for three-tooth labyrinth seal for radial clearance parametric study

Description	Notation	Number
Shaft diameter	D	3 mm
Cavity height	H	0.79 mm
Cavity length	L_{cavity}	1.27 mm
Tooth width	L_{tooth}	0.424 mm
Total length	L_{total}	3.81 mm
Tooth number	n	3

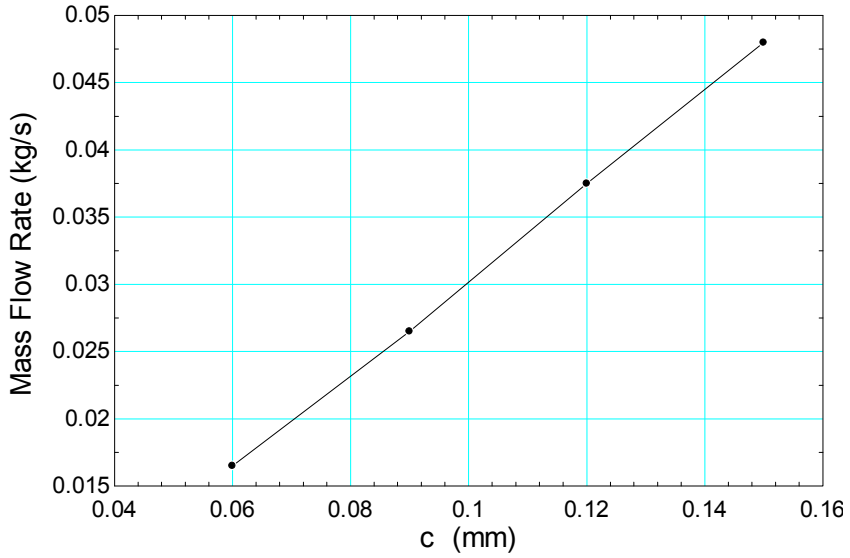

Figure 45 Effect of radial clearance on mass flow rate

5.2.4 Cavity length

A two-tooth labyrinth seal was inspected to see the cavity length's effect on leakage rate. This two-tooth labyrinth seal is identical with the labyrinth seal tested in Section 5.2.2, with a slightly different clearance of 0.09 mm as shown in Table X. The cavity length was changed to investigate the response of the leakage rate. However the total length was kept constant. In Figure 46, the cavity height is fixed to be 0.88 mm, while the cavity length is sampled evenly between 1.27 to 3 mm. All data points in Figure 46 have the same inlet condition of (9 MPa, 498 kg/m^3), and the same outlet pressure of 5 MPa. Figure 46 describes that the

leakage rate decreases as the cavity length increase. This means that the form pressure loss introduced by the cavity is more significant than the friction pressure loss induced by teeth. A three-tooth labyrinth seal was also tested for this parametric study with the same conclusion obtained, and its data can be found in Appendix D.

Table X Geometry parameter for two-tooth labyrinth seal in simulation

Description	Notation	Number
Shaft Diameter	D	3 mm
Seal diameter	D_o	3.18 mm
Radial clearance	c	0.09 mm
Cavity height	H	0.88 mm
Tooth width	L_{tooth}	1.27 mm
Total length	L_{total}	3.81 mm

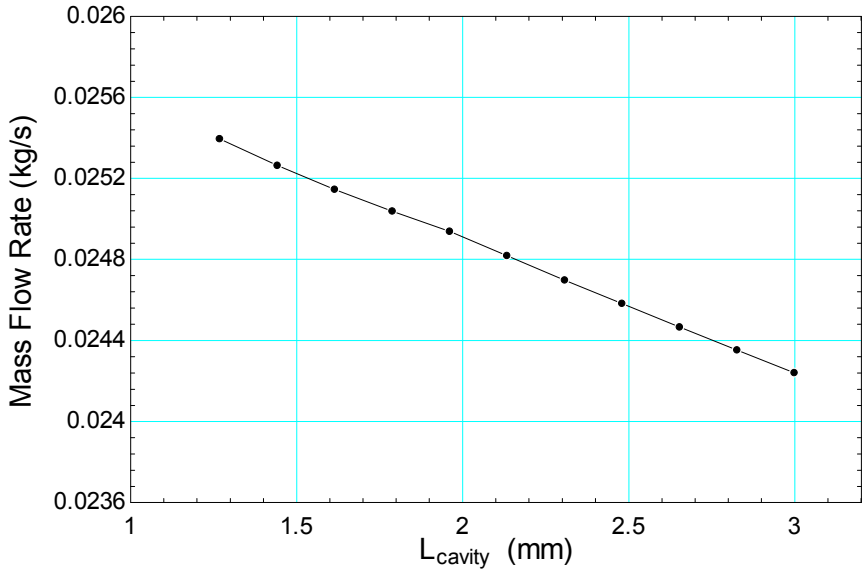

Figure 46 Mass flow rate changes with cavity length at cavity height of 0.88 mm

The streamline plots of two two-tooth labyrinth seals with the same cavity height but different cavity lengths are presented in Figure 47 and Figure 48. In Figure 47, the cavity length is 1.27 mm, while in Figure 48 the

cavity length is 3 mm. In Figure 47 and Figure 48, the main stream spreads a small angle (called expansion angle) after it enters the cavity, and then contracts again when it meets the next tooth producing a contraction pressure loss. At the same time, it interacts with the eddy inside the cavity, and loses its partial kinetic energy. This contraction pressure loss is proportional to the mainstream area change and contributes as the major part of the total pressure loss. The expansion angle was assumed to be constant in Hodkinson [38]'s research. However, Suryanarayanan [43] disagrees with this assumption. Regardless of the expansion angle assumption, the mainstream area change in Figure 48 is much larger than that in Figure 47. In other words, a larger cavity length results in a larger contraction pressure loss and a smaller leakage.

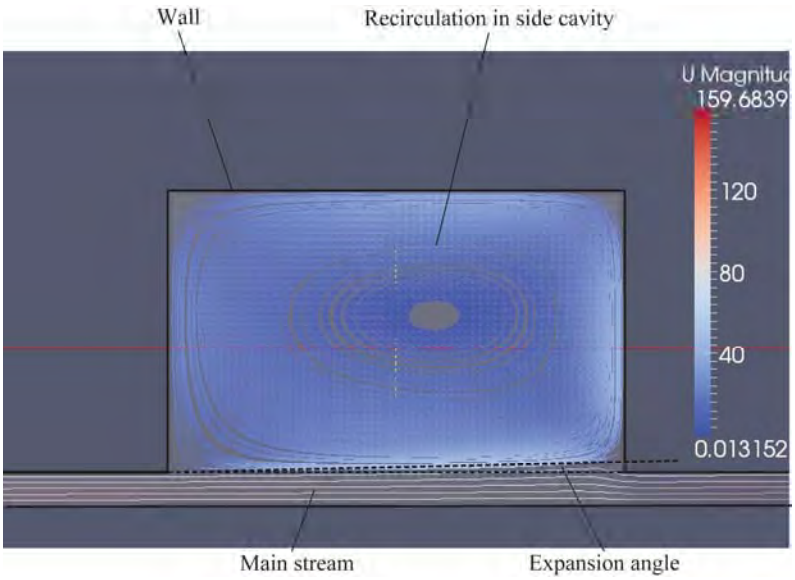

Figure 47 Flow pattern in cavity of labyrinth seal of cavity height of 0.88 mm and cavity length of 1.27 mm

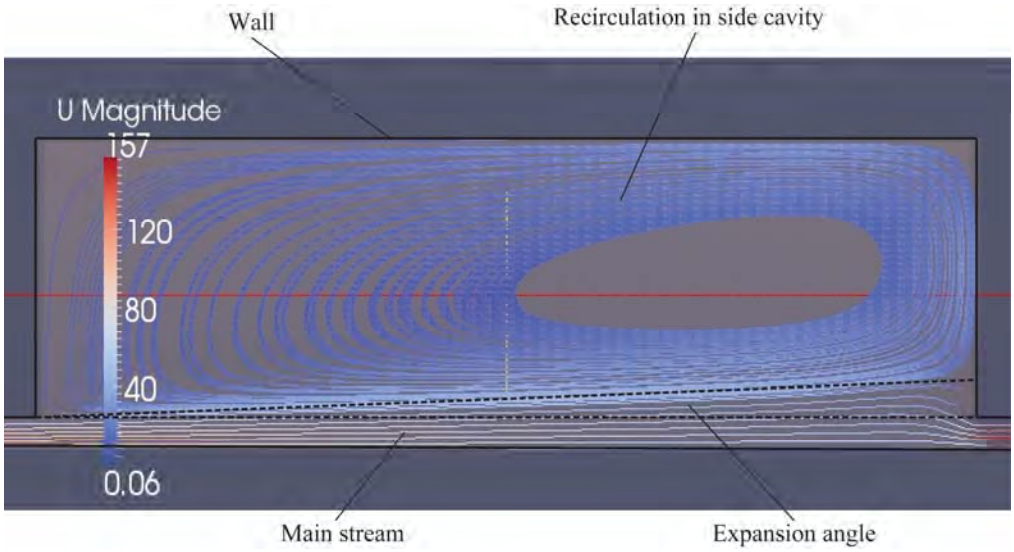

Figure 48 Flow pattern in cavity of labyrinth seal of cavity height of 0.88 mm and cavity length of 3 mm

5.2.5 Cavity height

To inspect the cavity height's effect, the cavity length is fixed and the cavity height is varied. Other geometric parameters are the same as those in Table X. The data in Figure 49 and Figure 50 are based on the same two-tooth labyrinth seal in the last subsection. All the data points have the same inlet condition of (9 MPa, 498 kg/m^3), and the same outlet pressure of 5 MPa. In Figure 49, the cavity length is fixed at 1.27 mm, while the cavity height is sampled evenly between 0.15 and 0.8 mm. In Figure 50, the cavity length is fixed at 3 mm, while the cavity height is sampled evenly between 0.2 and 1.0 mm. Figure 49 and Figure 50 both conclude that there is an optimum point for the cavity height that produces a minimum leakage rate. The same three-tooth labyrinth seal in last subsection was also tested for this parametric study with the same conclusion obtained, and its data can be found in Appendix D.

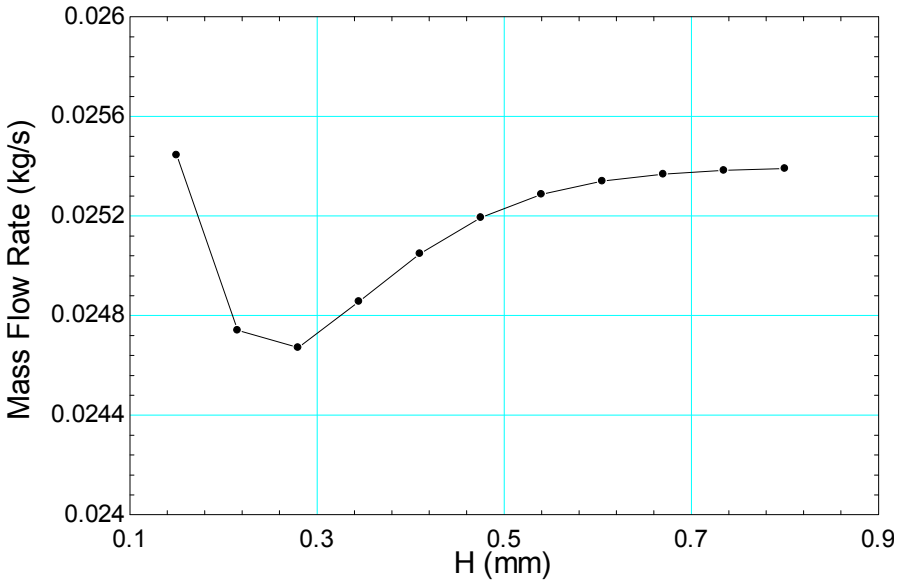

Figure 49 Mass flow rate changes with cavity height at cavity length of 1.27 mm

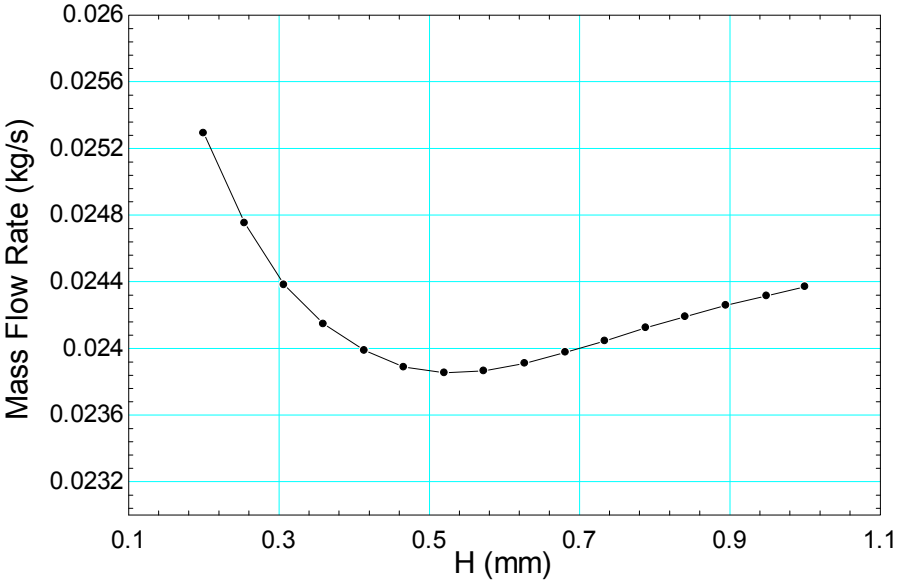

Figure 50 Mass flow rate changes with cavity height at cavity length of 3 mm

The phenomenon in Figure 49 and Figure 50 was also found in the experiment of Eldin [39]. He used three five-tooth labyrinth seals with the same cavity length but different cavity heights. In Figure 51, the leakage from two labyrinth seals with cavity heights of 20 mils (0.508mm, blue) and 50 mils (1.27mm, green) are

compared with a labyrinth seal with a cavity height of 500 mils (12.7mm). In Figure 51, the labyrinth seal with 50-mil cavity height has a less leakage, while the 20-mil cavity height labyrinth seal has a higher leakage. Readers should notice that the y axial in Figure 51 represents the drop in leakage; as a result, a positive value means a decreased leakage.

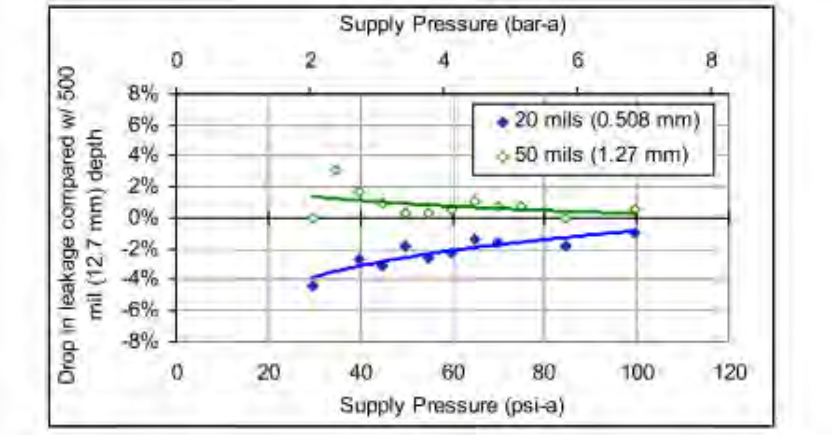

Figure 51 Labyrinth seal cavity height study by Eldin [39]

The following three figures show the flow pattern in three two-tooth labyrinth seals that share the same cavity length of 3 mm but different cavity heights. Their mass flow rates are presented Figure 50. The labyrinth seal in Figure 52 has the largest cavity height, while that in Figure 54 has the smallest cavity height. In Figure 54, the cavity height is too small that limits the mainstream expansion, while in Figure 52 the mainstream expansion is fully developed. An interesting phenomenon is observed in Figure 53, that the mainstream expansion is the largest. The possible reason is that the eddy in Figure 53 is not fully developed, and then does not limit the mainstream expansion. As a result, the contraction pressure loss in Figure 53 is the largest, leads to the minimum leakage in Figure 50.

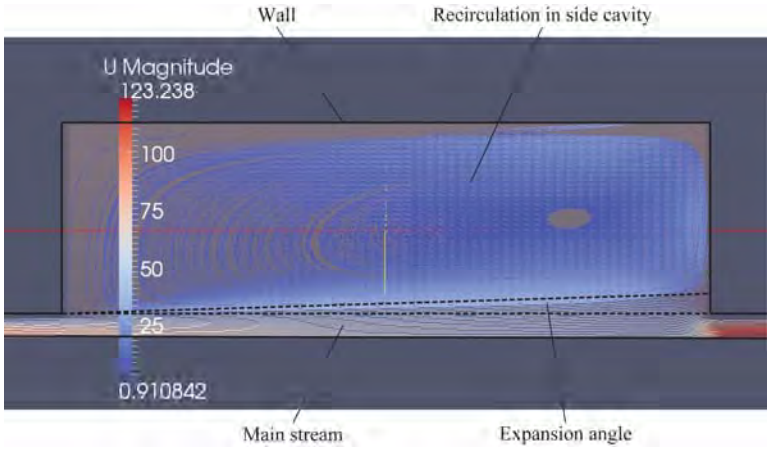

Figure 52 Flow pattern in cavity of labyrinth seal of cavity height of 1 mm and cavity length of 3 mm

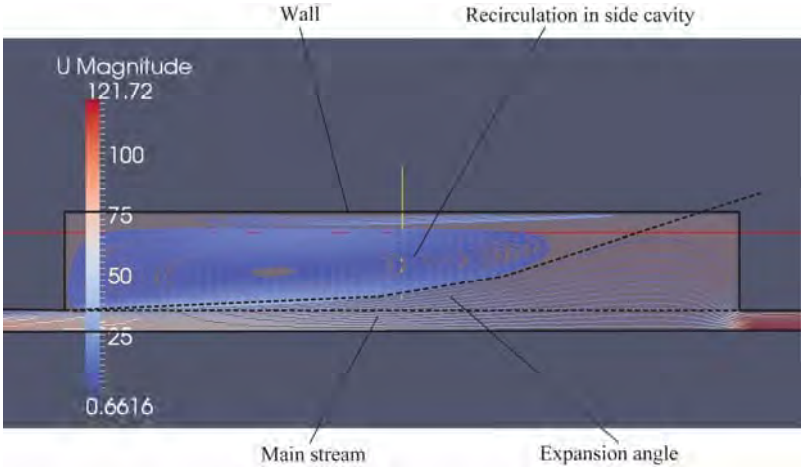

Figure 53 Flow pattern in cavity of labyrinth seal of cavity height of 0.52 mm and cavity length of 3 mm

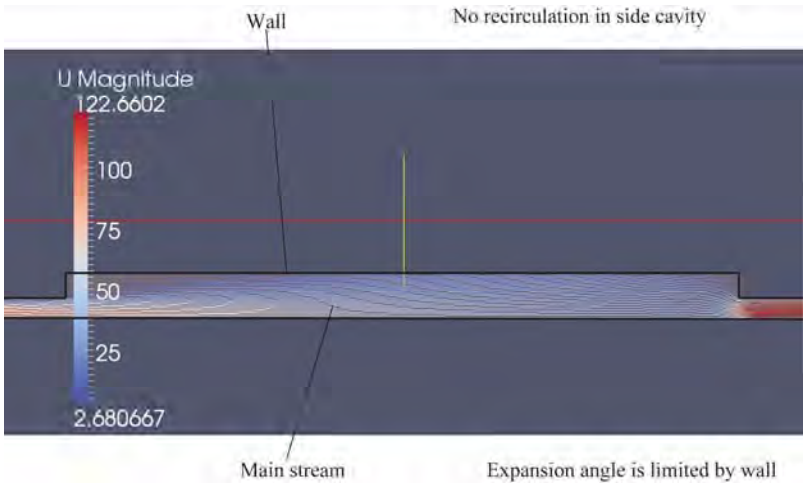

Figure 54 Flow pattern in cavity of labyrinth seal of cavity height of 0.2 mm and cavity length of 3 mm

5.2.6 Tooth number

In this subsection, the tooth number is varied. In order to compare designs with different toot numbers, the total length is fixed. The tooth width is also fixed assuming this is the manufacture's limit, and each tooth is assumed to be identical. Figure 55 shows labyrinth seals of different tooth numbers. By inserting more teeth into the seal, the leakage rate initially decreases. However, after a certain number of teeth are inserted, the leakage rate increases. There is a tooth number with a minimum leakage rate. This subsection wants to shows the existence of this optimum tooth number. Total lengths of all designs are fixed to 11.43 mm (0.45 in); with tooth widths are 1.27 mm (0.05 in). The upstream condition is (10 MPa, 498 kg/m^3). Figure 56 displays the data of these labyrinth seals at different pressure ratios, with Figure 57 shows the data at a pressure ratio of 0.5. In Figure 57, the seal design with three teeth has the minimum leakage rate. From previous discussion, increasing cavity length reduces leakage. In this section, as teeth are inserted into the seal, cavity length decreases for a fixed total length. As a result, at a certain point, inserting more teeth cannot bring more benefits to decreasing leakage, as cavity length is too small.

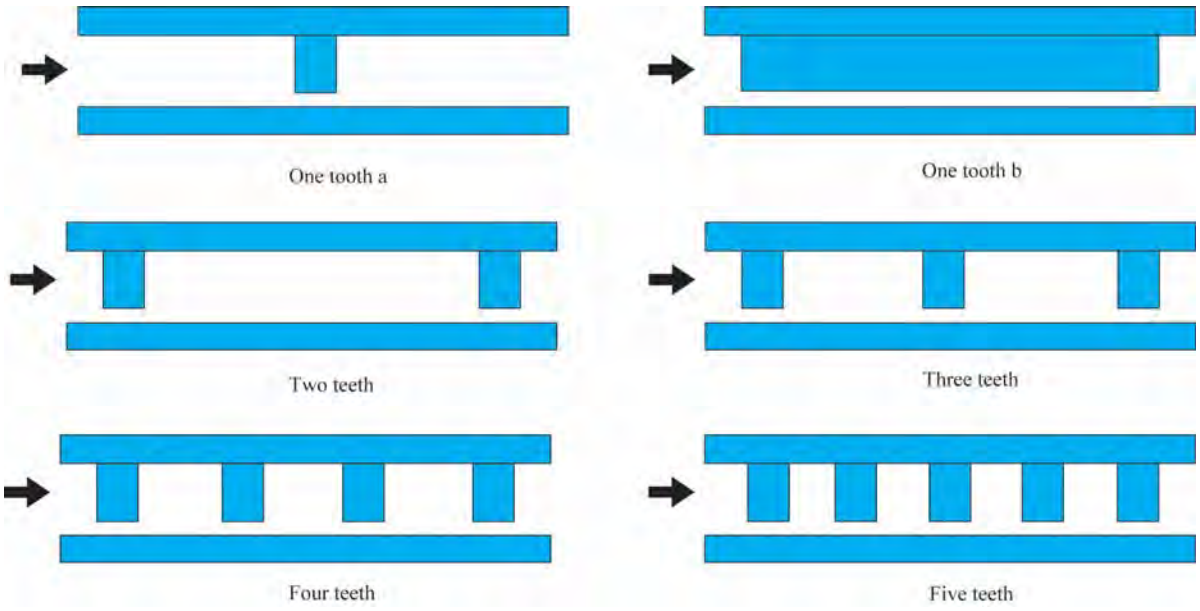

Figure 55 Labyrinth seal designs of same total length

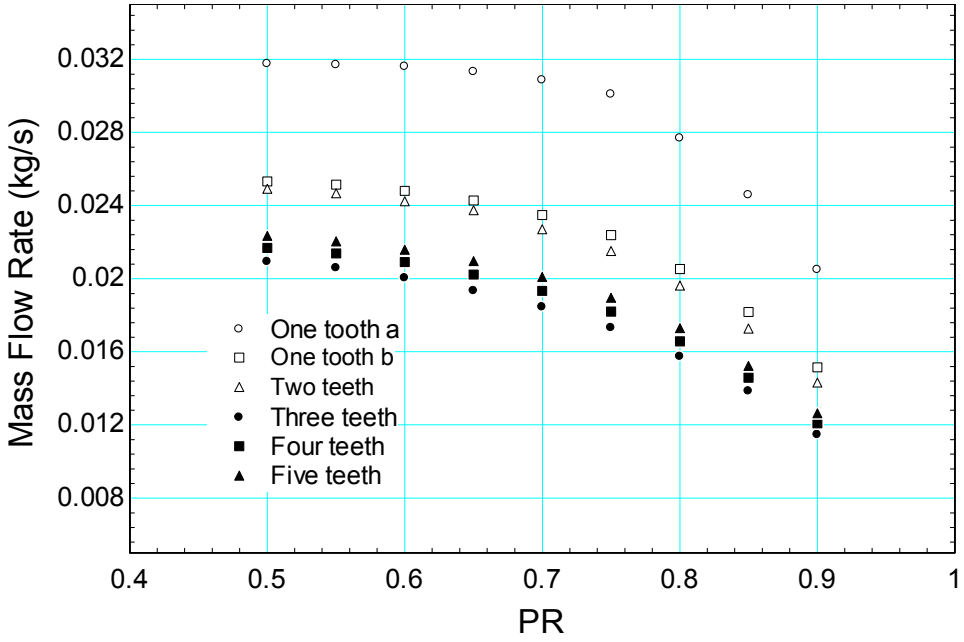

Figure 56 Mass flow rates of different tooth number labyrinth seals

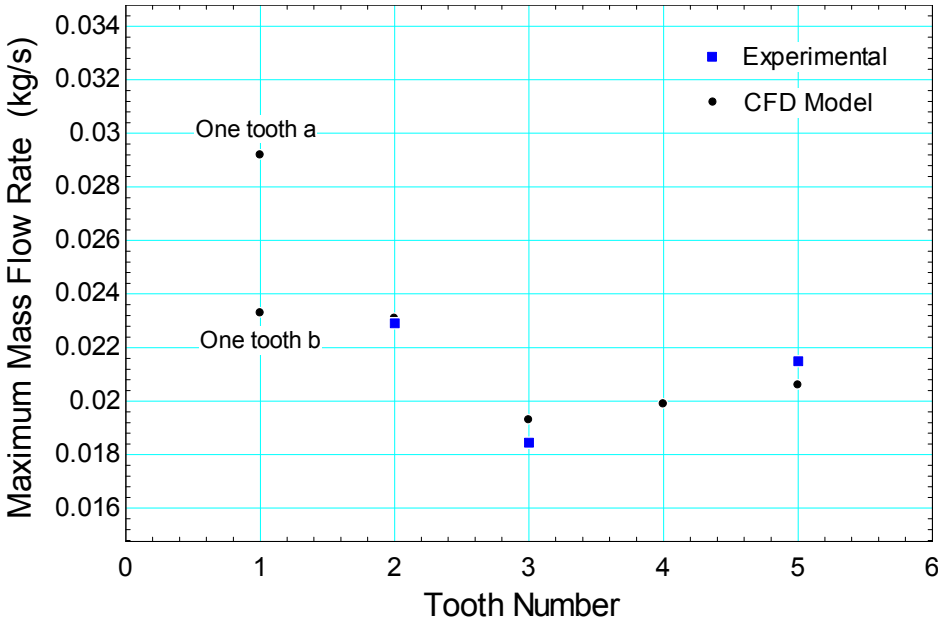

Figure 57 Maximum mass flow rate VS tooth number

5.2.7 Simulation of SNL labyrinth seal design

A labyrinth seal is used in the SNL S-CO_2 Brayton Cycle Compressor [15] as shown in Figure 11. The leakage through this labyrinth seal was measured while shaft is rotating as shown in Figure 58. This measurement was compared with the Martin model (Equation 52). S_o is the flow area, C_d is the discharge coefficient which is assumed to be 0.61, and N is the number of teeth. And p_1 is the upstream pressure, p_2 is the downstream pressure, ρ_1 is the upstream density.

$$\dot{m} = C_d S_o \sqrt{p_1 \rho_1 \left(\frac{\left(1 - p_2/p_1\right)}{N - \ln\left(p_2/p_1\right)} \right)} \qquad 52$$

Several conclusions can be reached in Figure 58. First, the seal leakage is independent of the shaft rotation speed. Second, the Martin model under predicts about 30%, indicating the limitation of existing models. The oscillation of the measured leakage rate is due to the two-phase appearance at downstream.

This labyrinth seal is actually a stepped labyrinth seal. However, due to the limitation of our test facility, it is currently not feasible to test the same design. Therefore, a similar design with different dimensions is tested, and its shaft and seal designs are presented in Figure 59. Two different shafts are manufactured, one with two steps, and the other with three steps. Using the shaft with two steps forms a three-tooth labyrinth seal, while using another forms a four-tooth labyrinth seal. However, the steps on shaft are not perfect, and curves are observed as shown in Figure 60. More details of the profile on shaft are given in Appendix D. This geometric profile is implemented into simulation.

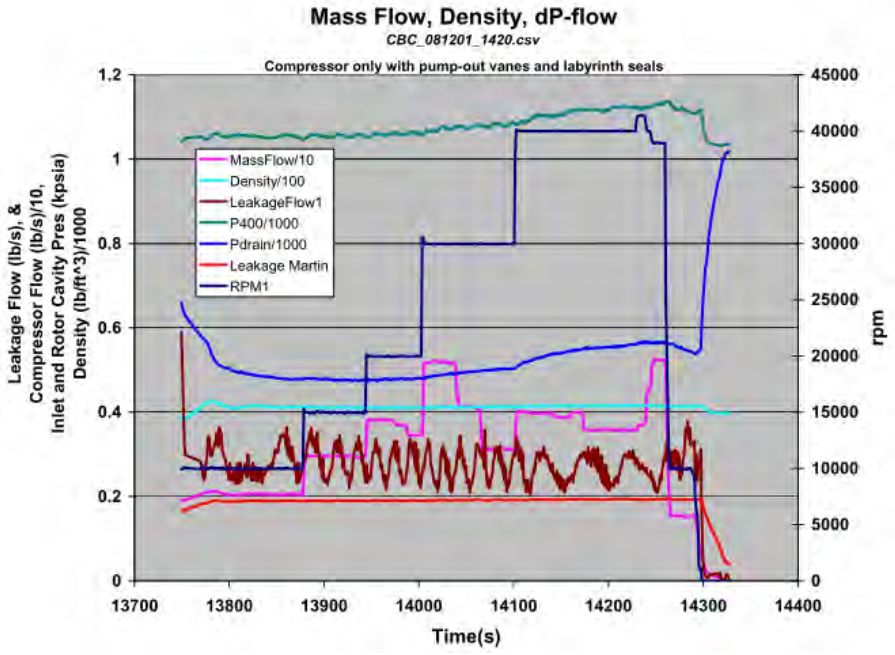

Figure 58 Measured (brown) and predicted (red) leakage flow rate through labyrinth seal

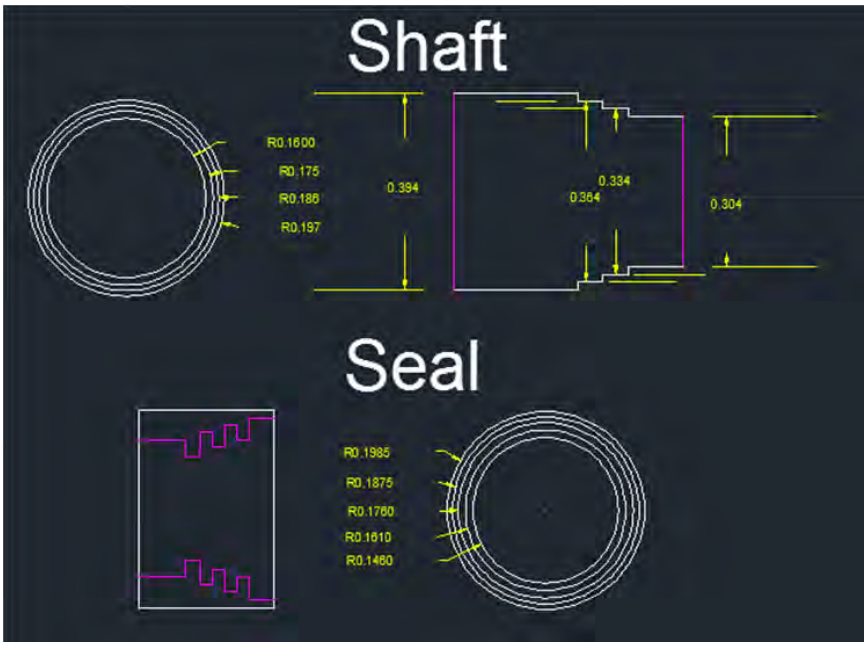

Figure 59 Dimension of tested stepped labyrinth seal

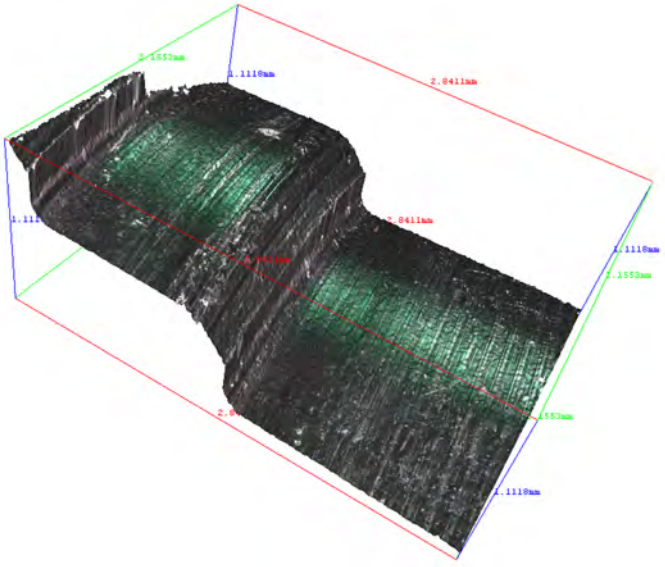

Figure 60 Curves on shaft steps

In the rest of this part, the experimental and numerical data are compared for the three-tooth stepped labyrinth seal. Two upstream conditions (7.7 MPa at 498 kg/m^3, and 10 MPa at 640 kg/m^3) are tested. The predicted data and experimental data are compared in Figure 61 and Figure 62. As can be seen, the proposed numerical methodology matches the experimental data very well.

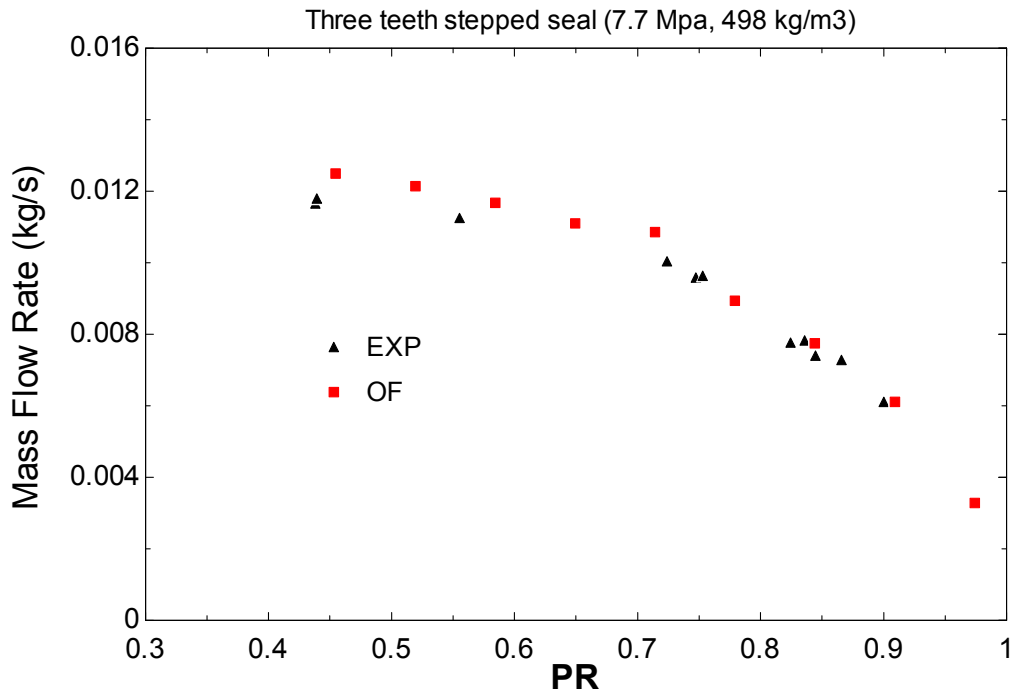

Figure 61 Mass flow rates for three-tooth stepped labyrinth seal for 7.7 MPa at 498 kg/m^3

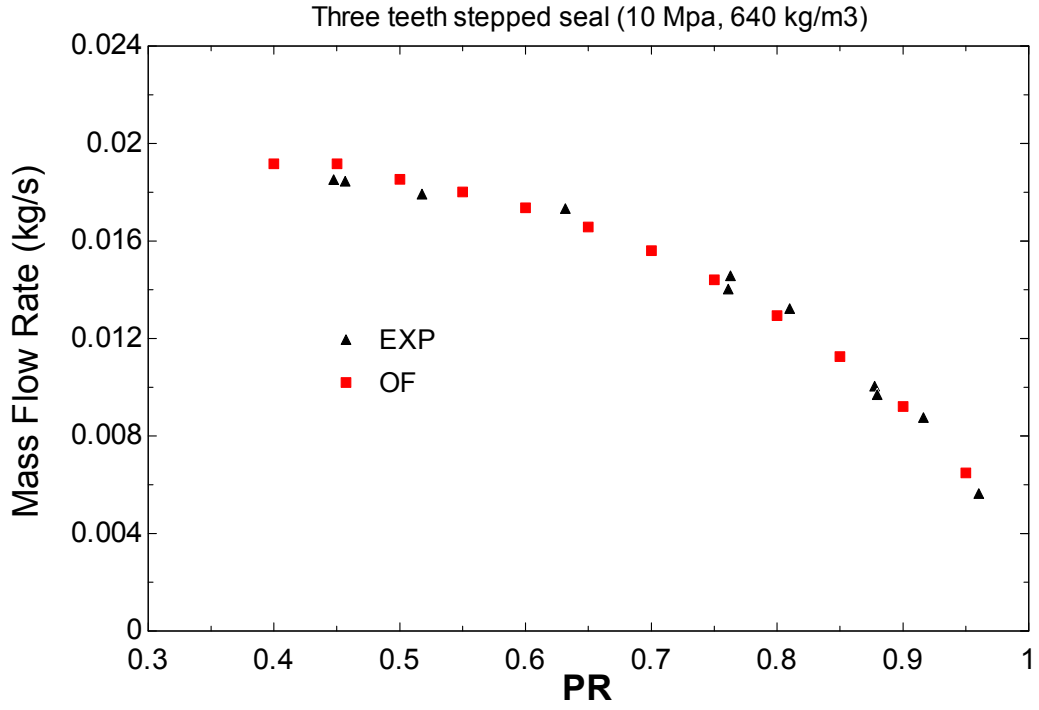

Figure 62 Mass flow rates for three-tooth stepped labyrinth seal for 10 MPa at 640 kg/m^3

5.2.8 Summary

In this section, a geometric description of labyrinth seals is first presented. Then, comparisons show experimental data and simulation results are in agreement. After that, four geometry parameters, radial clearance, cavity length, cavity height, and number of teeth, were studied to understand their effects on the leakage rate. First, increasing the radial clearance increases the leakage rate. As the radial clearance gets larger, more flow area is provided. Therefore, the radial clearance should be minimized to reduce leakage. Second, increasing the cavity length decreases the leakage rate. This is because an increased cavity length leads to a more developed mainstream expansion. As a result, the mainstream area change before the next tooth is larger, and results an increase contraction pressure loss. Third, an intermediate cavity height results in a minimum leakage. This is because an intermediate cavity height leads to the largest mainstream expansion. However, changing the cavity length has a more significant effect than changing the cavity height. If the total length and number of teeth are fixed in a design, the cavity length should be maximized. However, some restrictions exist for the width of a given tooth. For example, it should be thick enough to bear the pressure difference. Due to these restrictions, an optimization procedure for supercritical fluid labyrinth seals is proposed. This is done by adding teeth into the labyrinth seal one by one, until adding more teeth resulted in an increased leakage rate. This observation is confirmed by the parametric study of the number of teeth.

5.3 Geometry 3: Valves

Most manufacturers evaluate valves using water or air. Research data on valves with supercritical fluid is currently not available. This section is focused on measuring mass flow rate through valves with supercritical fluid. However, only S-CO_2 flow is studied, as the experimental data for SCW is not available. This section is divided into five parts. The first subsection introduces the experiment setup for valve testing. Then, the experiment data from this test are used to validate the proposed numerical methodology. After that, a real S-CO_2 Brayton cycle design is used for valve selection. Meanwhile the empirical gas service valve model is also examined with both experimental and numerical data. The following subsection investigates the issues of cavitation and Mach number. The final subsection ends with a brief summary.

5.3.1 Experiment setup

The Metering Valve SS-31RS4 by Swagelok [69] was tested in the experiment because it is already in use within the experiment to adjust the flow. As a consequence, testing this valve requires minimal changes to the experimental facility. This valve has an orifice diameter of 0.064 in, which results in a nominal valve coefficient of 0.04. The dimensions and the inner geometry are presented in Figure 63. The pressure drop and mass flow rate across this valve are measured. This valve is connected to the test section inlet as show in Figure 64. The subassembly in the reservoir tank is taken out, leaving it serving to maintain stable downstream conditions.

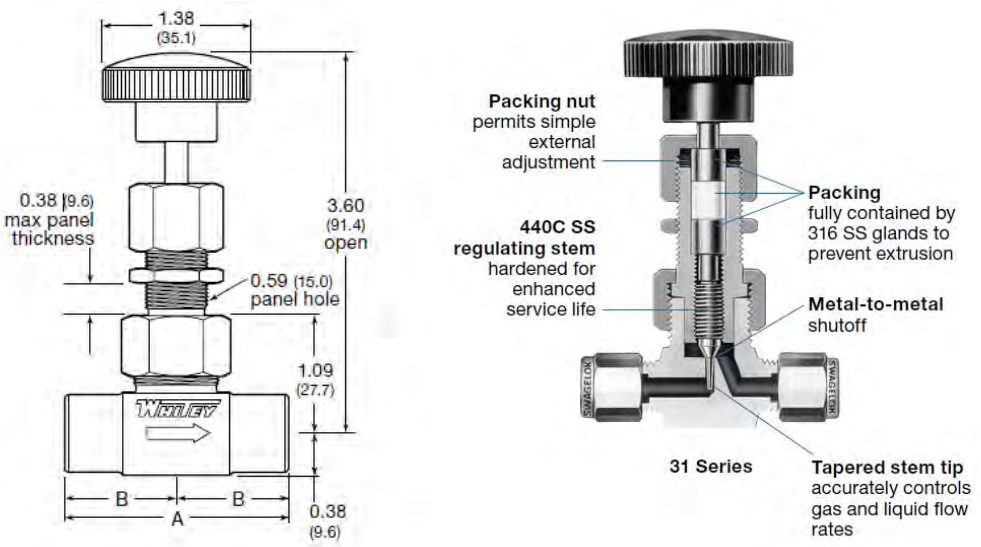

Figure 63 Dimensions and inner geometry of SS-31RS4 [69]

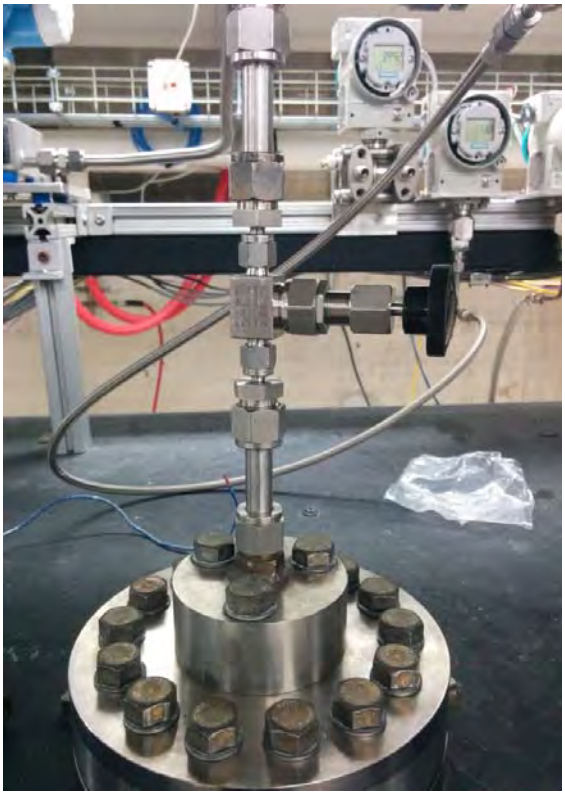

Figure 64 Test valve connected to test loop

5.3.2 Validation with experimental data

The geometry of the same valve in last subsection is simulated and compared with experimental data. Its computational domain is described in Figure 65. In order to save computational time, axisymmetric geometry was used to approach this problem. The simulation geometry mimics the behavior of the plug and seat. With the help of a high accuracy optical measurement method, the dimensions of the plug and seat can be determined precisely. Details of the optical measurement can be found in Appendix E.

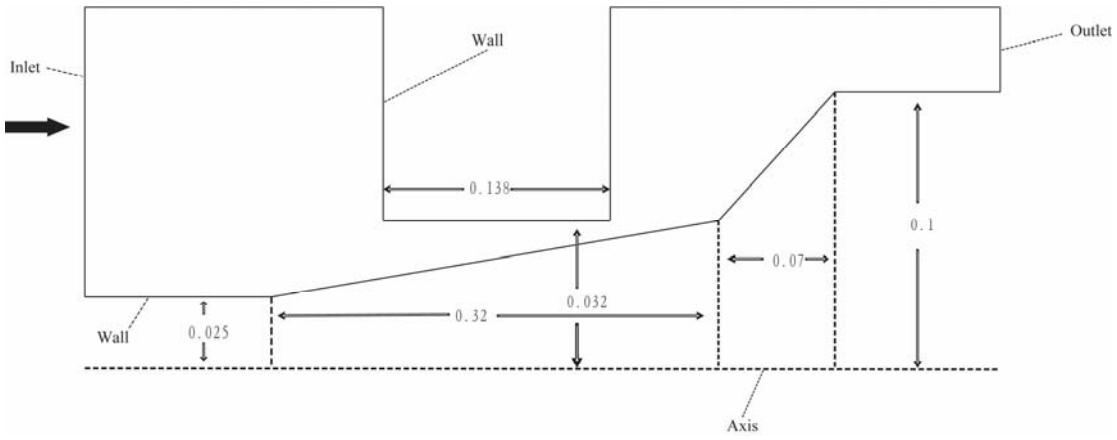

Figure 65 Computational domain for test valve geometry

Figure 66 presents the data from experiment and simulation for different open percentages at the same upstream condition of 7.7 MPa at 498 kg/m^3. The upstream condition of 12.5 MPa at 425 kg/m^3 was also tested for the 50%-open valve, and the data are shown in Figure 67. The proposed numerical methodology predicts valve's mass flow rates with a very good accuracy. Thus, it is feasible to use the proposed numerical methodology to inspect valve with supercritical fluid when an experimental approach is not available.

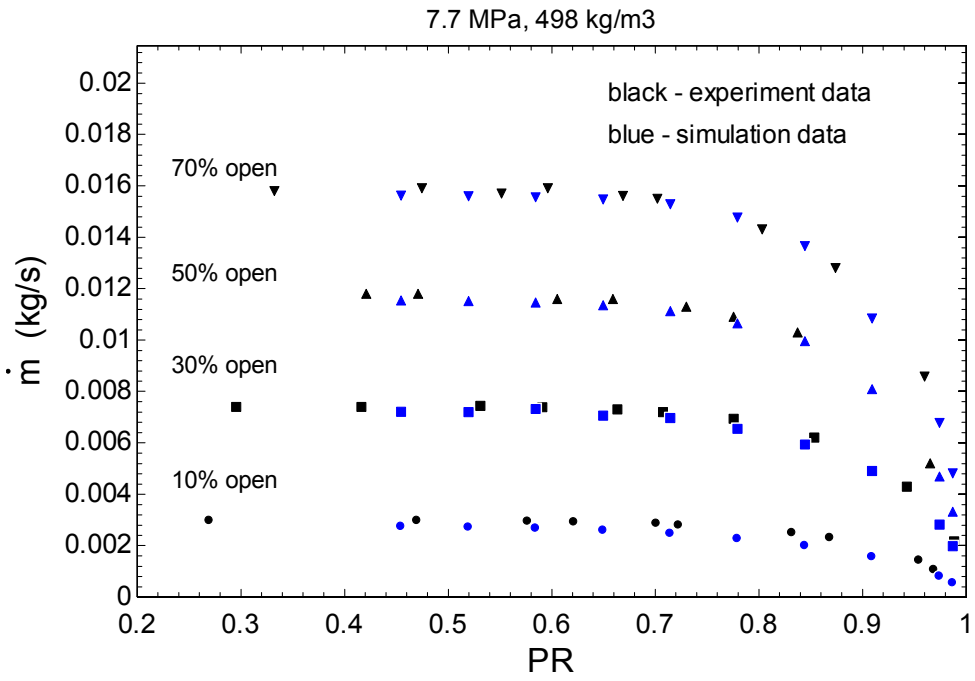

Figure 66 Comparison of experiment and simulation for test valve for 7.7 MPa at 498 kg/m^3

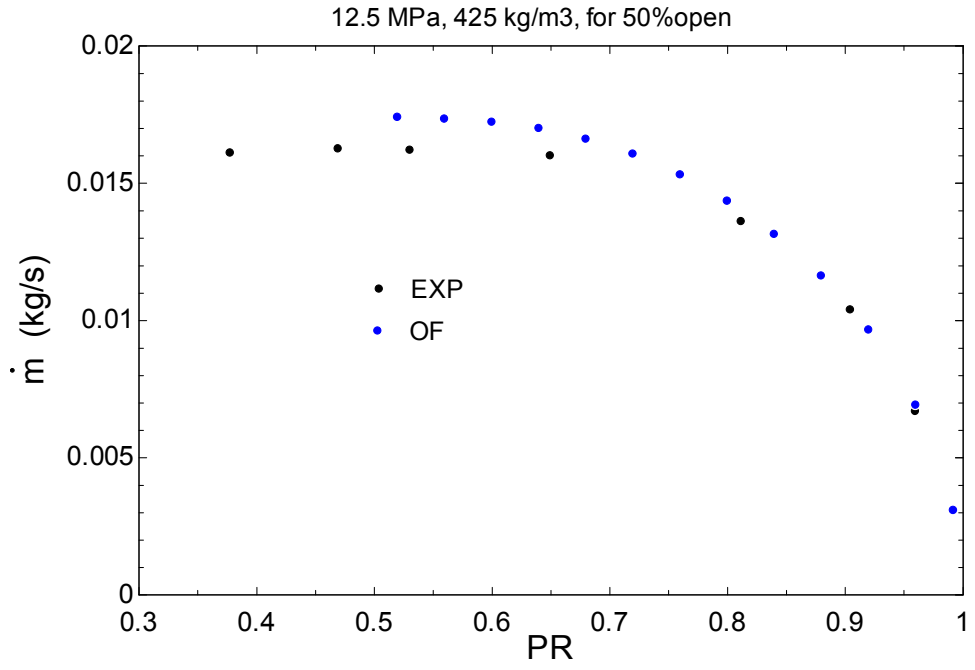

Figure 67 Comparison of experiment and simulation for test valve for 12.5 MPa at 425 kg/m^3 at 50% open

In the rest of this part, the proposed modification of the gas service valve model is examined with experimental and numerical data to demonstrate its improvement. The gas service valve model is discussed in section 2.5.2. The 50%-open valve with the upstream condition of 7.7 MPa at 498 kg/m^3 is used as an example. Figure 68 shows the valve coefficient changes with number of turns provided by manufacturer. For the 50%-open valve, which is 5 turns in Figure 68, the valve coefficient is around 0.015. However, from both experiment and simulation, the valve coefficient is 0.02 at a low-pressure drop. Figure 69 demonstrates the mass flow rate from experiment, simulation, and model. As can be seen, using the valve coefficient of 0.015 underestimates the mass flow rate at high pressure ratios, and using the value of 0.02 overestimates the mass flow rate at low pressure ratios for the original gas service valve model in Equation 8. Figure 69 also presents the results from the modified gas service valve model. The modified model with a valve coefficient of 0.02 matches the experimental data best.

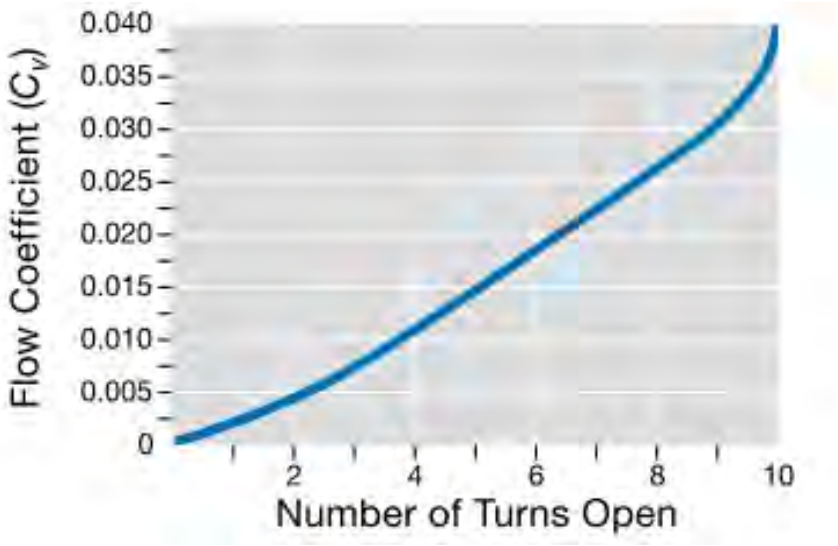

Figure 68 Valve coefficient changes with number of turns for tested valve

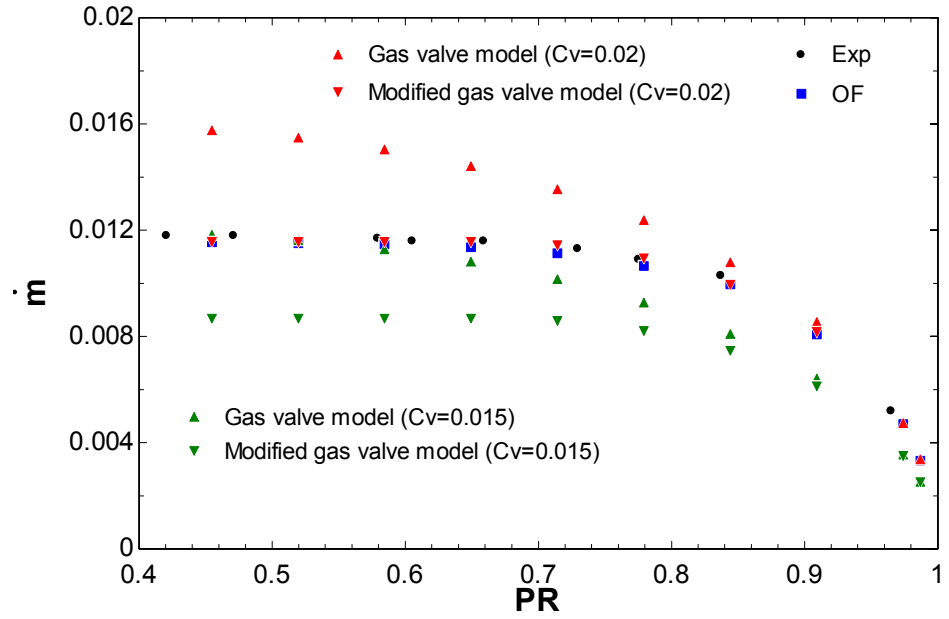

Figure 69 Mass flow rate of valve from different sources at 50% open

5.3.3 Valve selection

Two typical cycle transients calculated by Moisseytsev [45] are used to help valve selection. One transient is a shutdown process, while the other is a down-up process. These transient data provide the upstream and downstream conditions of each valve, as well as the mass flow rates through them. The valve coefficients are calculated at each time step, thus providing their maximum values in Table XI. The corresponding upstream and downstream conditions are presented as well.

In Table XI, valves are significantly different in their requirements. The valves for bypass control, such as TBPv, RBPv, and CBPv, require large valve coefficients. These valves usually have a large amount of flow and a relative small pressure drop. This means that the traditional method is working for these valves, and the nominal valve coefficient values provided by manufacturers could be directly used. However, valves for inventory control, such as INVIv and INVOv, only need small valve coefficients. And the pressure drop is relative large at their maximum valve coefficients. This means S-CO_2 property changes should be considered. As a result in the following part of this section, valve selections for INVIv and INVOv are performed.

Table XI Max valve coefficients

Condition at max Cv	TBPv	RBPv	CBPv	INVIv	INVOv
Cv_{max}	7489.99	14818.44	5552.48	29.13	25.74
P_{inlet} (MPa)	7.67	16.0	7.68	15.0	8.52
P_{outlet} (MPa)	7.58	15.9	7.66	14.0	7.61
T_{inlet} (°C)	327.81	210.11	85.26	87.75	42.27
T_{outlet} (°C)	347.33	339.92	33.00	70.30	89.08
ρ_{inlet} (kg/m^3)	68.65	195.94	146.31	382.90	313.71
ρ_{outlet} (kg/m^3)	65.46	140.15	381.09	452.24	141.31
$\dot{m}$ (kg/s)	438.15	703.05	231.39	13.98	10.41

The nuclear application valve report from Flowserve [70] helps valve selection. According to the pressure and temperature range of the S-CO_2 Brayton cycle, all valves should be in Class 1500. Parameters of the Class 1500 globe valve are presented in Table XII. In Table XII, the valve with 2.5 in Nominal Pipe Size (NPS) provides the valve coefficient needed by INVIv and INVOv. However, the parameters in Table XII are obtained from traditional tests using water and air. It is necessary to perform experimental or numerical study under S-CO_2 conditions. The current test facility at UW-Madison cannot provide the mass flow rate for a valve with 2.5 in NPS. As a consequence, only the numerical approach is used. The valve's seat and plug geometries are presented in Figure 70 for the globe valve by Flowserve [70]. There are three types of plug, standard, cage, and parabolic, presented in Figure 70. For a better control, the parabolic plug should be selected. Figure 71 shows the computational domain for this globe valve with a parabolic plug with 50%-open. The valve at 100%-open is not tested, as a three-dimension simulation is needed, which requires a lot computational resource. The conditions in Table XI for INVIv and INVOv are tested to see if the selected 2.5 in NPS valve can provide the required valve coefficients.

Table XII Class 1500 globe valve's maximum valve coefficient by Flowserve [70]

NPS (in)	2.5	3	4	6	8
Max Cv	83.3	119	201	435	733

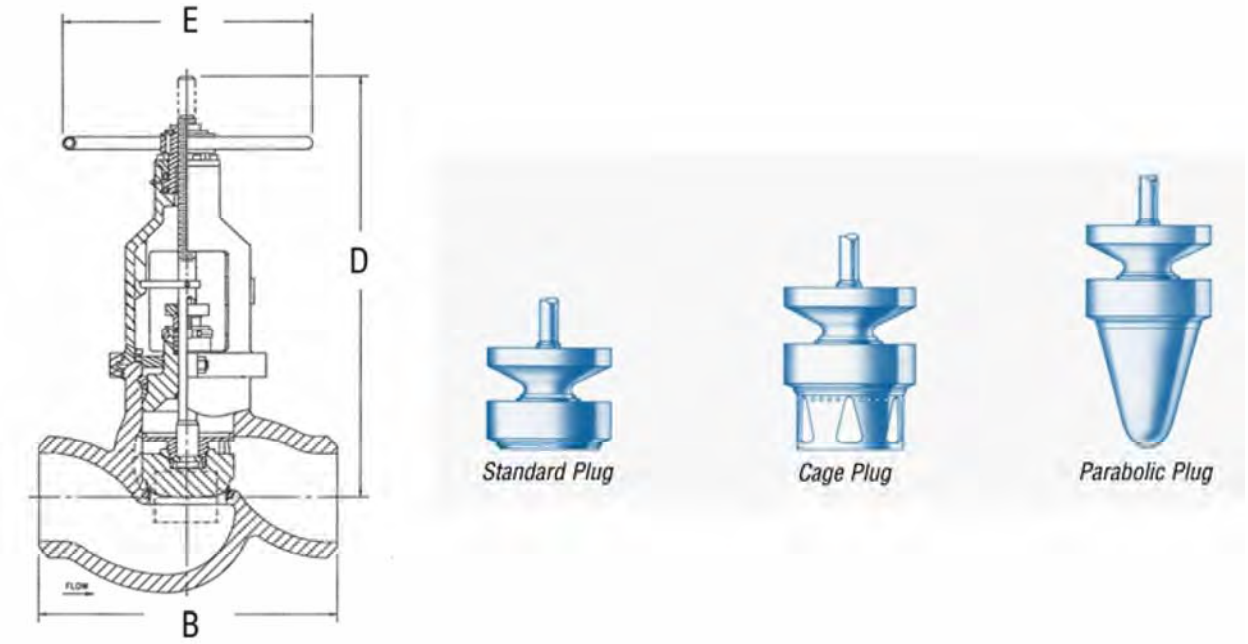

Figure 70 Globe valve by Flowserve[70]

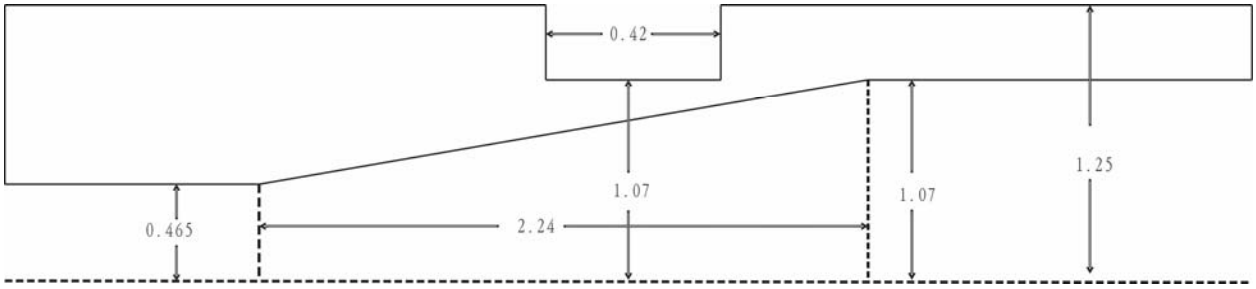

Figure 71 Computational domain for globe valve by Flowserve

In the following part, three upstream conditions are tested (shown in Figure 72) for the geometry in Figure 71. Figure 73, Figure 74, and Figure 75 present the data with upstream conditions of 7.7 MPa at 498 kg/m^3, 8.5 MPa at 313 kg/m^3, and 15 MPa at 383 kg/m^3 respectively. This 50%-open valve has a valve coefficient of 63, which is obtained from the numerical data at a low-pressure drop. With this valve coefficient, the modified gas service valve model provides a very good prediction of the mass flow rate. In Figure 75, when

the upstream condition is far away from the critical point, the traditional model works every good, and the modification only brings a small improvement. However, when the upstream condition is close to the critical point, like what in Figure 73 and Figure 74, the modification introduces a great improvement.

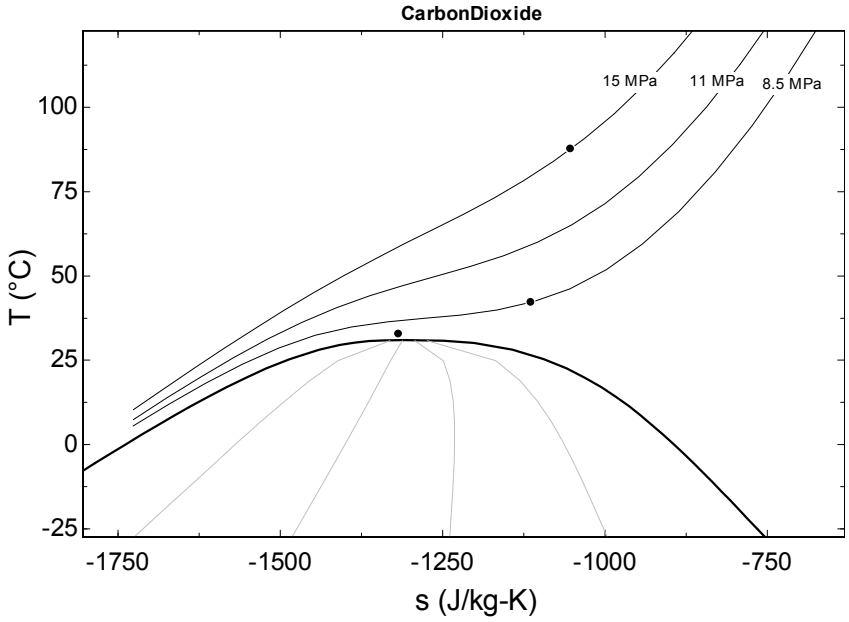

Figure 72 Tested upstream conditions

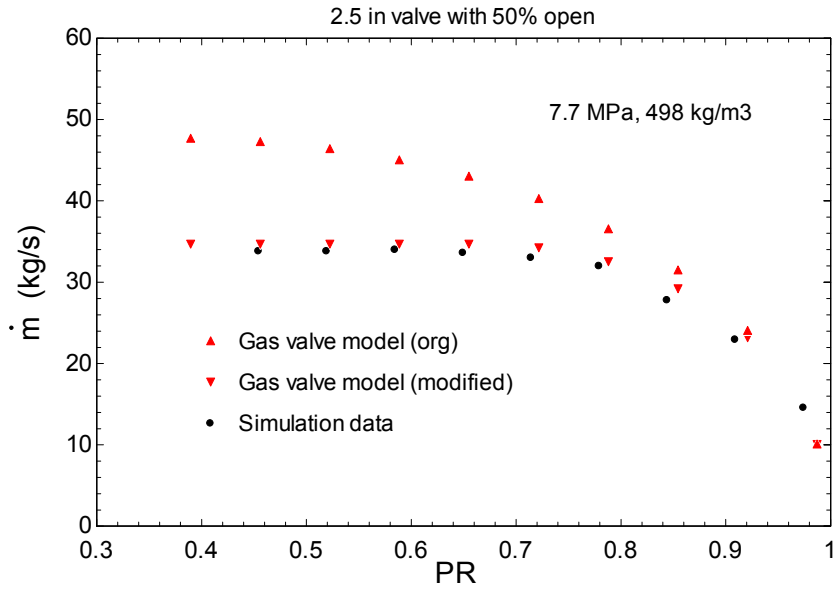

Figure 73 Globe valve with 50% open with upstream condition of 7.7 MPa at 498 kg/m^3

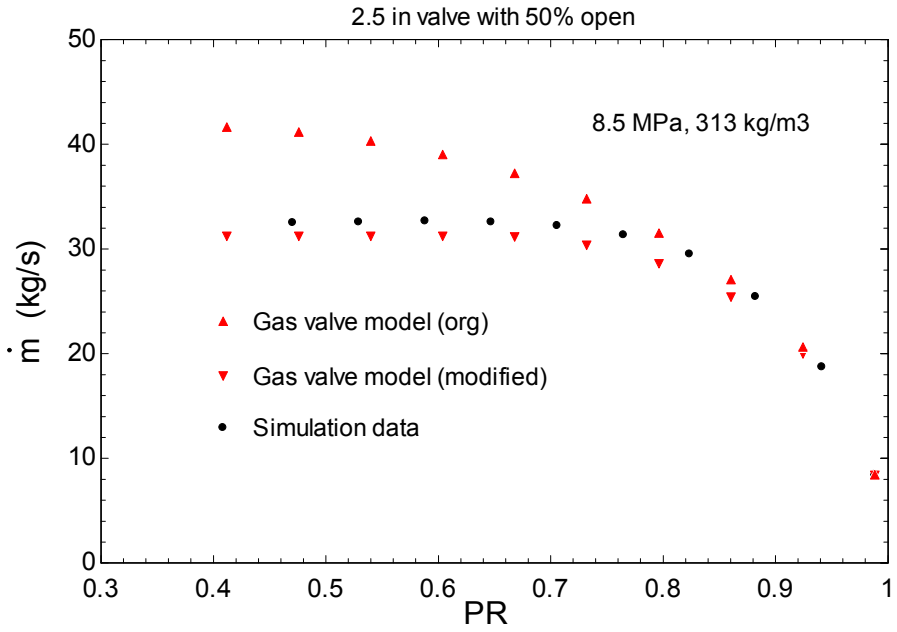

Figure 74 Globe valve with 50% open with upstream condition of 8.5 MPa at 313 kg/m^3

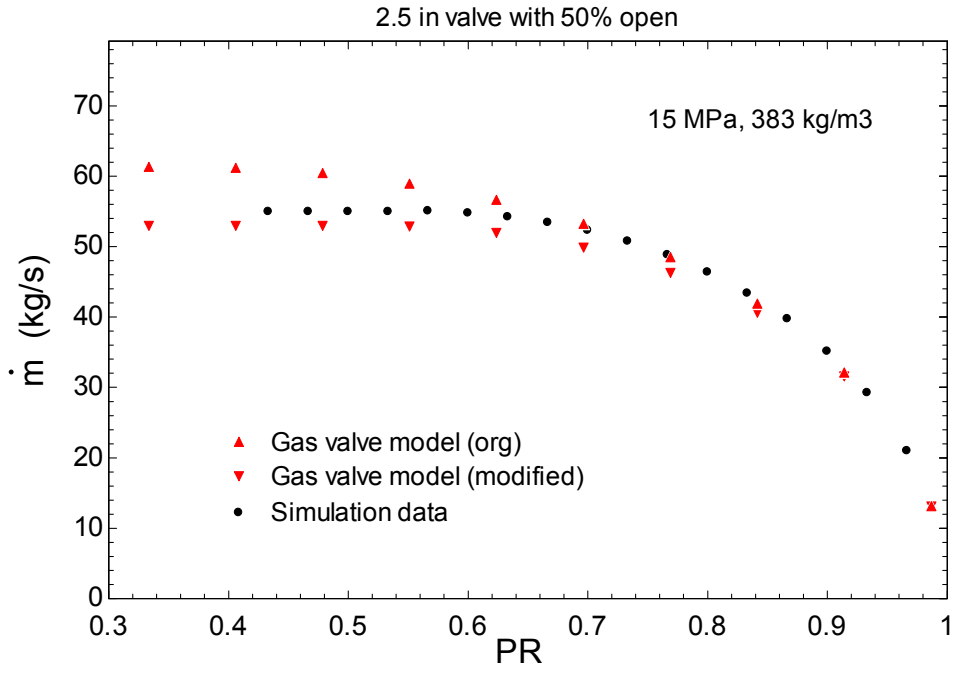

Figure 75 Globe valve with 50% open with upstream condition of 15 MPa at 383 kg/m^3

5.3.4 Mach number and cavitation

After valves are selected, Mach number and cavitation should be inspected. This can only be achieved by examine numerical data. Figure 76 and Figure 77 show the Mach number distribution for the 2.5 in NPS valve at the conditions in Table XI for INVIv and INVOv. The calculation of the Mach number is discussed in section 2.5.2. As the maximum Mach numbers are less than one for both cases, it is feasible to use this valve. For the conditions represented in Figure 76 and Figure 77, the two-phase scenario does not appear. However, if further reducing the downstream pressure, the two-phase scenario appears. As HEM is implemented to model two-phase flow, the cavitation phenomenon cannot be represented with a visualization of bubble formation and collapse. A very qualitative representation of cavitation is presented. Figure 78 and Figure 79 present the quality distribution for reduced downstream pressures at the condition in Figure 76 and Figure 77. Even though downstream conditions are not in the region of two-phase, the cavitation still appears. Therefore, a special design or material should be implemented at the location of cavitation.

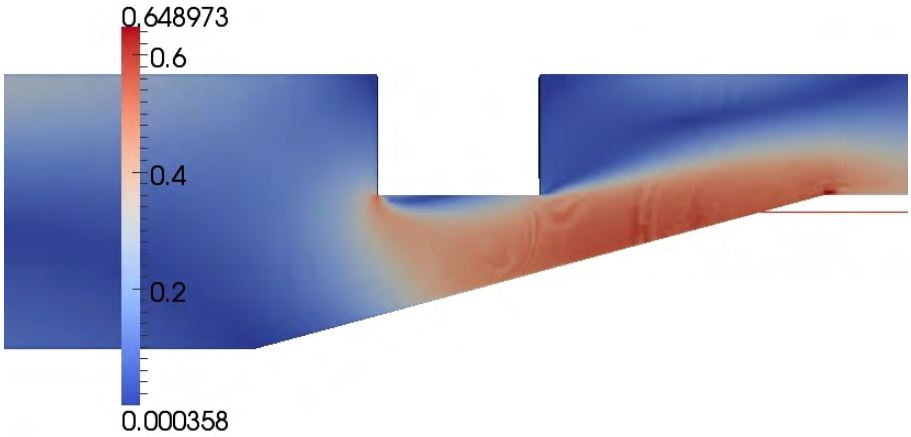

Figure 76 Mach number of upstream of 8.5 MPa at 313 kg/m^3, and downstream of 7.6 MPa

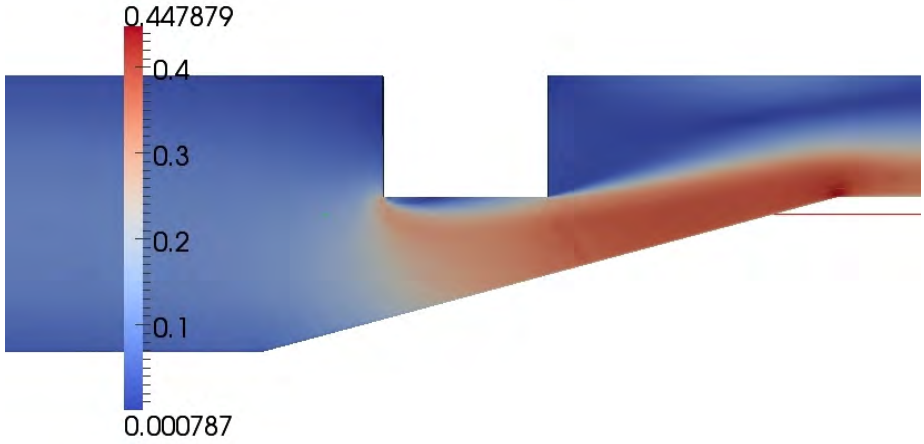

Figure 77 Mach number of upstream of 15 MPa at 383 kg/m^3, and downstream of 14 MPa

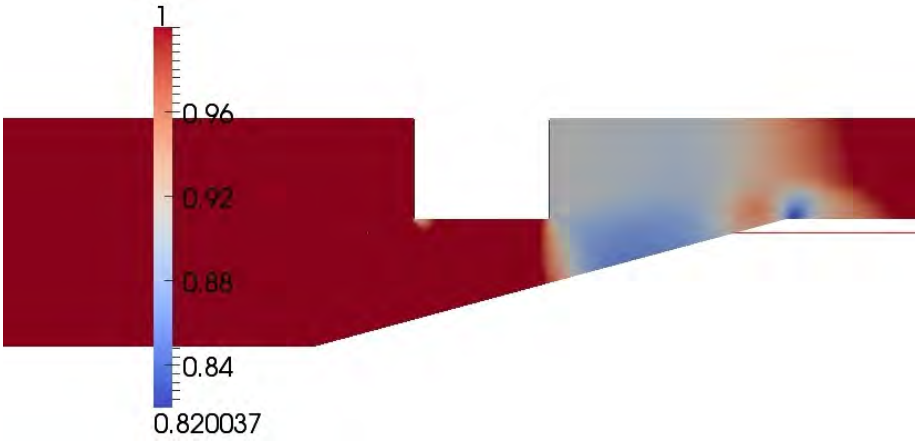

Figure 78 Quality of upstream of 8.5 MPa at 313 kg/m^3, and downstream of 7.0 MPa

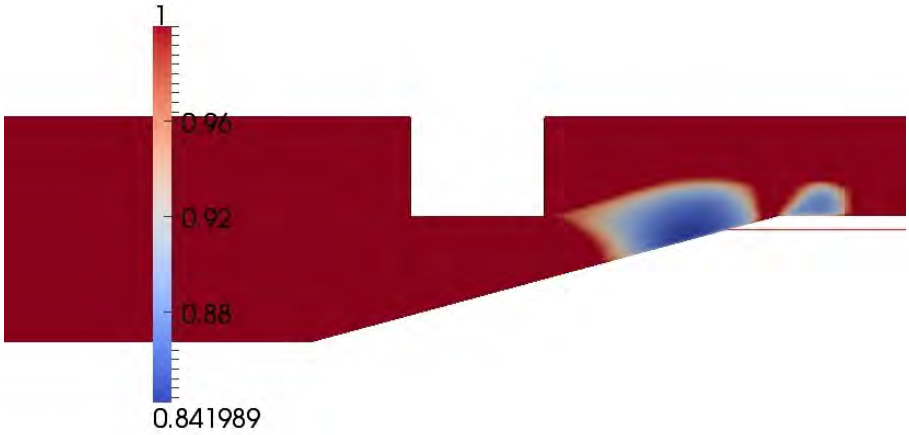

Figure 79 Quality of upstream of 15 MPa at 383 kg/m^3, and downstream of 9.0 MPa

5.3.5 Summary

In this chapter, a study of valve is performed under the S-CO_2 flow condition. Experiment was conducted for a small-scale valve to provide validation data. The developed numerical methodology was examined under the same geometry and conditions. The comparison of numerical and experimental data is successful. The S-CO_2 Brayton cycle design by Moisseytsev [45] was used to demonstrate the process of valve selection. The maximum valve coefficients for each valve were calculated under cycle transients. After the valve size was determined for each valve, the proposed numerical method inspects the selected valve when the experiment is not available. The traditional gas service valve model is also compared with experimental and numerical data. And the proposed modification introduces a great improvement when the tested condition is near the critical point. The Mach number and cavitation phenomenon were also inspected using numerical data.

6. Conclusion

In this research, a CFD methodology was proposed to simulate supercritical and two-phase fluid flow. The open source CFD code OpenFOAM served as the platform due to its high flexibility and wide usage. The solver was modified to use the real fluid properties. A real fluid property module, called FIT, was used to provide accurate supercritical and two-phase fluid properties with an increased computational speed versus REFPROP. The HEM was implemented to calculate two-phase properties. The standard k-epsilon model was used to model turbulence.

Three example geometries, including orifices, labyrinth seals, and valves, were studied to validate the proposed methodology with available experimental data. For orifices, two different supercritical fluids, S-CO_2 and SCW, were used for this study. The simulation of S-CO_2 was very successful, predicting the mass flow rate through an orifice within a 5% maximum difference versus experimental data. Several efforts were made to achieve this improvement. First, the proposed methodology uses a more accurate real fluid module to provide properties. Second, the upstream condition is determined by pressure and density, which determines a supercritical state more precisely than the traditional method using pressure and temperature. The numerical data for SCW also agree with experiment for the choked mass flow rate showing the extensibility of the proposed methodology. It is believed that other supercritical fluids could be studied using the same method.

The geometry of labyrinth seals was also studied. After successful comparisons of experiment and simulation, some parametric studies were performed to study geometric effects on the leakage rate. Adding more teeth or cavity area both decreases the leakage rate. However, a balance is needed, as total length and tooth width are restricted. Based on these observations, an optimum design for the see-through labyrinth seal was proposed.

In the study of valves, the proposed numerical methodology predicted the mass flow rate for the tested valve very well. After that, a demonstration of valve selections for a real S-CO_2 Brayton cycle design was

presented. The tradition gas service valve model was also examined with its limitations pointed out for supercritical fluid. A modification was proposed to improve the gas service valve model with a new choked flow check method, in order to have a better mass flow rate prediction near the critical point.

7. Open issues and future work

The open issues and future work related to this research are discussed in this chapter, and several limitations of the current methodology are also listed. First, only HEM was used to model two-phase flow. As discussed previously, HEM was proved to be applicable to the problem in this research. However, if the condition is changed, HEM may not work as well as it is in this problem. At the current stage, two-phase flow can only be represented by quality distribution. If more details about the flow, such as phase distribution, bubble/droplet formation/collapse, are interested, then more advanced two-phase models should be implemented. Second, the heat transfer phenomenon is not a major concern in this research, which leads to the currently used standard k-epsilon model working well. However, the standard k-epsilon model introduced redundant dissipation into the flow, eliminating detailed flow structures. Third, as the flow reaches Mach 1.0 when choked, the first order upwind numerical scheme for convection tern was used to insure stability, which also introduced redundant dissipation. As a result, if more details of the flow are interested, more advanced two-phase and turbulence models, and higher order numerical scheme should be used.

Based on the developed methodology, future work can be performed on different perspectives. First, more advanced seal designs, such as dry gas seal, pocket damper seal, could be analyzed using the same method for supercritical fluid. Second, the compressor blade design can be studied for supercritical fluid using the methodology developed in this research. The possible appearance of two-phase can be represented; however, due to the current usage of HEM, the cavitation phenomenon cannot be represented precisely. In order to study the detail of cavitation and the damage associate with it, advanced two-phase model should be used or developed. Third, with the accurate property module of supercritical fluid, heat transfer could be studied, which is another big topic for supercritical fluid flow.

Reference

[1] ANSYS Inc, "ANSYS-FLUENT User ' s Guide," no. April. 2009.

[2] E. W. Lemmon, M. L. Huber, and M. O. Mclinden, "NIST Reference Fluid Thermodynamic and Transport Properties-REFPROP," Boulder, Colorado, 2007.

[3] Northland Numerics, "FIT," 2012. [Online]. Available: http://www.northlandnumerics.com/.

[4] S. Klein and G. Nellis, *Thermodynamics*. Cambridge University Press, 2012.

[5] F-Chart Sofrware, "Engineering Equation Solver." 1993.

[6] K. Dobashi, a. Kimura, Y. Oka, and S. Koshizuka, "Conceptual design of a high temperature power reactor cooled and moderated by supercritical light water," *Ann. Nucl. Energy*, vol. 25, no. 8, pp. 487–505, May 1998.

[7] Y. Oka and S. Koshizuka, "Supercritical-pressure, Once-through Cycle Light Water Cooled Reactor Concept," *J. Nucl. Sci. Technol.*, vol. 38, no. 12, pp. 1081–1089, Dec. 2001.

[8] Y. Oka, S. Koshizuka, and T. Yamasaki, "Direct Cycle Light Water Reactor Operating at Supercritical Pressure," *J. Nucl. Sci. Technol.*, vol. 29, no. 6, pp. 585–588, Jun. 1992.

[9] M. Chatharaju, "Computational Study of Critical Flow Discharge in Supercritical Water Cooled Reactors Computational Study of Critical Flow Discharge in Supercritical Water Cooled Reactors," McMaster University, 2011.

[10] J. Wright and J. Patterson, "Status and Application of Supercritical Water Reactor Coolant," in *Proceedings of the American Power Conference*, 1966.

[11] A. Bishop, L. Efferding, and L. Tong, "A review of heat transfer and fluid flow of water in the supercritical region and during 'once-through' operation," *Rep. WCAP-2040, Westinghouse Electr. Corp. At. Power Div. Pittsburgh, PA, USA*, p. 106, 1962.

[12] P. S. Weitzel, "Steam Generator for Advanced Ultra-Supercritical Power Plants 700 to 760C," in *Proceedings of the ASME 2011 Power Conference*, 2011.

[13] V. Dostal, "A Supercritical Carbon Dioxide Cycle for Next Generation Nuclear Reactors," Doctoral dissertation, Massachusetts Institute of Technology, 2004.

[14] V. Dostal, P. Hejzlar, and M. J. Driscoll, "THE SUPERCRITICAL CARBON DIOXIDE POWER CYCLE : COMPARISON TO OTHER ADVANCED POWER CYCLES," *Nucl. Technol.*, vol. 154, no. 283–301, 2006.

[15] S. A. Wright, R. F. Radel, M. E. Vernon, G. E. Rochau, and P. S. Pickard, "Operation and Analysis of a Supercritical CO 2 Brayton Cycle," Albuquerque, New Mexico and Livermore, California, USA, 2010.

[16] S. A. Wright, M. E. Vernon, and P. S. Pickard, "Concept Design for a High Temperature Helium Brayton Cycle with Interstage Heating and Cooling," Albuquerque, New Mexico and Livermore, California, USA, 2006.

[17] M. J. Schuler, T. Rothenfluh, and P. Rudolf von Rohr, "Numerical analysis of penetration lengths in submerged supercritical water jets," *J. Supercrit. Fluids*, vol. 82, pp. 213–220, Oct. 2013.

[18] A. Farah, P. Haines, G. Harvel, and I. Pioro, "Sensitivity analysis of CFD code FLUENT-12 for supercritical water heat transfer in vertical bare tubes," in *proceeding of the 2012 20th international conference on nuclear engineering collocated with the ASME 2012 Power conference*, 2014, pp. 1–9.

[19] E. Ampomah-Amoako, E. H. K. Akaho, B. J. B. Nyarko, and W. Ambrosini, "CFD analysis of the dynamic behaviour of a fuel rod subchannel in a supercritical water reactor with point kinetics," *Ann. Nucl. Energy*, vol. 59, pp. 211–223, Sep. 2013.

[20] Y. Chen, M. Zhao, C. Yang, K. Bi, K. Du, and S. Zhang, "Critical Flow of Water Under Supercritical Pressures," in *2010 14th International Heat Transfer Conference, Volume 2*, 2010, pp. 319–326.

[21] A. K. Yadav, M. Ram Gopal, and S. Bhattacharyya, “CO2 based natural circulation loops: New correlations for friction and heat transfer,” *Int. J. Heat Mass Transf.*, vol. 55, no. 17–18, pp. 4621–4630, Aug. 2012.
[22] E. Van Abel, M. Anderson, and M. Corradini, “Numerical Investigation of Pressure Drop and Local Heat Transfer of Supercritical CO 2 in Printed Circuit Heat Exchangers,” in *Supercritical CO2 Power Cycle Symposium, Boulder, Colorado*, 2011.
[23] I. P. Serrano, a. Cantizano, J. I. Linares, B. Y. Moratilla, I. Fernandez-Berceruelo, and L. Sedano, “Numerical modeling and design of supercritical CO2 pre-cooler for fusion nuclear reactors,” *Fusion Eng. Des.*, vol. 87, no. 7–8, pp. 1329–1332, Aug. 2012.
[24] a. Guardo, M. Coussirat, F. Recasens, M. a. Larrayoz, and X. Escaler, “CFD study on particle-to-fluid heat transfer in fixed bed reactors: Convective heat transfer at low and high pressure,” *Chem. Eng. Sci.*, vol. 61, no. 13, pp. 4341–4353, Jul. 2006.
[25] A. J. Suo-anttila and S. A. Wright, “Computational Fluid Dynamics Code for Supercritical Fluids,” in *Supercritical CO2 Power Cycle Symposium, Boulder, Colorado*, 2011.
[26] M. Fairweather, S. Falle, J. Hebrard, D. Jamois, C. Proust, C. Wareing, and R. Woolley, “Reynolds-Averaged Navier-Stokes Modelling of the Near-Field Structure of Accidental Releases of Carbon Dixxide from Pipelines,” in *Proceeding of the 22nd European Symposium on Computer Aided Process Engineering, London, UK*, 2012.
[27] G. P. Mignot, M. H. Anderson, and M. L. Corradini, “Measurement of supercritical CO2 critical flow: Effects of L/D and surface roughness,” *Nucl. Eng. Des.*, vol. 239, no. 5, pp. 949–955, May 2009.
[28] J. P. Chen, J. P. Liu, Z. J. Chen, and Y. M. Niu, “Trans-critical R744 and two-phase flow through short tube orifices,” *Int. J. Therm. Sci.*, vol. 43, no. 6, pp. 623–630, Jun. 2004.
[29] J. P. Liu, Y. M. Niu, J. P. Chen, Z. J. Chen, and X. Feng, “Experimentation and correlation of R744 two-phase flow through short tubes,” *Exp. Therm. Fluid Sci.*, vol. 28, no. 6, pp. 565–573, Jun. 2004.
[30] C. Zhang and L. Yang, “Modeling of Supercritical CO2 Flow Through Short Tube Orifices,” *J. Fluids Eng.*, vol. 127, no. 6, p. 1194, 2005.
[31] L. Yang and C. Zhang, “Modified neural network correlation of refrigerant mass flow rates through adiabatic capillary and short tubes: Extension to CO2 transcritical flow,” *Int. J. Refrig.*, vol. 32, no. 6, pp. 1293–1301, Sep. 2009.
[32] Y. Chen, M. Zhao, C. Yang, K. Bi, K. Du, and S. Zhang, “Research on Critical Flow of Water under Supercritical Pressures in Nozzles,” vol. 6, pp. 201–208, 2012.
[33] H. J. Sneck, “Labyrinth Seal Literature Survey,” *J. Lubr. Technol.*, vol. 96, no. 4, pp. 579–581, 1974.
[34] C. Parsons, “The Labyrinth Packing,” *Engineer*, 1938.
[35] C. Parsons, “STANLEY SMITH COOK,” *US Pat. 1,374,520*, 1921.
[36] H. Martin, “Labyrinth packings,” *Engineering*, 1908.
[37] A. Egli, “The Leakage of Steam Through Labyrinth Seals,” *TRANS.ASME*, vol. 57, pp. 115–122, 1935.
[38] B. B. Hodkinson and A. M. E. Mech, “ESTIMATION OF THE LEAKAGE THROUGH A LABYRINTH GLAND,” in *Proceeding of the Institution of Mechanical Engineers*, 1939.
[39] A. M. . Eldin, “LEAKAGE AND ROTORDYNAMIC EFFECTS OF POCKET DAMPER SEALS AND SEE-THROUGH LABYRINTH SEALS LEAKAGE AND ROTORDYNAMIC EFFECTS OF POCKET DAMPER SEALS AND SEE-THROUGH LABYRINTH SEALS,” Texas A&M University, 2007.
[40] S. Wittig, U. Schelling, S. Kim, and K. Jacobsen, “Numerical predictions and measurements of discharge coefficients in labyrinth seals,” *... Gas Turbine Conf. Exhib. 32 ...*, 1987.
[41] D. Rhode, S. Ko, and G. Morrison, “Leakage optimization of labyrinth seals using a Navier-Stokes code,” *Tribol. Trans.*, 1994.

[42] V. Schramm, J. Denecke, S. Kim, and S. Wittig, “Shape Optimization of a Labyrinth Seal Applying the Simulated Annealing Method,” *Int. J. Rotating Mach.*, vol. 10, no. 5, pp. 365–371, Jan. 2004.
[43] S. Suryanarayanan, “LABYRINTH SEAL LEAKAGE EQUATION,” Texas A&M University, 2009.
[44] P. N. Jiang, W. Z. Wang, Y. Z. Liu, and G. Meng, “Influence of steam leakage through vane, gland, and shaft seals on rotordynamics of high-pressure rotor of a 1,000 MW ultra-supercritical steam turbine,” *Arch. Appl. Mech.*, vol. 82, no. 2, pp. 177–189, May 2011.
[45] A. Moisseytsev and J. Sienicki, “Development of a Plant Dynamics Computer Code for Analysis of a Supercritical Carbon Dioxide Brayton Cycle Energy Converter Coupled to a Natural Circulation Lead-Cooled Fast Reactor,” Chicago,IL,USA, 2006.
[46] P. L. Skousen, *VALVE HANDBOOK*. McGraw-Hill, 1998.
[47] J. P. Van Doormaal and G. D. Raithby, “Enhancements of The Simple Method for Predicting Incompressible Fluid Flows,” *Numer. Heat Transf.*, vol. 7, no. 2, pp. 147–163, Apr. 1984.
[48] S. Patankar, *Numerical heat transfer and fluid flow*. Taylor & Francis, 1980.
[49] M. Ishii and T. Hibiki, *Thermo-fluid Dynamics of Two-Phase Flow*. New York: Springer, 2011.
[50] F. J. Moody, “Maximum Flow Rate of a Single Component , Two-Phase Mixture,” *J. Heat Transfer*, vol. 87, no. 1, pp. 134–141, 1965.
[51] N. H. F. Fletcher, “Size Effect in Heterogeneous Nucleation,” *J.Chem.Phys*, vol. 29, no. 1, p. 572, 1958.
[52] D. W. Oxtoby and R. Evans, “Nonclassical nucleation theory for the gas–liquid transition,” *J. Chem. Phys.*, vol. 89, no. 12, p. 7521, 1988.
[53] D. . Aaron, “Experiments, analysis and correlation of Refrigerant-22 through short tube restrictors,” *ASHRAE Trans.*, vol. 96, no. 1, pp. 729–742, 1990.
[54] X. Fang, “Advances in Fixed-Area Expansion Devices Amana Refrigeration,” Urbana,IL, 1999.
[55] W. . Payne, “Multiphase flow of refrigerant R410A through short tube orifices,” *ASHRAE Trans.*, vol. 105, no. 2, pp. 66–72, 1999.
[56] M. F. Trujillo and A. E. Parkhill, “A local lagrangian analysis of passive particle advection in a gas flow field,” *Int. J. Multiph. Flow*, vol. 37, no. 9, pp. 1201–1208, 2011.
[57] M. L. Corraini, “Fundamentals of Multiphase Flow,” 1997. [Online]. Available: http://wins.engr.wisc.edu/teaching/mpfBook/. [Accessed: 04-Jul-2013].
[58] OpenCFD Limited, “OpenFOAM User Guide,” 2011. [Online]. Available: http://www.openfoam.org/docs/user/.
[59] OpenFOAM Foundation, “Open FOAM Programmer’s Guide,” 2011. [Online]. Available: http://www.foamcfd.org/Nabla/guides/ProgrammersGuide.html.
[60] H. Yuan, J. Edlebeck, M. Wolf, M. Anderson, M. Corradini, S. Klein, and G. Nellis, “Simulation of Supercritical CO2 Flow through Circular and Annular Orifice,” *J. Nucl. Eng. Radiat. Sci.*, 2014.
[61] L. Qiu, Y. Wang, and R. D. Reitz, “On regular and retrograde condensation in multiphase compressible flows,” *Int. J. Multiph. Flow*, vol. 64, no. 1, pp. 85–96, May 2014.
[62] J. Y. Yoo, “The Turbulent Flows of Supercritical Fluids with Heat Transfer,” *Annu. Rev. Fluid Mech.*, vol. 45, no. 1, pp. 495–525, Jan. 2013.
[63] S. He, W. S. Kim, and J. H. Bae, “Assessment of performance of turbulence models in predicting supercritical pressure heat transfer in a vertical tube,” *Int. J. Heat Mass Transf.*, vol. 51, no. 19–20, pp. 4659–4675, Sep. 2008.
[64] Y. Bae, S. Hong, and Y. Kim, “Numerical simulation of supercritical heat transfer under severe axial density gradient in a narrow vertical tube,” in *The 12th International Congress on Advances in Nuclear Power Plants, Chicago, Illinois*, 2012.
[65] M. Jaromin and H. Anglart, “A Numerical Study of The Turbulent Prandtl Number Impact on Heat Transfer to Supsercritical Water Flowing Upward Under Deteriorated Conditions,” in *The 15th International Topical Meeting on Nuclear Reactor Thermalhydraulics, Pisa, Italy*, 2013, p. 134.

[66] M. A. Rodarte, “The Development of an Experimental Test Facility to M easure Leakage through Labyrinth Seals,” Master Thesis, University of Wisconsin-Madison, 2011.
[67] M. Wolf, H. Yuan, and J. Edlebeck, “Measurements and Modelling of the Flow of Supercritical Carbon Dioxide through Orifices and Annuli,” in *ANS National Meeting*, 2013, pp. 2–5.
[68] J. P. Edlebeck, “Measurements And Modeling of The Flow of Supercritical Carbon Dioxide,” Master Thesis, University of Wisconsin-madison, 2013.
[69] “Metering Valves.” [Online]. Available: http://www.swagelok.com/downloads/webcatalogs/En/MS-01-142.pdf.
[70] “Edward and Anchor/Darling Nuclear Application Valves.” [Online]. Available: http://www.flowserve.com/files/Files/Literature/ProductLiterature/FlowControl/AnchorDarling/EVENCT0004-01.pdf.
[71] Alicona, “InfiniteFocus Metrology.” [Online]. Available: http://www.alicona.com/home/products/infinitefocus.html.

Appendix A：Drift number and Surface number

In this appendix, the drift and surface number calculations are discussed with more detail. There are two parts in this appendix. The first part discusses the drift number calculation; the second part presents the surface number calculation.

A.1 Drift number

In Section 3.3.2, the isentropic model and the Moody's slip ratio model are used to calculate the drift number. An example case with an upstream condition of 7.7 MPa, 498 kg/m^3 and an outlet pressure is 6 MPa is discussed. Other parameters from this calculation are presented in Table XIII. The calculated drift number is 0.082, which is much less than unity.

Table XIII Parameters for drift number calculation

	Mixture	Liquid phase	Gas phase
Density (kg/m^3)	358.1	750.1	210.9
Velocity (m/s)	89.64	66.77	102.0
Slip velocity (Gas-Mixture) (m/s)	12.32		
Drift number	0.082		

When the flow gets choked, further decreasing the downstream pressure does not change the mass flow rate and the flow condition inside the restriction. To further explore the drift number at different conditions, cases with upstream conditions on the saturation line are inspected. The lower limits of the choking downstream condition and the maximum drift numbers for the corresponding conditions could be calculated. To define an upper bound for the drift number that HEM is applicable, 0.1 was arbitrarily chosen which means when its value is less than 0.1, the drift term could be neglected. Figure 80 describes the drift number calculation discussed above. In Figure 80, there is a dashed line dividing two regions. In one region, the drift number is larger than 0.1, and in the other region it is less than 0.1. The tested upstream conditions for

circular orifice are also presented in Figure 80, and they are all in the region where the drift number is less than 0.1.

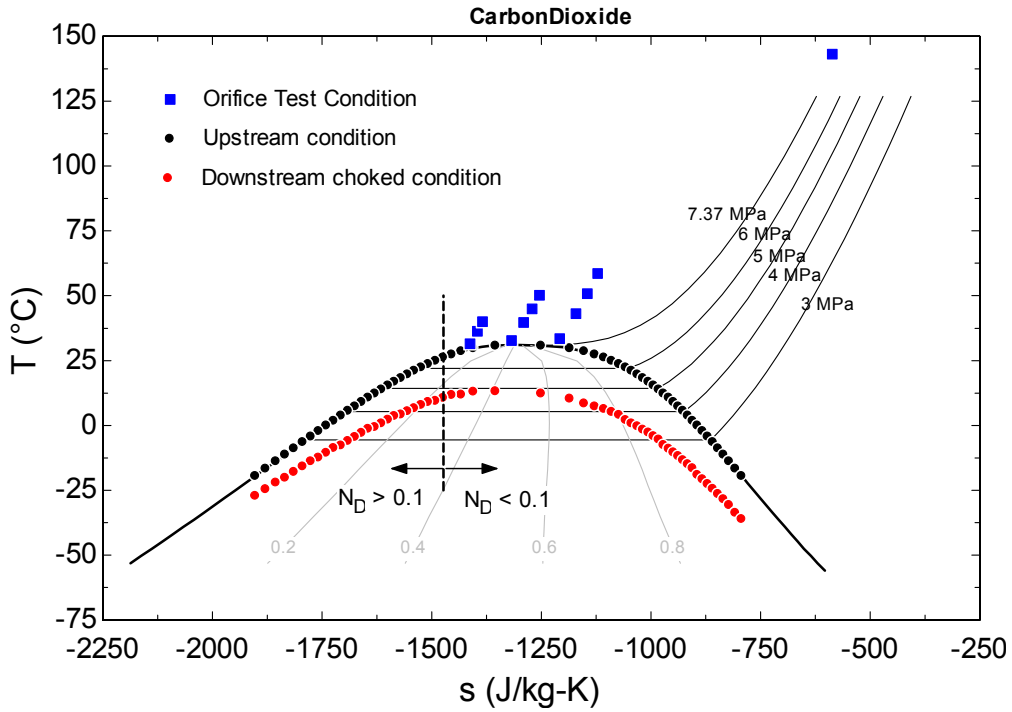

Figure 80 Drift number calculations for saturated upstream conditions

A.2 Surface number

In this part, the calculation of the surface number is discussed. As discussed in Section 3.3.3, the classical nucleation theory is used at the saturation point of 6 MPa. Figure 81 shows the position of the tested condition. The critical nucleus radius determined from Equation 40 is 2.9 μm, which is the minimum nucleus radius and results the maximum value of the surface number. The mixture velocity is assumed to be 40 m/s, which is a typical velocity in experiment and simulation. The calculated surface number is around 0.002, indicating that the drift term can be ignored in simulation. The parameters in this calculation are presented in Table XIV. Readers should know that, if the tested condition is closer to the critical point, the surface number gets even smaller.

Table XIV Parameters for surface number calculation

Nucleus radius (μm)	2.9

Surface tension (j/m^2)	0.0009308
Density (kg/m^3)	210.9
Velocity (m/s)	40
Surface number	0.001881

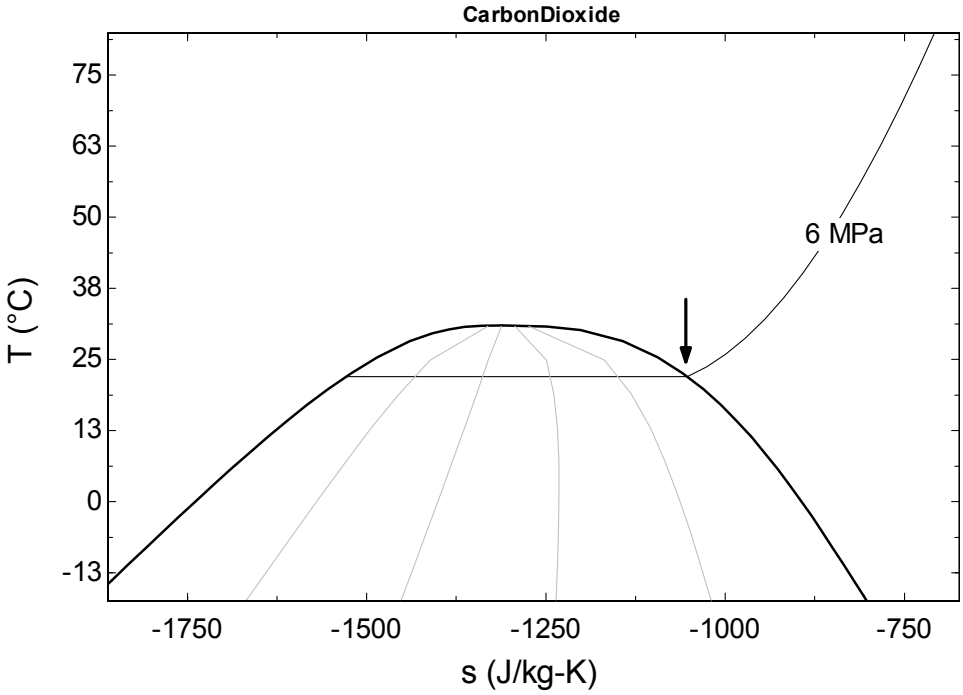

Figure 81 Saturation point at 6 MPa

Appendix B: More data for orifices

B.1 Simulation data for circular orifice

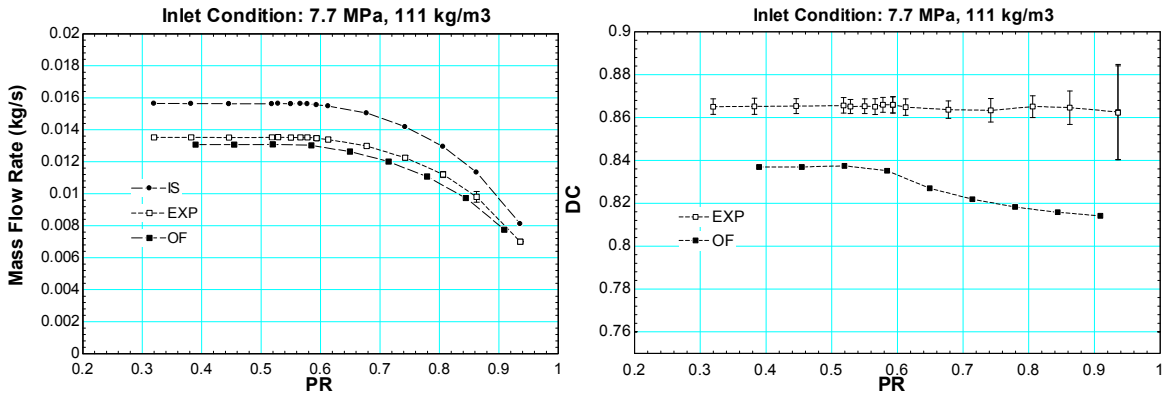

Figure 82 Circular orifice data for inlet condition of 7 MPa, 111 kg/m^3

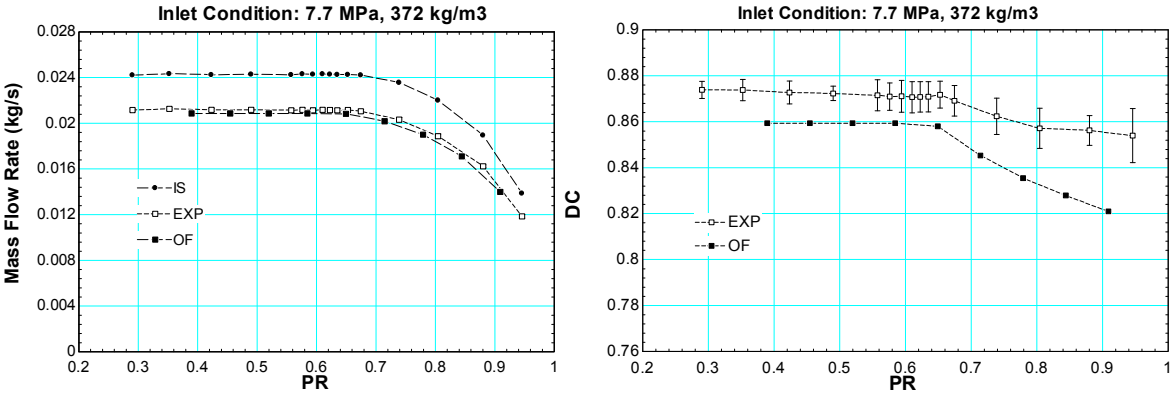

Figure 83 Circular orifice data for inlet condition of 7 MPa, 327 kg/m^3

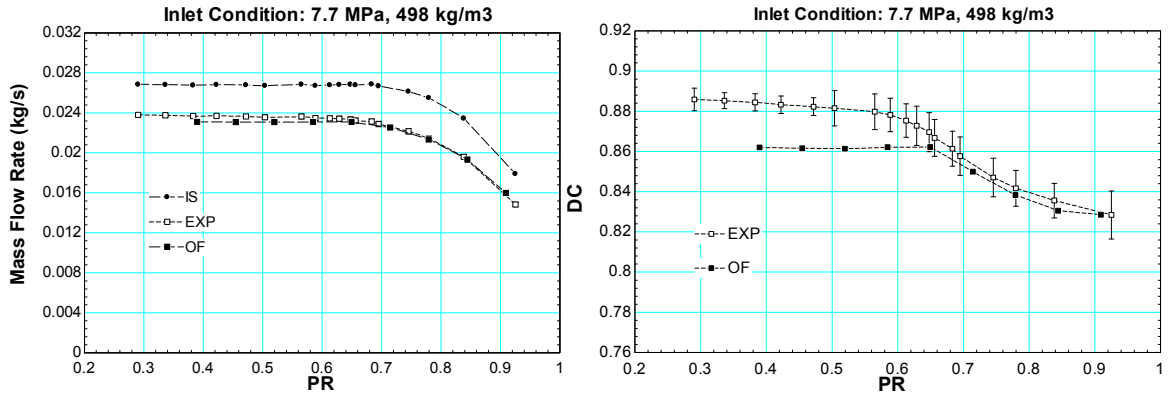

Figure 84 Circular orifice data for inlet condition of 7 MPa, 498 kg/m^3

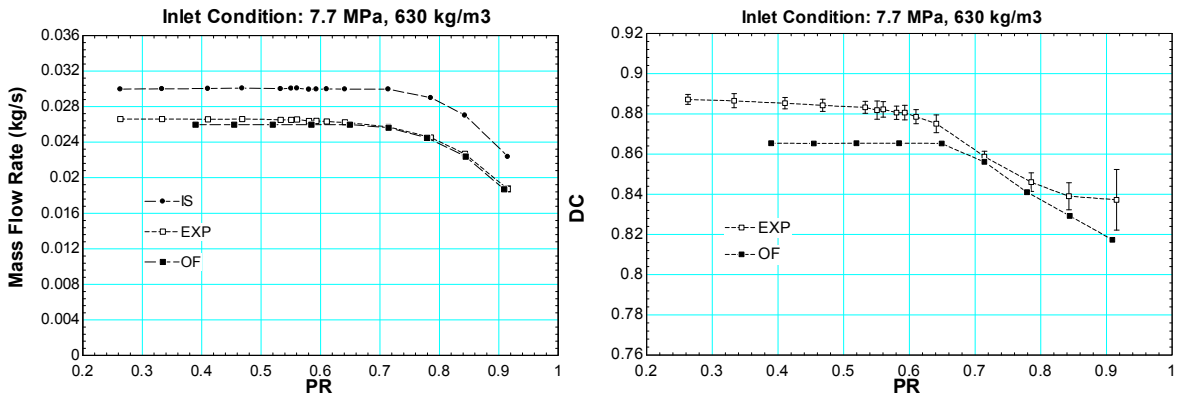

Figure 85 Circular orifice data for inlet condition of 7 MPa, 630 kg/m^3

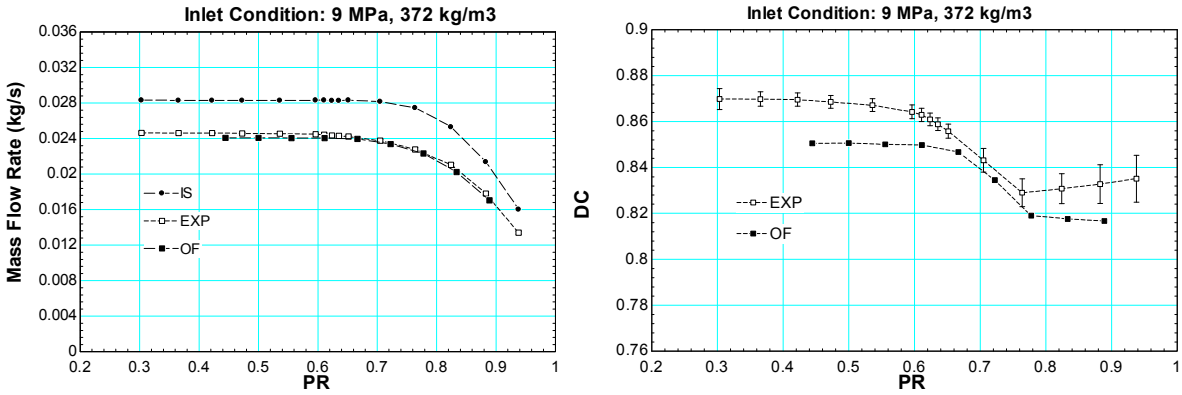

Figure 86 Circular orifice data for inlet condition of 9 MPa, 372 kg/m^3

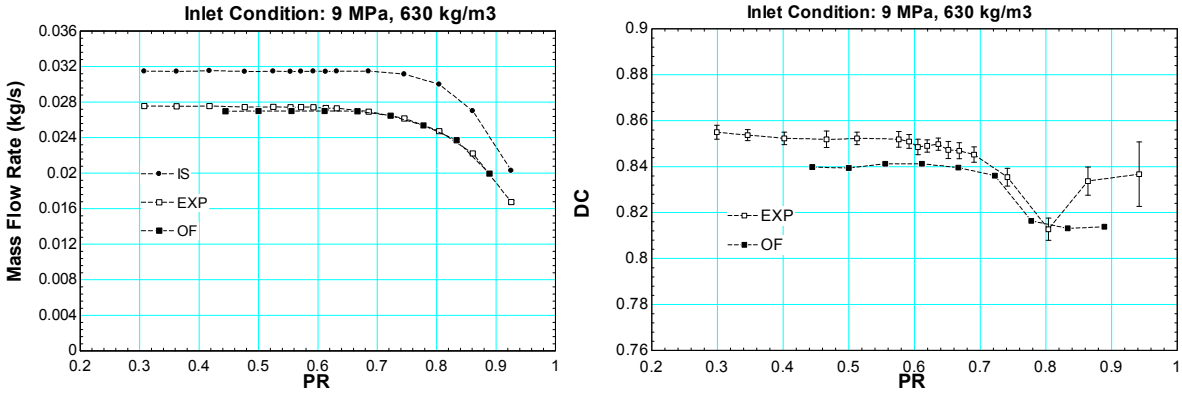

Figure 87 Circular orifice data for inlet condition of 9 MPa, 630 kg/m^3

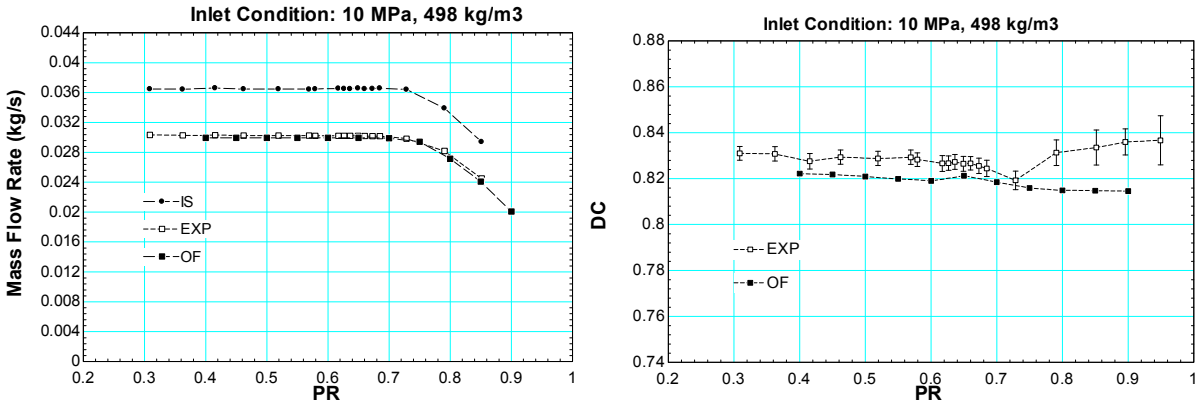

Figure 88 Circular orifice data for inlet condition of 10 MPa, 498 kg/m^3

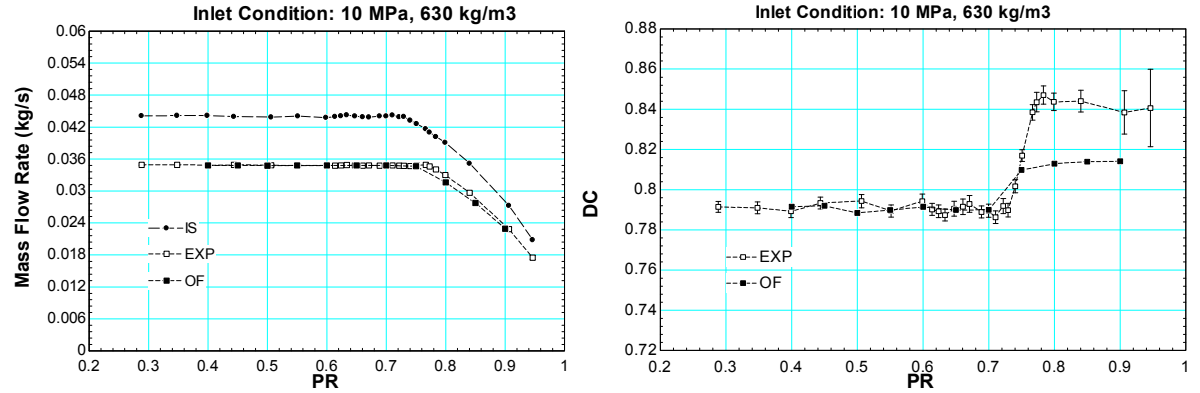

Figure 89 Circular orifice data for inlet condition of 10 MPa, 630 kg/m^3

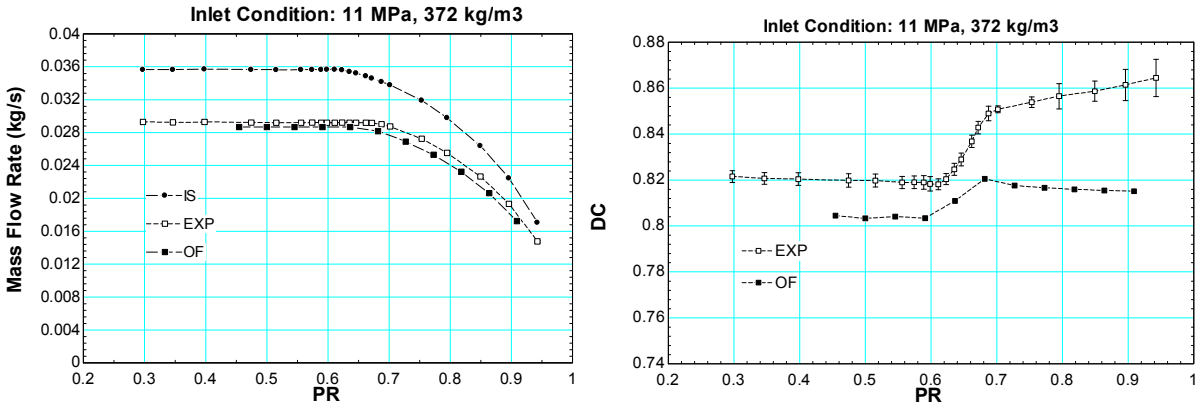

Figure 90 Circular orifice data for inlet condition of 11 MPa, 372 kg/m^3

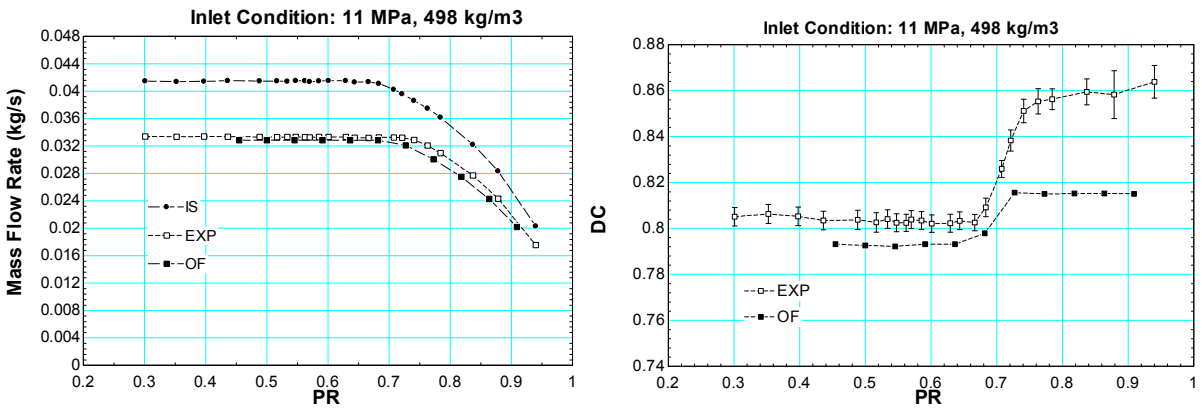

Figure 91 Circular orifice data for inlet condition of 11 MPa, 498 kg/m^3

B.2 Simulation data for annular orifice

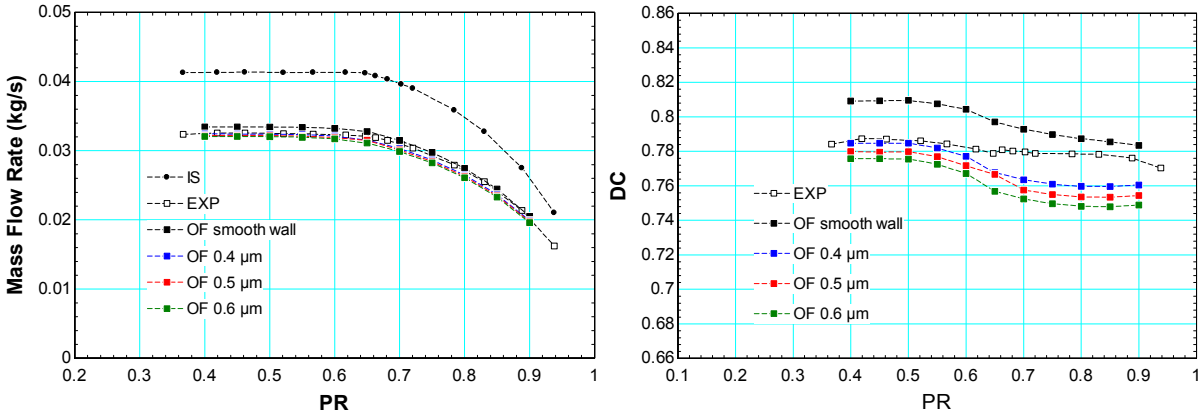

Figure 92 Medium annular orifice data for inlet condition of 10 MPa, 325 kg/m^3

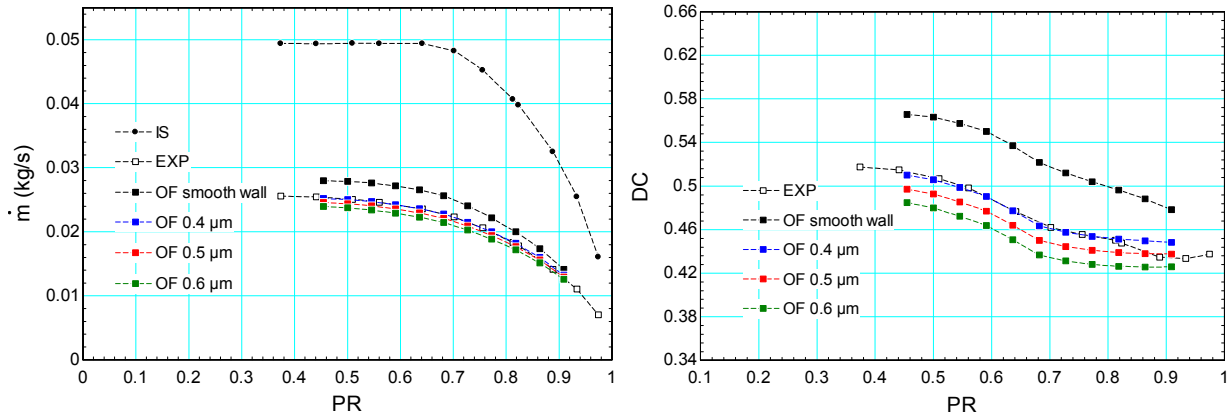

Figure 93 Long annular orifice data for inlet condition of 11 MPa, 498 kg/m^3

Appendix C: More data for labyrinth seals

In this appendix, the data from the three-tooth labyrinth seal mentioned in Chapter 5 are presented. The geometry is shown in Figure 94, along with its dimensions in Table XV. In Figure 95, the cavity height is fixed to be 0.88 mm, while the cavity length is sampled evenly between 1.27 mm to 3 m. All data in Figure 95 have the same inlet condition of (10 MPa, 372 kg/m^3), and the same outlet pressure of 5 MPa. The observation from Figure 95 is identical with Figure 46, which indicates that for different labyrinth seals and test conditions, increasing the cavity length results in a reduced leakage rate.

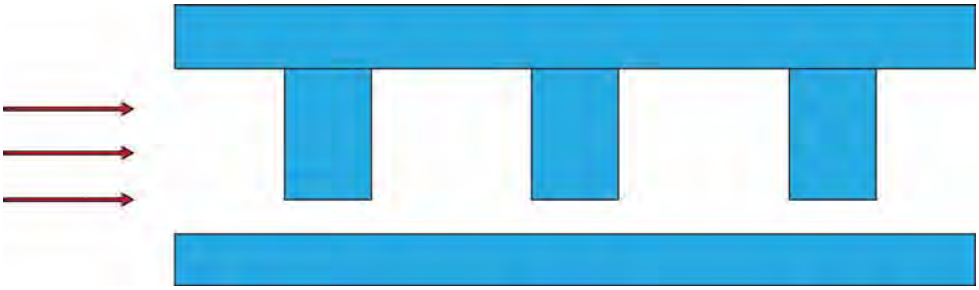

Figure 94 Schematic diagram of a three-tooth labyrinth seal.

Table XV Geometry parameter for three-tooth labyrinth seal in parametric study

Description	Notation	Number
Shaft Diameter	D	3mm
Seal diameter	D_o	3.18mm
Clearance	c	0.09 mm
Cavity height	H	0.88 mm
Cavity length	L_{cavity}	1.27 mm
Seal length	L_{seal}	1.27 mm
Total length	L_{total}	6.35 mm

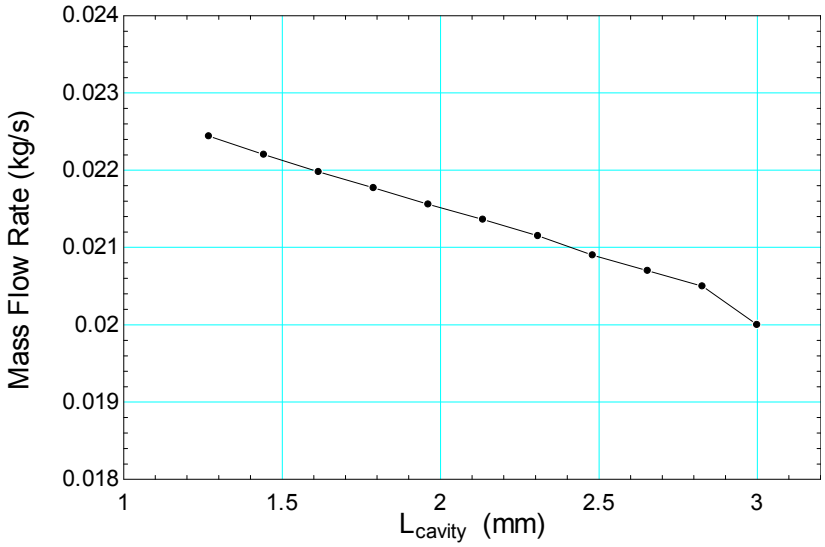

Figure 95 Mass flow rate changes with cavity length at cavity height of 0.88 mm.

The same three-tooth labyrinth seal was also used to inspect the cavity height's effect on the leakage rate. In Figure 96, the cavity length is fixed to be 1.27 mm, while the cavity height is sampled evenly between 0.15 mm and 0.80 mm. All data in Figure 96 have the same inlet condition of (10 MPa, 372 kg/m^3), and the same outlet pressure of 5 MPa. Figure 96 gives the same conclusion that there is an optimum point for the cavity height that results in a minimum leakage rate.

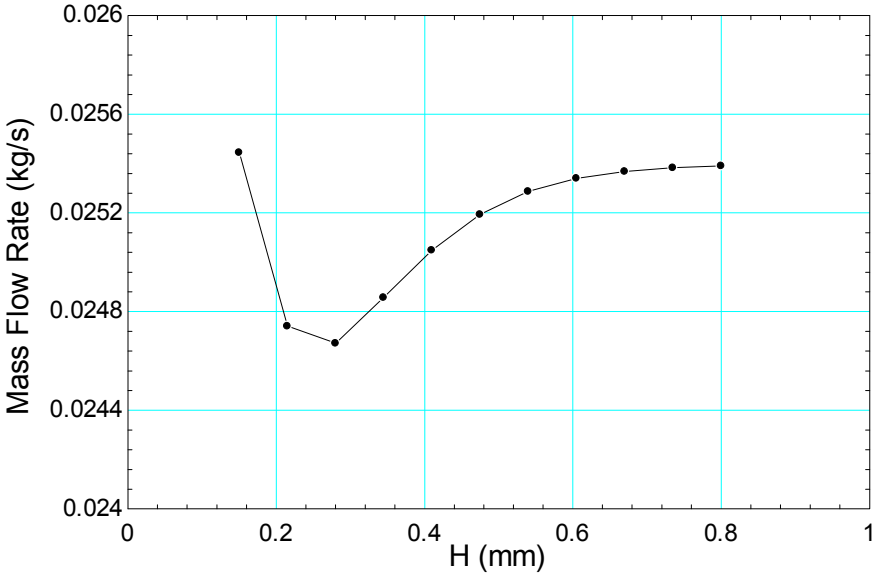

Figure 96 Mass flow rate changes with cavity height at cavity length of 1.27 mm.

Appendix D: Geometric detail of stepped shaft labyrinth seal

In this appendix, the geometry detail of the tested stepped labyrinth seal is presented. The InfiniteFocus metrology system made by Alicona [71] was used to determine its precise geometry. Figure 97 presents the measurement for the teeth arrangement from the top view. Figure 60 describes a step on the shaft, with Figure 98 showing its profile.

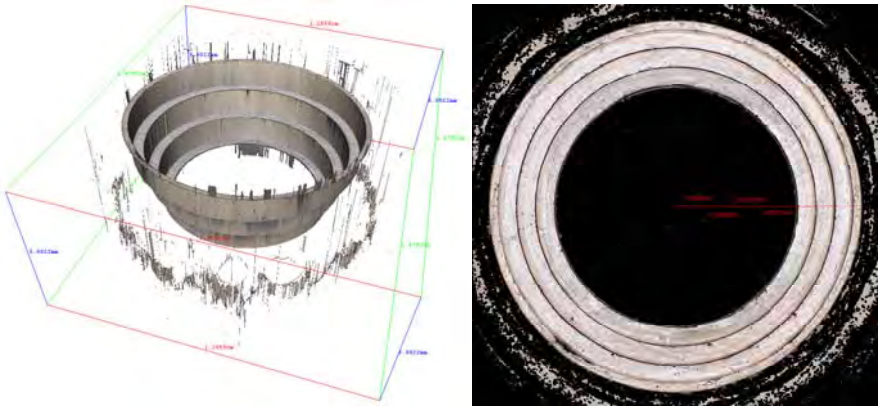

Figure 97 Stepped labyrinth seal teeth

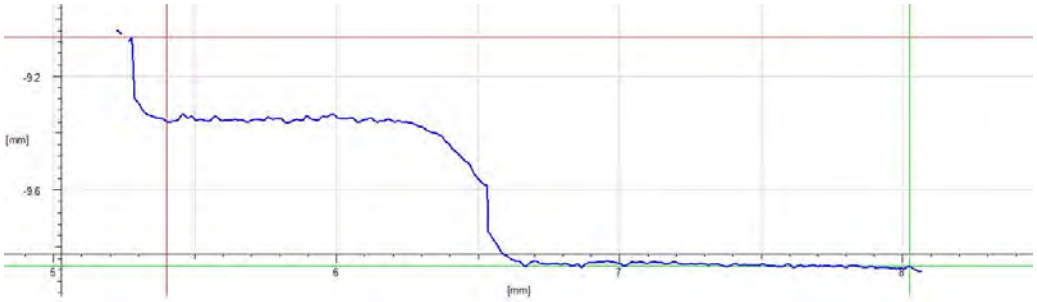

Figure 98 Profile of step on shaft

Appendix E: Optical measurement of tested valve

The optical measurement of the tested valve is presented in this appendix. The same facility used in previous appendix was used to measure the geometry of the tested valve in Figure 63. Figure 99 presents the geometric profile of the seat orifice. In Figure 99, the entrance of the seat orifice is chamfered, and the chamfered geometry is described in the simulation. Figure 100 illustrates the geometry is of the valve plug.

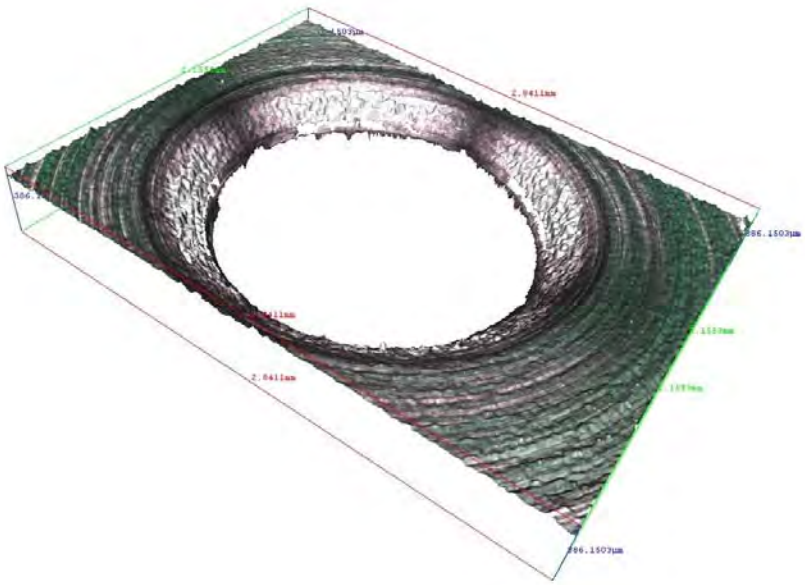

Figure 99 Entrance of seat orifice

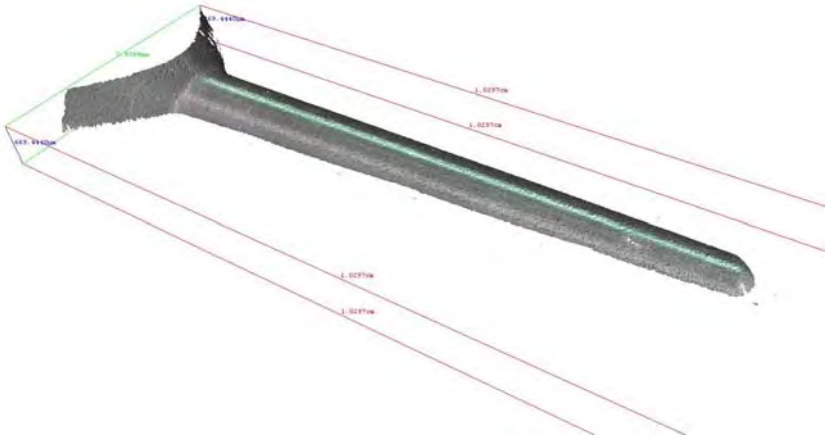

Figure 100 Geometry of valve plug

Appendix F: Source code

The source code of the modified solver and property module can be found in the link below:

https://github.com/yhaomin2007/OpenFOAM-2.1.x-withFIT.git